

Spectral Phase Manipulation of Optical Pump Pulses for mJ-Level Narrowband Terahertz Generation in PPLN

by

Spencer Windhorst Jolly, B.S.E., M.A.

DISSERTATION

Submitted to the Faculty of
Mathematics, Informatics, and Natural Sciences
Department of Physics
for the degree of

DOCTOR RERUM NATURALIUM

UNIVERSITÄT HAMBURG

November 2017

Evaluators of the dissertation:

Dr. Andreas Maier
Prof. Dr. Franz Kärtner

Date of oral defense:

10.01.2018

Chair of the disputation committee:

Prof. Dr. Robin Santra

Chair of the physics promotion committee:

Prof. Dr. Wolfgang Hansen

Head of the Department of Physics:

Prof. Dr. Michael Potthoff

Dean of the MIN Faculty:

Prof. Dr. Heinrich Graener

For Irena

Clarification of Work

Hiermit erkläre ich an Eides statt, dass ich die vorliegende Dissertationsschrift selbst verfasst und keine anderen als die angegebenen Quellen und Hilfsmittel benutzt habe.

I hereby declare, on oath, that I have written the present dissertation by my own and have not used other than the acknowledged resources and aids.

Hamburg, den

city and date

signature, Spencer W. Jolly

Acknowledgments

The number of people worthy of acknowledgment for the work presented in this thesis is very large, large enough that it may be someone is missing. I have had the pleasure of coming to the DESY campus without even knowing how great of an environment I was arriving to, and all of the people mentioned here played a part in that experience over these years. The first and most significant person to acknowledge is my supervisor Andi Maier. I started in the group certainly as an unexperienced student, but organically and with the intense support of Andi, I grew to be the scientist I am now. I will be thanking him for the rest of my career for the experiences I have had in his group, both scientifically and otherwise, and for providing an example that I fear will not be matched. I have to acknowledge Vincent Leroux and Matthias Schnepf. Vincent, Matthias, and I worked closely together for months on improving and installing diagnostics on the laser, and because of their company and truly daily input on all number of topics, the sometimes painstaking work was made enjoyable. I must acknowledge Franz Kärtner and Nicholas Matlis, with whom it was a singular pleasure to develop the chirp-and-delay experiment together, and of course Frederike Ahr, whom I was primarily with in the lab. Timo Eichner should be thanked for helping on weekends and holidays, and in general for punching above his weight as a HiWi and master's student.

The rest of the LUX team, current and former — Andi Walker, Manuel Kirchen, Paul Winkler, Philipp Messner, Niels Delbos, Chris Werle, Sören Jalas, Irene Dornmaier — can all be thanked for any number of inputs and conversations, but in general have to be acknowledged as the coolest troupe around. I was seconded to Hamburg from the ELI-Beamlines experimental program, so I thank Dariusz Kocoń, Lukáš Příbyl, and Georg Korn for support. Besides my direct colleagues already mentioned, there are many others: DESY experts such as Chris Staats, Vladimir Rybnikov, Falko Peters, and Jörg Reichow; Stephan Fleig and Frank Jonas in the UHH workshop; Heike Kaminski and Fenna Reinholdt in our Sekretariat; and the list goes on.

Outside of my work at DESY I met many friends on the Hardfisch ultimate frisbee team, who made my time in Germany even more fun than I could predict. I am thankful for the

support and understanding of my parents Robert and Lorraine, and sisters Olivia and Drew, who trust that I am across the ocean doing what I love and support me unconditionally. I would like to think that my grandmother Dr. Dorothy Windhorst, who passed away this year, would be equally proud to see her grandson continue to pursue research. And lastly I thank my girlfriend Irena, who brought me to Europe, who supported me every step of the way, and who stayed on my shoulder through the good and the bad.

It is only after sharing experiences with all of these people that I write this thesis, and I am truly grateful for the pieces of everyone I have met in Hamburg that I will carry with me.

Spectral Phase Manipulation of Optical Pump Pulses for mJ-Level Narrowband Terahertz Generation in PPLN

Abstract

The generation of mJ-level terahertz (THz) radiation is reported via quasi-phase-matching in periodically poled lithium niobate (PPLN) using chirped optical pump pulse trains from the ANGUS laser system. The integration of the 200 TW ANGUS laser system into the DESY control system architecture is outlined, which increased the availability of the system for use in experiments. The verification and characterization of the chirp-and-delay method for terahertz generation in PPLN is reported using crystals of four different poling periods, resulting as well in pulses of up to $40 \mu\text{J}$ at 544 GHz. The effect of the third-order phase present in the optical pump pulses on the process is reported in detail with a discussion especially of the effect on the efficiency of the process. The derivation of these effects is in fact general, and applies to difference frequency generation via chirp-and-delay in a broad sense, within the limitations of the analytic formulation. Compensation for this higher-order effect is studied, and a method of independently manipulating the spectral phase of the overlapped pulses is theoretically developed and experimentally implemented. This implementation results in an increase of eight times in efficiency in large aperture PPLN, producing a maximum pulse energy of $458 \mu\text{J}$ at 361 GHz with $<1\%$ bandwidth from a single crystal, and a combined average THz output of $604 \mu\text{J}$ produced in two crystals simultaneously. This has broad implications for manipulation and acceleration of particles and material studies with high-energy and narrowband pulses at sub-THz frequencies.

Manipulation der Spektralphase von optischen Pumpimpulsen für mJ-Level Schmalband Terahertz Erzeugung in PPLN

Zusammenfassung

Die Erzeugung von mJ-Level Terahertz (THz) -Strahlung ist berichtet durch Quasiphasenanpassung in periodisch gepoltem Lithiumniobat (PPLN, aus dem Englischen) unter Verwendung von gechirpten optischen Pumpimpulsen aus dem Lasersystem ANGUS. Die Integration des 200 TW ANGUS Lasersystems in die DESY Systemarchitektur, die die Verfügbarkeit des Systems für Experimente erhöht, wird skizziert. Die Verifikation und Charakterisierung der Chirp-and-Delay Methode für die Terahertz-Erzeugung in PPLN wird mit Kristallen mit vier verschiedenen Polungsperioden berichtet, wobei Pulsenergien bis zu $40 \mu\text{J}$ bei 544 GHz erreicht wurden. Die Phase dritter Ordnung, die in den optischen Pumpimpulsen des Prozesses vorhanden ist, wird im Detail mit einer wichtigen detaillierten Diskussion der Auswirkung auf die Effizienz des Prozesses beschrieben. Die Herleitung dieser Effekte ist allgemein gültig für die Erzeugung von Differenzfrequenzen über Chirp-and-Delay innerhalb der Grenzen der analytischen Formulierung. Die Kompensation dieses Effekts höherer Ordnung wird untersucht und eine Methode zur unabhängigen Manipulation der Spektralphase der überlappten Pulse wird theoretisch hergeleitet und experimentell implementiert. Diese Implementierung führt zu einer achtfachen Zunahme des Wirkungsgrads bei PPLN mit großer Apertur, was bei 361 GHz eine maximale Pulsenergie von $458 \mu\text{J}$ mit einer Bandbreite $<1\%$ ergibt. Dies hat breite Auswirkungen auf die Manipulation und Beschleunigung von Teilchen und Materialuntersuchungen mit Hochenergie- und Schmalbandimpulsen bei Sub-THz-Frequenzen.

Table of Contents

Abstract	xi
List of Figures	xv
Chapter 1. Introduction	1
Chapter 2. Background	5
2.1 High power laser pulse generation and focusing	5
2.1.1 Grating-based pulse stretching and compression	5
2.1.2 Focusing of beams	10
2.2 Basic nonlinear optics	13
2.2.1 The nonlinear susceptibility	14
2.2.2 Second-order processes	14
2.2.3 Third-order processes	17
2.3 Terahertz generation with broadband drivers	18
2.3.1 Single-cycle terahertz generation	19
2.3.2 Multi-cycle terahertz generation	22
Chapter 3. ANGUS laser — control system integration, operation, and pump-probe beam	27
3.1 ANGUS laser system overview	27
3.2 ANGUS supervision and control	30
3.3 Cooling circuit case study	32
3.4 Design for compressed pump-probe beam for the LUX experiment	35
3.4.1 Extraction and compression	36
3.4.2 Temporal jitter measurement	37
3.4.3 Optical-to-optical jitter stabilization	40
Chapter 4. Narrowband terahertz generation in PPLN with ANGUS	45
4.1 Concept of chirp-and-delay	47
4.2 Experimental overview	48
4.2.1 Detector calibration	49
4.3 Experimental results	51

4.3.1	THz output energy and conversion efficiency	53
4.3.2	THz output during cooling	57
4.3.3	Evidence of cascading in IR spectrum	58
Chapter 5.	The effect of third order dispersion on narrowband terahertz generation via trains of chirped pulses	61
5.1	Properties of phase matching with chirped-and-delayed pulses	62
5.2	Temporal phase description of IR pump pulses	67
5.3	Effect of the TOD and pulse-train on input IR field	70
5.4	Signature of TOD in experimental data	74
5.4.1	Output pump spectrum	75
5.4.2	Delay behavior	78
5.5	Effect of TOD on efficiency of THz generation via quasi-phase-matching	80
5.6	Discussion of the effect on chirp of THz pulses	83
5.7	Discussion of the effect of higher order terms	86
5.8	Outlook	87
Chapter 6.	Asymmetric compensation of higher order phase effects for high-energy terahertz generation in PPLN	89
6.1	Study for compensation of third-order phase	89
6.1.1	De-tuned grating compressor	91
6.1.2	Asymmetric compensation of phase	93
6.2	Experimental overview	97
6.2.1	SF11 prisms	98
6.2.2	High-TOD chirped mirrors	99
6.2.3	Glass wafer for THz outcoupling	100
6.2.4	Purging of detection setup for calibration of absorption	104
6.3	Experimental results	106
6.3.1	Optimization of THz energy with SF11 and TOD mirrors	108
6.3.2	High energy THz pulses from a single crystal	114
6.3.3	Generation of high-energy THz pulses in two crystals simultaneously	117
6.4	Outlook	121
Chapter 7.	Conclusion	123
Bibliography		125

List of Figures

2.1	An example of the combined effects of GDD and TOD on an <i>almost</i> ideally compressed pulse.	9
2.2	Overview of various mechanisms for generating single-cycle THz.	20
2.3	Overview of various mechanisms for generating multi-cycle THz.	23
3.1	The ANGUS laser system in concept showing the five amplifier stages and six total pump lasers.	28
3.2	The approximate ANGUS laser system performance across the different stages in pulse energy and FWHM bandwidth.	29
3.3	An example of a JDDD supervision panel for the Regen amplifier stage.	30
3.4	Amp2 crystal temperature with different extracted energies showing different equilibrium temperatures.	33
3.5	Amp1 crystal temperature on two consecutive days showing stabilization after an A/C repair.	34
3.6	The Amp1 crystal temperature is shown before and after cooling system cleaning on consecutive days showing a decrease in temperature.	35
3.7	Overview of the pump-probe setup in relation to the LUX experiment.	36
3.8	Diagram of the pump-probe extraction and recompression setup.	37
3.9	Simple and exaggerated sketch of the single-shot correlation principle.	38
3.10	Our specific cross-correlation schematic for temporal jitter measurements.	39
3.11	An example schematic for a BOC where the two beams to be jitter stabilized are colinear and have different frequencies.	41
3.12	Example of an ideal BOC signal, given pulses of the same duration and intensity.	42
3.13	An example schematic for a BOC where the two beams to be jitter stabilized are not colinear and have the same frequency.	43
4.1	Conceptual temporal arrangement of collinear chirped-and-delayed pulses with a Wigner-plot.	47
4.2	Chirp-and-delay setup using a combination of partial reflector (PR) and high reflector (HR) to generate a chirped pulse pair plus lower energy trailing pulses.	49
4.3	An example of the measured fall time of the pyro-electric detector and simulations predicting the calibration at low rep-rate.	50
4.4	Delay scan results for chirp-and-delay in PPLN with different poling periods.	52
4.5	Scaled THz output for three different frequencies at room temperature.	53
4.6	THz efficiency for three different length crystals all at room temperature with 212 μm poling period.	54

4.7	Conversion efficiency of 212 μm poling period PPLNs at room- and cryogenic temperature as a function of pump fluence.	55
4.8	THz efficiency for two different length crystals at cryo temperature with 212 μm poling period.	56
4.9	Delay scans and maximum output during cooling of a 10 mm long 212 μm poling period PPLN.	58
4.10	Delay scans and maximum output during cooling of a 20 mm long 212 μm poling period PPLN.	59
4.11	Pump spectra before and after interaction with the 212 μm PPLN showing evidence of cascading.	60
5.1	Chirp and delay concept including now the general effect of higher order phase. .	62
5.2	The THz refractive index and absorption coefficient of PPLN at 80 K, and the relative efficiency based only on these material properties.	64
5.3	The THz properties of GaP, and the relative efficiency based only on these material properties.	66
5.4	Comparison of the total pulse train envelope and frequency content at one time delay.	71
5.5	Comparison of the total difference frequency content with permutations of no TOD and with TOD, 2 pulses and a pulse train, at the four delays.	73
5.6	Chirp-and-delay experimental setup, reproduced from the previous chapter. . . .	75
5.7	Comparison of input and output IR spectrum for three different experimental scenarios.	76
5.8	Experimental output IR spectrum during a delay scan of a train of IR pulses generating THz in four different poling period crystals.	78
5.9	Comparison of calculated delay scan behavior with and without TOD and pulse-train.	79
5.10	Frequency content at 540 GHz and QPM bandwidth shown together.	81
5.11	The effect of TOD on the THz generation efficiency for different frequencies and lengths with the ANGUS pump parameters in a PPLN crystal.	82
5.12	THz pulses produced in 0.5 mm GaP with and without TOD on the pump pulses. .	85
6.1	Plot showing example parameters for a compressor such that the TOD would be zero and the remaining GDD at each set grating configuration.	93
6.2	Chirp and delay Wigner plot showing the case with TOD and exact pulse copies, and when only modifying one pulse.	94
6.3	As the compensation is increased to the ideal amount the difference frequency bends so that a higher proportion is within the QPM bandwidth.	96
6.4	A diagram of the experimental setup in this chapter.	97
6.5	A diagram of the geometry and optical path through a pair of SF11 prisms. . . .	98
6.6	Measurements of the TOD on the chirped mirrors from the supplier and from white-light interferometry.	100

6.7	The expected Fresnel transmission at the PPLN exit surface for varying frequencies.	101
6.8	Transmission at the LN rear surface for 360 GHz radiation for varying glass plate thickness and for varying vacuum spacing thickness.	103
6.9	Transmission at the LN rear surface for 558 GHz radiation for varying glass plate thickness and for varying vacuum spacing thickness.	104
6.10	A photo of an installed wafer with and without spacer.	105
6.11	Summary of humidity and purging measurements at 558 GHz.	106
6.12	THz generated at positive and negative delays for both crystals, and THz output with angle offset between the two beams.	107
6.13	Frequency measurements for the 330 μm and 212 μm poling period crystals showing 361 GHz and 558 GHz central frequencies respectively.	108
6.14	Example of three delays scans producing 361 GHz THz under the same experimental conditions with one beam propagating through various amounts of SF11.	109
6.15	Example of three delays scans producing 558 GHz THz under the same experimental conditions with one beam propagating through various amounts of SF11.	110
6.16	The summary of the full compensation with SF11 and TOD mirrors for both crystals.	111
6.17	Two full-pulse interferometer scans of the 361 GHz output when there is no compensation and with 49 mm SF11.	112
6.18	Delays scans when generating 361 GHz radiation with 49 mm SF11 in one arm and a varying amount of TOD mirrors in the other arm.	113
6.19	Delays scans when generating 558 GHz radiation with 69 mm SF11 in one arm and a varying amount of TOD mirrors in the other arm.	114
6.20	High energy output at 361 GHz showing total efficiencies up to 0.13% when pumped at 293 mJ/cm ² producing up to 400 μJ THz energy.	115
6.21	Output spectra at various fluence levels with full compensation for the 361 GHz output, and the intrinsic efficiency compared with the measured efficiency.	116
6.22	Output spectra at various fluence levels with full compensation for the 558 GHz output, and the intrinsic efficiency compared with the measured efficiency.	117
6.23	A diagram of the experimental setup for asymmetric compensation with two crystals.	118
6.24	Delay scans showing the peak in THz output at the exact same delay for both crystals.	119
6.25	THz output with increasing pump fluence for both crystals simultaneously.	120

Chapter 1

Introduction

The development of particle accelerators for many decades brought about discovery-after-discovery in the field of particle physics when used in tandem as particle colliders, colliding energetic packages of particles and analyzing the outcome of those collisions. However, as more and more discoveries were made with particle accelerators at the cutting edge in maximum energy, the ability of the current technology to continue making discoveries that are not limited by the current maximum collision energy decreased. Only advancements in investment and technology brought about even higher energy particle accelerators that could allow for more discoveries. However, what is unavoidable, even including fundamental technology improvement, is that the higher energy accelerators take up more space and therefore cost more and more. At present there are only a small number of such colliders that work at the cutting edge, and making a new one is only possible with decades of design and international collaboration. Although this is being undertaken in the FCC [1] and LLC [2] project design collaborations, complementary advanced acceleration development is absolutely crucial.

In parallel with this technology advancement for maximum energy, some of the infrastructure that was used for past particle physics discoveries was adapted to become light sources based on, for example, synchrotron radiation (the PETRA light source at DESY, Hamburg, Germany) [3] or free-electron laser (FEL) radiation (LCLS at SLAC, Menlo Park, USA) [4]. The migration of these accelerator machines to light sources having unique properties (X-ray wavelength, ultra-short duration) has also brought about many discoveries, but now in the field of photon science. These include discoveries using femtosecond diffractive imaging [5] and the unique response of atoms to hard X-rays [6]. Still, these sources come with a billion Euro price tag, and therefore are still scarce. Even longer wavelength, high average power THz and far-infrared FELs are within large price tag facilities based on large-scale rf acceleration [7, 8].

This application to photon science additionally — some would say even more-so — motivates the development of compact particle accelerators.

There are many options for compact particle accelerators, aiming to make the footprint of the accelerating infrastructure smaller (and potentially the light-source as well depending on the mechanism for light generation), so that the scarcity of such unique light sources decreases. Two methods that are most related to this thesis are laser-plasma based acceleration (laser wakefield acceleration, LWFA) [9, 10, 11, 12] and terahertz- (THz) based acceleration [13, 14, 15, 16]. This thesis will outline principally the operation specifics of the ANGUS laser system, a 200 TW laser system that is the crucial driving infrastructure for the LUX laser-plasma acceleration experiment at DESY, and generation of sub-mJ-level narrowband THz pulses, the crucial driving mechanism for THz-based linear acceleration in dielectric waveguides, relevant to the AXIS project at DESY. In addition to being relevant for acceleration, narrowband THz is also useful for deflection of particles in waveguides [17, 18], which may necessitate very high THz pulse energies to act as a proper diagnostic of temporal properties (transverse deflecting structure, TDS) [19, 20] of either high-energy or very short duration electron beams [21] such as those produced via either laser-plasma or THz acceleration.

This thesis is structured as follows. There will first be a background chapter (Chapter 2), detailing the basic physics behind high-power lasers (Section 2.1), nonlinear optics (Section 2.2), and THz generation with broadband drivers (Section 2.3). This background informs the important mechanisms and the state-of-the-art in those fields, including for example what is important in the driving laser parameters. The next chapter (Chapter 3) is a detail of the 200 TW ANGUS laser system from a general point of view, with a discussion of the control systems, a case-study showing the power of those same control systems, and also a design for a pump-probe beam to be used in parallel with the LUX experiment.

The following three chapters focus only on narrowband THz generation with the ANGUS system. This is first the initial proof-of-concept results (Chapter 4) of the quasi-phase-matched chirp-and-delay method in periodically poled lithium niobate (PPLN) already showing pulses up to 40 μ J. Then the effect of higher-order laser parameters is outlined (Chapter 5) showing a derivation of these effects, a confirmation with nuanced experimental results, and comments on the implications on the efficiency of THz generation among other properties. Lastly, methods

for compensation of these higher order effects are detailed and experimentally implemented (Chapter 6), showing an increase in the efficiency by a factor of 8. THz pulses up to a peak energy of $458 \mu\text{J}$ at 361 GHz in large aperture PPLN crystals are achieved, and a combined average THz output of $604 \mu\text{J}$ is produced in two crystals simultaneously.

The results of this work have major impact. The achievement of such a smoothly operating high-power laser system enables a new level of professionalism and reliability, which in parallel with the quality of the built LUX experiment infrastructure [22] is a game-changer in laser-plasma acceleration. The generation of sub-mJ-level THz pulses pushes the limits of the field, which includes the generally derived compensation method, and enables future THz-based particle acceleration and strongly driven resonant material studies that were not before possible at these sub-THz frequencies.

Chapter 2

Background

This chapter will provide the general background for specifics of high-power laser pulses, nonlinear optics, and a brief literature review of past work on broadband and narrowband Terahertz generation, motivating the work presented in the majority of this thesis.

2.1 High power laser pulse generation and focusing

The generation of high-power laser pulses depends primarily on two well-known phenomena: First, the creation of ultrashort seed pulses from modern oscillator cavities and second the chirped-pulse amplification (CPA) [23] method of amplifying the broadband pulses to a high energy.

The generation of femtosecond pulses with more than 100 nm bandwidth has now become routinely accessible in modern commercially available Ti:Sapphire cavity oscillators that operate in a Kerr lens mode-locking scheme, and have in-cavity spectral phase compensation. These broadband pulses are stretched and then amplified in this stretched state, avoiding laser damage of mirrors and amplifier crystals and minimizing nonlinear propagation effects, and finally after amplification compressed to the minimum duration allowed by the gain-narrowed spectrum. This is exactly the CPA method. The following section outlines some important concepts within that framework for generating high-power pulses, and also focusing them to achieve high intensity.

2.1.1 Grating-based pulse stretching and compression

Pulse stretching (compression) in time requires dispersion such that the spectral envelope is not changed, but due to a change in the spectral phase the temporal envelope is scaled to a longer (shorter) duration. Femtosecond pulses cannot be amplified directly due

to many considerations, so a stretched pulse with the same spectral content must be amplified. This stretching, amplification, and compression is done by, for example, the grating-based methods [24] that will be outlined here. The final compression produces the shortest possible pulses at the output of the final amplifier within the constraints of the spectral effects of the amplification (the Fourier limit).

Gratings are a popular solution because the alignment is relatively simple (compared to prisms), they are all reflective, and widely available. There are limitations, such as price, supplier lead time, damage threshold, thermal strain with high average power, etc. However, with all of these considered gratings are the most commonly used method for pulse stretching/compression in near-infrared laser systems.

As a reminder, diffraction gratings act as a dispersive element by diffracting different wavelength components (λ) to angles (θ_r) of an incident pulse at a single angle of incidence (AOI, θ_i):

$$\theta_r = \sin^{-1} \left(\frac{m\lambda}{d} - \sin(\theta_i) \right) \quad (2.1)$$

In all cases outlined here the diffraction order is $m=1$, so that coefficient will be dropped everywhere, and the 'diffracted angle' always refers to this first order diffraction. Then the effective spectral phase added to a pulse through a grating stretcher (through two passes) in this configuration is:

$$\phi_2 = \frac{\lambda_0^3 L}{\pi c^2 d^2 \cos^2(\theta_r)} \quad (2.2)$$

$$\phi_3 = \frac{-3\lambda_0 \phi_2}{2\pi c} \left[1 + \frac{\lambda_0 \sin(\theta_r)}{d \cos^2(\theta_r)} \right] \quad (2.3)$$

$$\phi_4 = \frac{-\lambda_0 \phi_3}{2\pi c} + \frac{\phi_3^2}{\phi_2} + \frac{3\lambda_0^3 \phi_2}{4\pi^2 c^2 d} \left[\frac{\sin(\theta_r)}{\cos^2(\theta_r)} + \frac{\lambda_0}{d} \left(\frac{1}{\cos^2(\theta_r)} + 2 \tan^2(\theta_r) \right) \right], \quad (2.4)$$

where λ_0 is the laser central wavelength, L is the distance between the grating along the central wavelength ray, and d is the line spacing (in length units). The spectral phase terms are $\phi_2 \equiv \left. \frac{d^2 \phi}{d\omega^2} \right|_{\omega=\omega_0}$, $\phi_3 \equiv \left. \frac{d^3 \phi}{d\omega^3} \right|_{\omega=\omega_0}$, and $\phi_4 \equiv \left. \frac{d^4 \phi}{d\omega^4} \right|_{\omega=\omega_0}$. These terms are also known

as the group delay dispersion (GDD, ϕ_2), third-order dispersion (TOD, ϕ_3), and fourth-order dispersion (FOD, ϕ_4). These relations are derived in past references, for example [25, 26, 27], but often have mistakes or contradictions in the coefficients. The grating separation L is also often used rather as the distance between the gratings along the normal, in contrast to along the central wavelength as here. It should be noted that the grating stretchers use curved mirrors or lenses to have an effective negative length within the stretcher so that the GDD can be positive [28]. This allows more simple geometries, higher stretching factors, and pulses that can be recompressed in grating compressors without any imaging elements.

Because there are only two tunable parameters when the laser and gratings are fixed, the grating separation L and angle (defined by θ_i), the emphasis is commonly only on the GDD and TOD. If one wishes to keep the GDD constant in a grating stretcher, and vary only the TOD, then the following must be kept, for the given constant GDD (ϕ_2):

$$L = \frac{\pi c^2 d^2 \phi_2 \cos^2(\theta_r)}{\lambda_0^3} \quad (2.5)$$

with the TOD at each set position (L, θ_r) being:

$$\phi_3 = \frac{-3\lambda_0 \phi_2}{2\pi c} \left[1 + \frac{\lambda_0 \sin(\theta_r)}{d \cos^2(\theta_r)} \right] \quad (2.6)$$

In most CPA laser systems the stretched pulses are only used to avoid adverse intensity related effects, therefore the specific temporal quantities are often unimportant. Only the pulse duration matters. In this respect only the stretching factor is important, or in principle only the GDD.

For compressed pulses the behavior is more complex, but for a pulse that is stretched significantly ($\phi_2 \gg \tau_0^2$) the pulse duration of the pulse is linearly dependent on the amount of GDD:

$$\tau_p = \frac{4 \ln(2) \phi_2}{\tau_0} = \phi_2 \delta\omega_L, \quad (2.7)$$

Where it is often good practice to use the laser bandwidth $\delta\omega_L$, which is more readily measured.

The case for a grating compressor is exactly the converse as for a grating stretcher. However, an non-imaging (and all-reflective) layout can be used since only negative GDD is needed to compensated for the positive GDD introduced in a grating stretcher of the type described above. This is of course also advantageous when producing ultrafast pulses to avoid nonlinear processes in transmittive elements.

Then, for a two-pass, double grating pulse compressor the second order spectral phase (GDD) and third order spectral phase (TOD) are:

$$\phi_2 = \frac{-\lambda_0^3 L}{\pi c^2 d^2 \cos^2(\theta_r)} \quad (2.8)$$

$$\phi_3 = \frac{-3\lambda_0\phi_2}{2\pi c} \left[1 + \frac{\lambda_0 \sin(\theta_r)}{d \cos^2(\theta_r)} \right] \quad (2.9)$$

$$\phi_4 = \frac{-\lambda_0\phi_3}{2\pi c} + \frac{\phi_3^2}{\phi_2} + \frac{3\lambda_0^3\phi_2}{4\pi^2 c^2 d} \left[\frac{\sin(\theta_r)}{\cos^2(\theta_r)} + \frac{\lambda_0}{d} \left(\frac{1}{\cos^2(\theta_r)} + 2 \tan^2(\theta_r) \right) \right]. \quad (2.10)$$

Notice that in this scenario the GDD can only be negative (L can only be positive), which is why this all-reflective configuration can only be used for pulse compression and not also pulse stretching (at least when combined with a conventional grating stretcher).

In the pulse compressor there is the exact same relationship for ϕ_3/ϕ_2 as in the grating stretcher. The pulse compressor however must be very precisely tuned to reach the ideally compressed short pulses, since relatively small deviations can significantly reduce peak intensity and modify the pulse envelope.

The reference (McMullen,77 [29]) derives an exact representation for the electric field of a compressed pulse with arbitrary amounts of GDD and TOD. This is expanded upon in the body of this work in reference to highly chirped pulses in order to derive the temporal phase in terms of the spectral phase when there is significant TOD present, but small enough to make certain assumptions. However, when the pulse is almost perfectly compressed the temporal phase is very complicated and there is a significant effect on the envelope.

Instead of going through this systematically, many examples are shown visually in Figure 2.1 for different amounts of GDD and TOD. This is relevant for processes that require

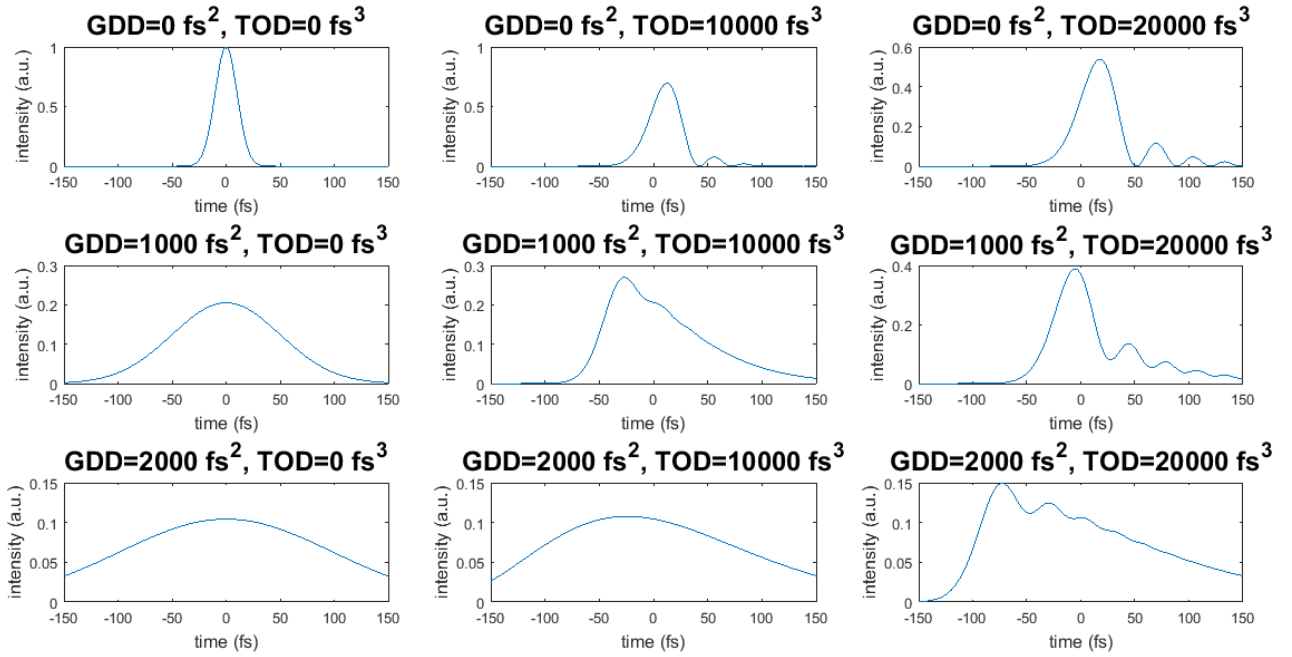


Figure 2.1: An example of the combined effects of GDD and TOD on an *almost* ideally compressed pulse. GDD only stretches the pulse whereas TOD has an effect on the symmetry and 'smoothness' of the pulse profile. The sign of the GDD does not have any effect on the pulse envelope, and the sign of the TOD essentially only reverses time. Note also that the magnitude of the TOD needs to be much larger than the GDD to have a noticeable effect.

compressed pulses, since even relatively small changes in GDD change the pulse duration significantly near the minimum (GDD=0). For example, the effect of the TOD alone can be seen in the first row of Figure 2.1, which could be the most interesting for laser-plasma acceleration [30] since the duration and therefore peak intensity remain relatively similar to the perfectly compressed case, but the symmetry and envelope of the intensity change significantly.

2.1.2 Focusing of beams

In order to create *intense* pulses one needs first high energy and short duration, as explained in the previous section. Additionally, a small spatial extent of the laser energy is needed. This is quite obvious, and is achieved simply by focusing the beam. There are few different beam types that will be discussed here: Simple Gaussian beams, cylindrical flat-top beams, and rectangular flat-top beams. These are the three most common amplified beams.

A detailed discussion of the optomechanics necessary will not be done in this section, but in almost all high-intensity laser systems an off-axis parabola is used at some shallow angle of incidence. The alignment of such an optic is quite trivial in theory, but may be complicated or tedious in practice. Additionally, the following discussion assumes that the wavefront is flat. If that is not the case, then severe aberrations may be present in the focus increasing the focal spot size and decreasing the achievable intensity. The closed-loop operation of a deformable mirror and a wavefront sensor can correct for any wavefront distortions and recover an optimal focal spot.

The most common and intuitively simple regime of laser beam propagation is Gaussian beams. These beams have a Gaussian spatial mode, which means that transverse to the direction of propagation the beam has a pulse envelope with a Gaussian form. This type of beam has relatively simple propagation rules, which will be outlined below.

The existence and rules for a Gaussian beam result from a particular solution to the paraxial wave equation. The field is constructed with a harmonic variation in the direction of propagation, with an additional unknown amplitude dependence in all three spatial directions:

$$\vec{E} = \hat{u}E(x, y, z)e^{ikz} \quad (2.11)$$

This general form for the field can be substituted in to the wave equation in vacuum for the electric field, $\nabla^2 E + k^2 E = 0$ with the vector nature excluded. This results in:

$$\frac{\partial^2 E}{\partial x^2} + \frac{\partial^2 E}{\partial y^2} + \frac{\partial^2 E}{\partial z^2} + 2ik \frac{\partial E}{\partial z} = 0 \quad (2.12)$$

The paraxial approximation is then applied, which eliminates the second derivative in z . The rationale is that the pulse envelope will vary significantly slower in the z direction than in either of the other two directions. This is essentially assuming the beam size is small compared to propagation distances, or equivalently that any angle from the axis of propagation is small (paraxial assumption).

If a Gaussian shape in the transverse direction is assumed (with a little bit of forethought included):

$$E \propto f(z) e^{-\frac{x^2+y^2}{g(z)}} \quad (2.13)$$

then a form for the $f(z)$ and $g(z)$ can be found that satisfies the paraxial wave equation.

There can be different solutions to this equation, but they are explored in detail in any standard laser textbook [31, 32]. The most important is the following cylindrically symmetric solution:

$$E = \left(\frac{2}{\pi}\right)^{1/2} \frac{\exp[ikz - i\psi(z)]}{w(z)} \exp\left[ik \frac{x^2 + y^2}{2R(z)} - \frac{x^2 + y^2}{w^2(z)}\right] \quad (2.14)$$

with all of the following properties:

$$w(z) = w_0 \sqrt{1 + \left(\frac{z}{z_R}\right)^2} \quad (2.15)$$

$$R(z) = z + \frac{z_R^2}{z} \quad (2.16)$$

$$\psi(z) = \tan^{-1}\left(\frac{z}{z_R}\right) \quad (2.17)$$

$$z_R = \frac{\pi w_0^2}{\lambda} \quad (2.18)$$

There are many things to clarify with this list of properties. w is the spot size, or more specifically the $1/e^2$ intensity radius. This is defined to be w_0 at $z = 0$ in this case and evolves according to $w(z)$. R is the radius of curvature of the phase front, is defined to be infinite at $z = 0$, and evolves according to $R(z)$. ψ is a specific value of the phase called the "Gouy phase", which changes as the beam goes through focus. And lastly z_R is a constant value referred to as the Rayleigh range. The Rayleigh range can be thought of as the distance from a focus after which the expansion of the beam waist is almost linear.

Again, many properties of a Gaussian beam can be found in Siegman's laser textbook [31]. What is important is that the Gaussian beam has an explicit relationship for the focal spot size given an initial spot size and a focal length (assuming the focal length is much larger than the Rayleigh range):

$$w_0 = \frac{f\lambda}{w_{\text{in}}\pi} \quad (2.19)$$

This means that one can always know the expected size of an optimum focus knowing only the wavelength, the initial beam waist, and the focal length (the ratio f/w_{in} is often called the f-number, $f^\#$). This is the most important feature when designing experiments and focusing optics.

The discussion for Gaussian beams is very important for the intuition of focusing laser pulses. However, in most high-intensity laser systems the pulses are actually of a flat-top transverse profile after the final stage of amplification. Because of this the focusing is subtly different.

The most ideal scenario of a flat-top beam is a truly flat top beam with infinitely steep edges. If a cylindrical beam of this intensity profile were to be focused then the focal spot profile would be exactly the Airy disk. However of course, in a real scenario the edges cannot be infinitely sharp and the intensity cannot be exactly constant within the aperture.

The proper way to analytically represent a flat-top beam then (with regards to the sharp edges) is via the super-Gaussian, written in general:

$$I(r) = \frac{1}{\sqrt{2\pi\sigma}} e^{-\frac{r^N}{2\sigma^N}} \quad (2.20)$$

With N being an integer defined as the "order" of the super-Gaussian. The edges become sharper as the order increases. The super-Gaussian does not propagate in a self-similar fashion as the Gaussian does. As a super-Gaussian is focused and approaches the Rayleigh-range, the intensity distribution extends to larger radii than for a Gaussian with the same beam diameter (corresponding to a larger effective M^2) and the peak intensity is not always on axis. Because of this it does not have the simple propagation rules and cannot be summed up quite so intuitively as the Gaussian. The focus of a super-Gaussian beam is qualitatively similar to the Airy disk, with a central strong peak and wings extending radially, but is not quantitatively exactly equivalent.

To add another complicating factor, many high energy laser systems including the L3 laser at ELI-Beamlines for example will be a square flat-top beam. This is due to the aim to extract the maximum energy from amplifier crystal. This can be similarly approximated as a two-dimensional super-Gaussian and shares the same analysis as the cylindrical flat-top beams (or radial super-Gaussian) discussed already. In this case the wings are no longer radially symmetric, and concentrated on the axes, which results in a higher maximum fluence or intensity above a certain radius.

2.2 Basic nonlinear optics

There is no doubt that this section depends very heavily on Robert Boyd's Nonlinear Optics textbook [33]. Please consult that wonderful reference for more detail and many more phenomena not mentioned in this short section.

This section presents a very brief overview of nonlinear optics. These concepts are crucial for mechanisms within many of the diagnostics for high power laser systems, many mechanisms within the cutting edge of ultrafast lasers (Terahertz generation included), and also helpful for contextualizing optical effects within a plasma.

2.2.1 The nonlinear susceptibility

The nonlinear susceptibility is the physical property that allows for nonlinear optical properties to exist in any material. In the interaction of electric fields with any dielectric medium, a polarization density is produced that represents an average dipole moment induced in the atoms within the dielectric. In linear optics this polarization density P depends linearly on the applied electric field E such that $P = \epsilon_0 \chi_1 E$ (ϵ_0 is the permittivity of free space). A well known result of this is the solution for electromagnetic waves traveling in a dielectric medium with different velocities. This is the index of refraction $n = \sqrt{1 + \chi_1} = \sqrt{\epsilon_r}$.

The nonlinear susceptibility is the natural extension of this linear effect and has wide-ranging implications. The nonlinear susceptibility means that the induced polarization is not just linear with the applied electric field $P = \epsilon_0(\chi_1 E + \chi_2 E^2 + \chi_3 E^3 + \dots)$. Since the linear susceptibility still accounts for the normal propagation in a dielectric medium, it is only the higher orders that contribute to new effects within the wave equation:

$$\nabla^2 E - \frac{n^2}{c^2} \frac{\partial^2 E}{\partial t^2} = \frac{1}{\epsilon_0 c^2} \frac{\partial^2 P_{\text{NL}}}{\partial t^2}, \quad (2.21)$$

where P_{NL} is the component of the polarization density that depends on all higher order susceptibilities. It is important to note that P and E are in reality vectors, not shown so far for simplicity, and all susceptibilities are tensors in increasing rank. It will be discussed why this is significant.

2.2.2 Second-order processes

The first nonlinear component of the susceptibility is χ_2 , which is said to be responsible for all second-order nonlinear processes. In reference to the wave equation, an incident electromagnetic wave in a medium with χ_2 produces a polarization wave dependent on the square of the electric field. In the simple plane wave view, ignoring the vector nature still, the initial electric field is proportional to $e^{i\omega t} + e^{-i\omega t}$, so the square of the electric field has components with exponential terms of $2\omega t$, etc. Therefore so does the polarization density, and the solution to the wave equation in general contains these terms. If the initial electric field is the sum of two fields with different frequencies, then the solution now must contain exponential terms

of $\omega_1 + \omega_2$ and $\omega_1 - \omega_2$ and so forth resulting from products of the field at any one of the single frequencies. This is how the second order susceptibility is responsible for what is called second-harmonic generation (SHG), sum-frequency generation (SFG), and difference-frequency generation (DFG).

It is important to discuss briefly the vectorial and tensorial nature of these relationships, in addition to the behavior with frequency. The full relationship between the polarization density and electric field is, in Einstein notation:

$$P_i(2\omega) = 2\epsilon_0\chi_2^{ijk}(2\omega; \omega, \omega)E_j(\omega)E_k(\omega). \quad (2.22)$$

This is still only in the particular case of SHG (hence only ω and 2ω), but it is important to demonstrate the fact that χ_2 in principle depends on the physical axes, and the frequencies involved, and in common cases can couple the axes producing radiation along an axis where there was no input.

A general constraint on materials useful for second-order processes is that they must be non-centrosymmetric. This means that the material (i.e. the crystal structure) has some type of spatial asymmetry. This is due to permutation rules for the χ_2 tensor and the summation form to determine the nonlinear polarization density P . Non-centrosymmetry is required to have a non-zero P due to χ_2 .

χ_2 is responsible for so many applications and processes that they cannot all be mentioned here, but one of the most relevant nonlinear processes for this work is parametric amplification, especially via difference frequency generation (DFG). The growth of DFG signal when the incident waves producing the DFG are propagating together in z can be viewed as a specific form of parametric amplification. Starting from the general nonlinear wave equation, and assuming there are waves at three frequencies ω_1 , ω_2 , and ω_3 such that $\omega_2 = \omega_3 - \omega_1$ all propagating together with the same polarization and in the same direction, then there are in principle three coupled equations for the amplitude of the different waves as they propagate in z .

Assuming that there is a strong driving wave at ω_3 with field amplitude A_3 that does not change, then there are now just two coupled equations that define the evolution of the other

two waves [33]

$$\frac{dA_1}{dz} = \frac{i\omega_1^2\chi_2}{k_1c}A_3A_2^*e^{i\Delta kz} \quad (2.23)$$

$$\frac{dA_2}{dz} = \frac{i\omega_2^2\chi_2}{k_2c}A_3A_1^*e^{i\Delta kz}. \quad (2.24)$$

In this $\Delta k = k_3 - k_1 - k_2$ represents the phase matching. Assuming that $A_2(0) = 0$, $A_1(0) \neq 0$, and $\Delta k = 0$ (perfect phase matching) is essentially the most simple scenario in optical parametric amplifiers (OPAs) where A_3 is the "pump", A_1 is the "seed", and A_2 is the "idler". This results in the the following relation [33]

$$A_1(z) = A_1(0)\cosh(\kappa z) \quad (2.25)$$

$$A_2(z) \propto A_1^*(0)\sinh(\kappa z), \quad (2.26)$$

where $\kappa \propto |A_3|^2$. So both the seed and idler grow together as they propagate with the pump in z .

A simple extension of this classic optical parametric amplification model is useful for understanding wave generation via DFG between delayed copies of pulses. Adding the constraint that $A_1 \sim A_3$ and therefore $dA_1/dz = 0$ as well, then the coupled equations are now only one equation for A_2 . Adding absorption of this wave α_2 in an ansatz leads to

$$\frac{dA_2}{dz} = \frac{i\omega_2^2\chi_2}{k_2c}A_3A_3^*e^{i\Delta kz} - \frac{\alpha_2}{2}A_2. \quad (2.27)$$

Assuming that $A_2(0) = 0$, but not restricting Δk has the solution

$$A_2(z) = A_3A_3^*\frac{2i\omega_2\chi_2}{n_2c}\frac{[e^{i\Delta kz} - e^{-\alpha_2 z/2}]}{(\alpha_2 + 2i\Delta k)}. \quad (2.28)$$

With only some small modifications this leads to the useful equations in Chapter 5 for generation of THz via quasi-phase-matching [34].

2.2.3 Third-order processes

The third-order susceptibility χ_3 is similarly the term that relates the third power of the electric field to the polarization density $P \propto \chi_3 E^3$. Without going into depth, χ_3 can be responsible in a similar fashion to wavelength conversion processes that now have three input waves, and therefore a larger number of possible permutations (called four-wave mixing, FWM). Additionally, since there are now more input terms involved in the full relationship, χ_3 is in full a tensor of one-rank above χ_2 . Contrary to χ_2 processes, χ_3 processes no longer require asymmetry and can exist in isotropic media. This includes very common media, such as air or simple glass.

An important result of χ_3 is an intensity dependent refractive index. Looking at the wave equation, if the polarization density is just proportional to $\chi_3 EI$, where $I \propto E^2$, then that term no longer contributes to any nonlinear process, but can be included within the normal refractive index, creating a nonlinear refractive index term $n = n_0 + n_2 I$ where $n_2 = 3\chi_3/4n_0$. This is only one of many interesting results of χ_3 .

Additional third-order nonlinear processes include: self-phase modulation (SPM), which causes a short pulse to compress or stretch in time due to the temporal variation in refractive index based on $n_2 I$; cross-phase modulation (XPM), where one beam influences a similar effect as SPM on a second beam; cross-polarized wave generation (XPW), where there is an anisotropic χ_3 that causes intensity based polarization rotation [35].

The phenomenon of self-focusing, caused by the spatial variation of the nonlinear refractive index is outlined here as an example of a specific χ_3 process. Self-focusing of laser light is, as one would expect, classified as a "self-action" effect. These types of effects are a result of the presence of the laser field itself modifying the surrounding material or substance, which results in some type of modification of that same incident field.

Self-focusing in a bulk material (not a plasma yet) results in general from the spatial variation of the intensity dependent refractive index of a material, or $n_2 I$

$$n = n_0 + n_2 I. \tag{2.29}$$

In a way similar to that of an actual lens, the material with the field now incident upon it causes a change in the phase fronts resulting in focusing. This can be quantified by equating the effective distance traveled by a wave at the edge of the finite incident beam, a distance w_0 from the axis with no field, and a wave on the axis where an intensity I is present.

$$(n_0 + n_2 I) f_{\text{SF}} = \frac{n_0 f_{\text{SF}}}{\cos(\theta_{\text{SF}})} \quad (2.30)$$

$$\cos(\theta_{\text{SF}}) = \frac{n_0}{n_0 + n_2 I} \quad (2.31)$$

Where f_{SF} is the focal length and θ_{SF} is the angle of convergence. If it is assumed that the angle of convergence is very small, i.e. a paraxial approximation, then a Taylor expansion can be done to further simplify the relation (note that this approximation is equivalent to assuming that the nonlinear refractive index is small compared to n_0)

$$\theta_{\text{SF}} = \sqrt{\frac{2n_2 I}{n_0}}. \quad (2.32)$$

Remembering the geometry, especially the initial width of the beam, one can solve for the focal length.

$$f_{\text{SF}} = w_0 \sqrt{\frac{2n_2 I}{n_0}}, \quad (2.33)$$

which represents the scale-length after which a collimated beam of a given initial peak intensity would reach a focus. There is exceptional literature work done on the exact effect of self-focusing on super-Gaussian beams [36] showing the development of a Townes profile and radial asymmetry breaking due to intensity noise on the initial super-Gaussian profile.

2.3 Terahertz generation with broadband drivers

This section reviews the developing field of generation of broadband (single-cycle) and narrowband (multi-cycle) THz pulses with broadband drivers, both compressed and chirped

(stretched). There are multiple nonlinear materials involved, multiple methods of phase matching, and different pump-pulse wavelengths and formats for each scenario. The following two sections attempt to summarize the literature in a compact way, motivating additionally the results in the body of this work. Simple schematics generating single-cycle and multi-cycle THz pulses are shown in Figure 2.2 and Figure 2.3 respectively.

2.3.1 Single-cycle terahertz generation

Generation of single-cycle THz pulses has rapidly progressed over the last decade, and now is used for new optical physics and for interacting with charged particles. A relevant example of an application is the development of a THz-based streak camera for X-ray pulses [37], which has been used to characterize the relative arrival time [38, 39] and temporal structure [40, 41] of FEL pulses.

One of the most widely used techniques to generate single-cycle THz pulses is via pumping with a compressed, Fourier-limited laser pulse and tilting the pulse-front to phase match within a specially cut prism of lithium niobate (LN) seen in Figure 2.2(a). The vast difference between the indices of refraction for the THz and the NIR pump requires that the pulse-front of the NIR is significantly tilted, usually $\sim 60^\circ$. This was first demonstrated in [42], pushed to the $10 \mu\text{J}$ energy level in [43], and proceeded over the years following [44, 45, 46] to reach sub-mJ energy levels [47]. What is interesting in this case is that the optimum pulse duration is ~ 600 fs, so ultrashort Ti:Sapphire lasers are often too short at the Fourier limit (therefore too broadband) to be optimized for this process. There has been study of some additional experimental parameters, for example pump wavelength [48], and very thorough theoretical studies of all relevant parameters [49, 50].

The medium for the tilted pulse-front (TPF) method is lithium niobate as mentioned, and the phase matching technique is quite unique. Lithium niobate is used mainly due to its high nonlinearity χ_2 and high damage threshold aided by MgO_2 doping. However, there are other materials that allow for single-cycle THz pulses without the complexity of the tilted pulse-front, using only thin electro-optic materials [51]. Multiple materials have been used in early results [52, 53], but the prominent example is organic salt crystals. These organic crystals have a very high nonlinearity, but the properties are very different than lithium niobate. The

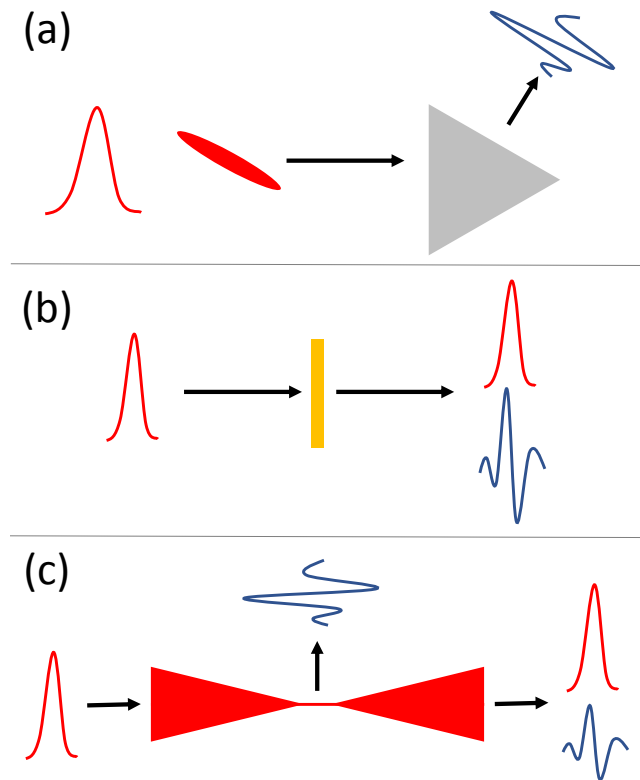


Figure 2.2: Overview of various mechanisms for generating single-cycle THz. Pumping via sub-ps NIR pulses with a tilted pulse-front **(a)** accomplishes phase matching and produces single-cycle THz in a specially cut LN prism. Pumping thin nonlinear crystals with ultrashort pulses **(b)** produces single-cycle THz without the need for complex phase matching. Air-plasmas produced from focused ultrashort pulses **(c)** can also produce single-cycle THz at many angles, but generally at a very low pulse energy.

organic crystals are much more difficult to grow, and therefore do not have the same size, length, durability, and damage threshold as lithium niobate. However, they have been very successful in generating single-cycle THz. In this case there is actually no phase matching, so the thickness of the crystals is set to one-quarter of the coherence length, and is therefore sub-mm. This case is shown schematically in Figure 2.2(b).

The first high energy results were pumped with Ti:Sapphire lasers in DAST and DSTMS [54] with progress in using partitioned crystals to increase the available aperture with only minor detrimental effects on the available peak field when focused [55]. However, these crystals are actually not completely transparent to 800 nm radiation and therefore the first results using Ti:Sapphire were not optimized. Development of a Cr:forsterite laser operating at 1.25 μm and ~ 150 fs enabled the researchers to increase the output to 0.9 mJ in DSTMS [56] along with high efficiency results also with DAST and OH1 [57]. They have continued crystal development in parallel, and used Ti:Sapphire to generate THz in BNA crystals [58], and have proposed the use of triangular selenium [59].

An additional method worth mentioning for producing single-cycle THz is via air-plasma produced by focused ultrashort laser beams, either single-color [60, 61] or two-color [62, 63]. The THz propagates at many angles from the original propagation direction seen in Figure 2.2(c). It has been reported for example that THz has been produced with NIR pump pulses below 1 μJ in ambient air, thus increasing the availability of a THz source [64], but this is a completely different parameter range where the peak energy or field of the THz is not high and the THz is not as directed as in the previously described solid-state nonlinear optical sources.

Beyond production of single-cycle THz from laser-based sources, such THz can also be produced from high-energy particle beams transitioning between regions with different electronic properties. This can be used as a diagnostic of the beam properties in high energy modern rf-based accelerators [65], which also already produces beams with a high peak field [66], but also occurs at the plasma-vacuum interface in laser-plasma accelerators [67, 68]. In recent years these sources of transition radiation have become an area of intense development for the diagnosis of the ultrashort bunches that are produced in laser-plasma acceleration, which produce transition radiation extending well beyond the THz range [69, 70].

2.3.2 Multi-cycle terahertz generation

The generation of multi-cycle or narrowband THz pulses is a parallel field of study that has lagged slightly behind the generation of single-cycle THz. This is partially due to the fact that the single-cycle pulses have a significantly higher peak field and therefore are more useful for experiments that require THz intensity (or peak field) only. As already mentioned however, such narrowband THz pulses are also useful for many applications.

One of the most experimentally simple methods for generation of these narrowband THz pulses is propagating a compressed pulse through a narrowband nonlinear medium. Within a Fourier-limited pulse the large bandwidth of optical frequencies produce difference frequency with each other (intra-pulse DFG) and this grows with the length of propagation in the crystal. The difference in this case from the very thin organic crystals, is that now the DFG is phase matched along the length of the medium. Due again to the disparate NIR and THz indices of refraction direct phase matching is not practical and the medium must be periodically poled to allow for quasi-phase-matching. The common material is periodically poled lithium niobate (PPLN). Because the compressed pulse and THz now co-propagate over many coherence lengths they have group-velocity walk-off (but are still phase matched), which causes the THz duration to be many times longer than the compressed pulse (approximately proportional to the number of poling periods).

This was shown first in [71], where the pulse energies were still sub- μJ (in the 1–2 THz frequency range). Important concepts such as the effect of absorption on the temporal envelope and the effect of poling period Λ and temperature on the central frequency were demonstrated very quickly [72, 73], summarized in Figure 2.3(a). At room temperature the high absorption of the THz in the PPLN causes the tail of the pulse to have lower amplitude since it has been produced earlier in the crystal and therefore propagated through a greater length. Once cooled to cryogenic temperatures the overall THz output increases, with the tail of the pulse now being essentially equal in amplitude to the head of the pulse, confirmed also in [74]. The variation of the index of refraction with temperature modifies the phase matching condition, such that as the crystal temperature decreases from room temperature to cryo-temperature the output THz frequency ν_{THz} for a given poling period Λ increases. Additionally, the more expected behavior of decreasing ν_{THz} with increasing Λ was confirmed. Although the most interesting,

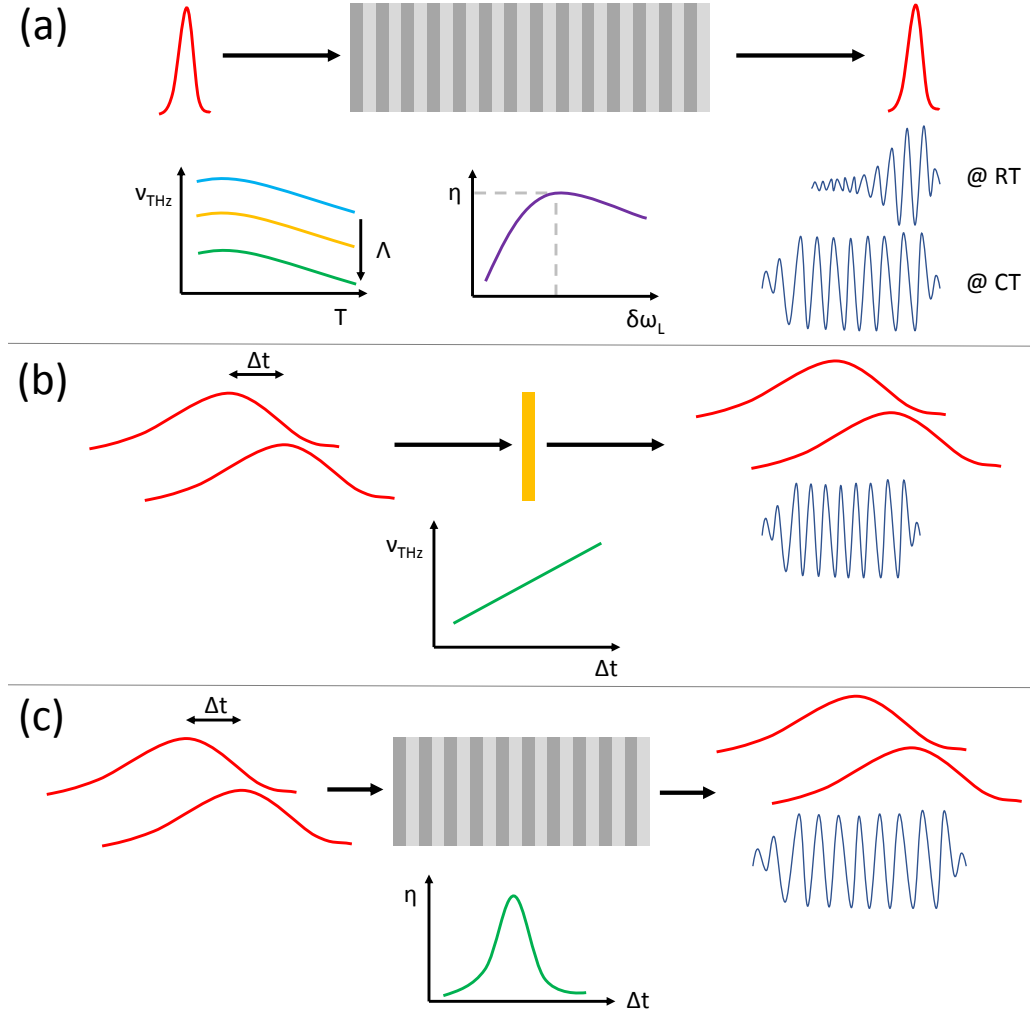


Figure 2.3: Overview of various mechanisms for generating multi-cycle THz. Pumping with compressed pulses in long PPLN crystals **(a)** produces multi-cycle pulses where the frequency ν_{THz} is in general tunable only via the temperature and poling period Λ , and due to a complex interplay of nonlinear effects there is an optimum pump bandwidth $\delta\omega_L$. Using overlapped chirped pulses in thin nonlinear crystals **(b)** produces multi-cycle THz where now the frequency is tuned via the temporal delay (and depends on the exact chirp of the pump NIR beams). Using chirp-and-delay in long PPLN crystals **(c)** is a method to generate high-energy output that requires an ideal Δt for a given poling period, and can show increased output along the length of the crystal, but is not limited by nonlinear effects or crystal damage.

high energy output is along the direction of propagation of the pump, surface emitted THz [75] and backward propagating THz [74] was also observed in these periodically poled structures.

Improvements over the years led to output of μJ pulses due to cryogenic cooling and optimization of the pulse bandwidth [76], and importantly the use of crystals producing THz in the 0.5 THz range where absorption is lower. The process is limited by damage at these short pulse durations, and nonlinear effects over the $\sim\text{cm}$ lengths of the crystals. The limitation due to nonlinear effects was confirmed by the measurement of an optimal laser bandwidth (and therefore pulse duration) $\delta\omega_L$ for a crystal of a given length. This generation was more generally described using trains of compressed pulses as well in [34]. Pumping with a train of these compressed pulses could lead to a mitigation of the damage threshold limitation and the generated THz from each pulse in the train could add coherently, with upcoming experimental demonstration of this [77].

A complementary technique is so-called chirp-and-delay, which instead of compressed pulses uses broadband chirped pulses that are then split into copies, delayed in time, and overlapped. This was shown experimentally in many different types of experimental setups: biased GaAs photo-conductive antennas in a Michelson-like setup producing radiation up to 1.5 THz [78]; in ZnTe using type-II phase matching producing radiation from 0.3–2.5 THz [79]; in bulk lithium niobate using TPF phase matching producing tunable radiation from 0.3–1.3 THz, and a peak pulse energy of $10\ \mu\text{J}$ [80]; in thin organic crystals driven by two separate chirped OPAs producing tunable radiation between 4–18 THz [81]; and recently in GaSe using two chirped OPAs producing radiation between 20–30 THz [82], which is technically MIR radiation rather than in the THz regime. In all of these cases because there was either no phase matching or direct phase matching, the temporal delay Δt determines the output frequency, shown simply in Figure 2.3(b).

One last nascent technique is the overlapping of closely spaced narrow frequency components in a nonlinear medium, for example PPLN, which very closely resembles the classic parametric amplification picture. This is very different than all of the phenomena addressed so far, which required broadband driver pulses. Cascading of this process may produce as well high energy THz [83, 84].

A significant amount of this work will be detailing this chirp-and-delay method specifically via quasi-phase-matching in PPLN, which has already been shown in principle in [85], which is reproduced in Chapter 4 with some updates. In this case THz pulses are produced in the 0.5 THz range due to the properties of PPLN, and in principle not tunable via temporal delay as in most of the examples using thin crystals, but only by the crystal poling period. Due to the phase matching bandwidth the change in Δt only optimizes the THz efficiency η for a given poling period, seen in Figure 2.3(c). Various theoretical nuances are shown in [86, 34] and also especially in Chapter 5.

Chapter 3

ANGUS laser — control system integration, operation, and pump-probe beam

All of these activities in this chapter were done with the help of extreme collaboration with V. Leroux, M. Schnepf, and A.R. Maier, but all analysis is that of the author. Responsible DESY experts are referenced when relevant.

This chapter will focus on an overview of the ANGUS laser system and its integration into the TINE [87] and DOOCS [88] control systems at DESY. Additionally there will be example of results, such as a two-month long test, along with a case-study showing operation parameters and interesting behaviors of the laser system using the power of these control systems. In addition to a description of the laser system itself, a design for a pump-probe beam will be detailed. This pump-probe infrastructure is useful for probing the plasma target at LUX, or interacting with the electron beam or X-ray beam at LUX as a pump or as a probe.

3.1 ANGUS laser system overview

The ANGUS laser system is a Titanium Sapphire based laser system producing broad bandwidth, high energy pulses with high temporal contrast and focusability. The laser is based on a THALES Lasers ALPHA 5/XS 200 TW system using chirped-pulse amplification (CPA) [23] with considerably improved diagnostics, active pointing stabilization, and control system integration. Due to these improvements the reliability and accessibility of the laser amplifiers is significantly improved from the original status. A chart showing the stages of the laser system for reference is shown in Figure 3.1.

The laser system is seeded via a Vanteon oscillator with above 100 nm bandwidth, below 15 fs pulse duration, and 83.275 Mhz repetition rate set by the cavity length (and tuned to high precision to match an external radio-frequency master clock for future experiments). This serves

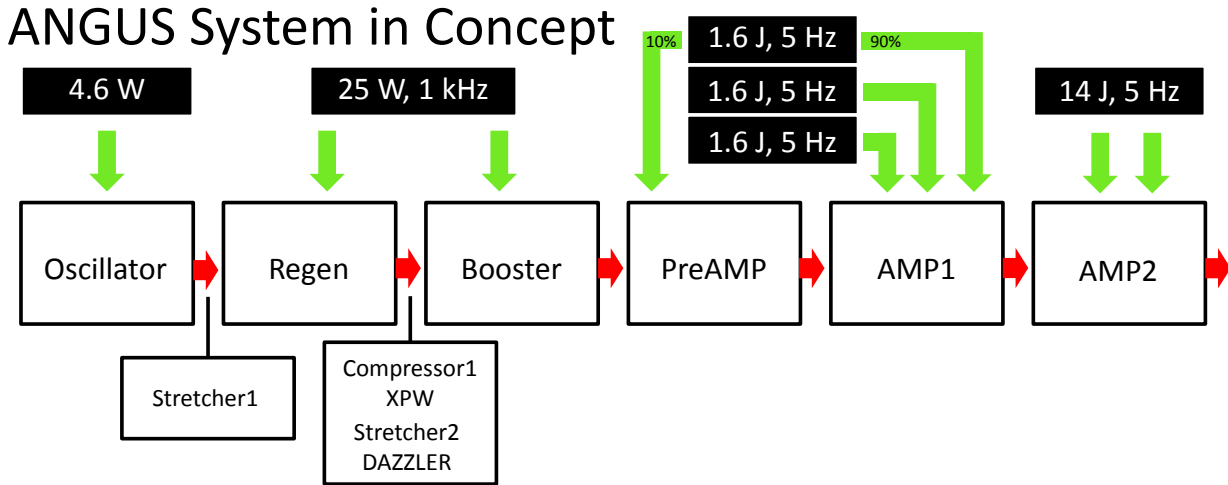


Figure 3.1: The ANGUS laser system in concept showing the five amplifier stages and six total pump lasers (green).

as both the initial laser seed and the time base for the rest of the amplification. The pulses are immediately stretched via an Öffner-stretcher and amplified in a regenerative amplifier to roughly $500 \mu\text{J}$, pumped with a frequency-doubled Nd:YLF laser at a 1 kHz rep-rate. The next stage is a so-called cross-polarized-wave generation (XPW) stage [35], which is responsible for increasing the fs-level temporal contrast. This stage involves a grating compressor, and a pair of nonlinear crystals and polarizers that transmit only the intense central pulse. This stage rejects pre- and post-pulses at the fs- and ps-level and simultaneously broadens the spectrum.

The pulses are then stretched once more with a much larger, but identical Öffner stretcher, and have the spectral phase and amplitude modified by the DAZZLER [89] in order to pre-compensate for gain narrowing in the multi-pass amplifiers and to allow for small scale optimization of the compression at the output of the final compressor. The pulses are then amplified in a two-pass Booster stage still pumped at 1 kHz via the rest of the same Nd:YLF laser up to an energy in excess of $50 \mu\text{J}$. A Pockels Cell selects a 5 Hz (or lower) pulse train from the 1 kHz output. The pulses are then amplified at this chosen rep-rate pumped by frequency-doubled Nd:YAG lasers in the three final multi-pass amplifiers of 5, 3, and 3 passes (called PreAmp, Amp1, and Amp2) to $>30 \text{ mJ}$, $>1.2 \text{ J}$, and $>6 \text{ J}$ respectively. A summary of these stages is shown in Figure 3.2 showing only the pulse energy and bandwidth. The final pulses have a 75 mm diameter and more than 40 nm FWHM spectral width. It is possible to

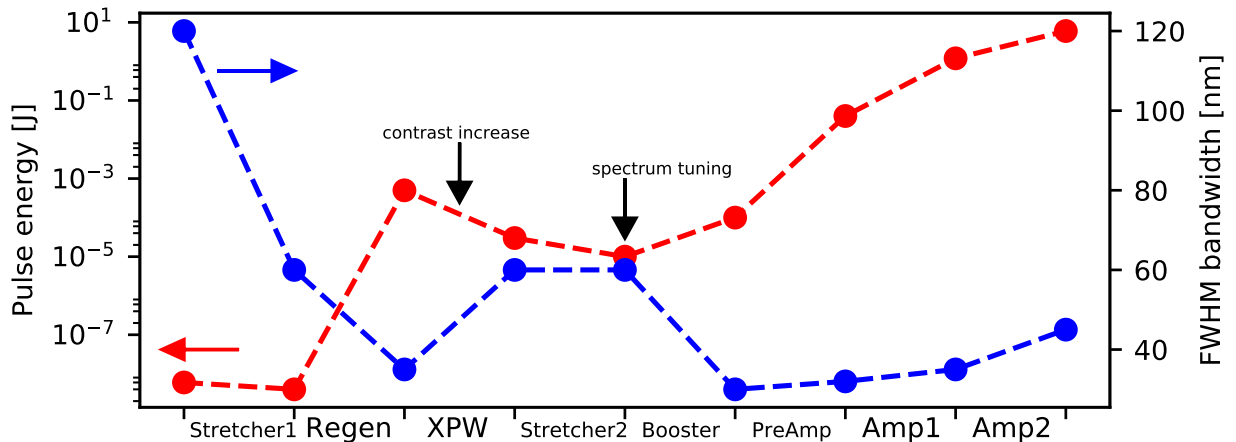


Figure 3.2: The approximate ANGUS laser system performance across the different stages in pulse energy (red) and FWHM bandwidth (blue). Although the pulse energy is clearly increased by 9 orders of magnitude throughout the system, there is an interesting interplay as the energy is decreased in the XPW (to increase fs- and ps-level contrast) and before the Booster stage where the DAZZLER tunes the spectrum.

optimize the spatial wavefront via a deformable mirror and Shack-Hartmann type wavefront sensor [90] crucial for such high energy Ti:Sapphire systems [91] in order to achieve the high focusability necessary for the laser-plasma experiments [92]. The work for improving the wavefront, especially for the laser-plasma experiments, was undertaken primarily by V. Leroux. The pulses are finally compressed in a large in-vacuum grating compressor to well below 40 fs.

After the compressor the pulses are sent to the 40 m laser transport beamline to the LUX laser-plasma acceleration experiment [22]. Additionally, there is a mirror that sends the leak-through of the compressor output to an optical table for mostly temporal diagnostics to confirm proper compression and temporal envelope. These include, not simultaneously, a WIZZLER device [93, 94, 95], a single-shot autocorrelator [96, 97, 98], and a FROG [99] for pulse duration measurements and a scanning third-order autocorrelator [100] for pulse contrast measurement. This optical setup is also used for wavefront, beam profile, and beam pointing measurements.

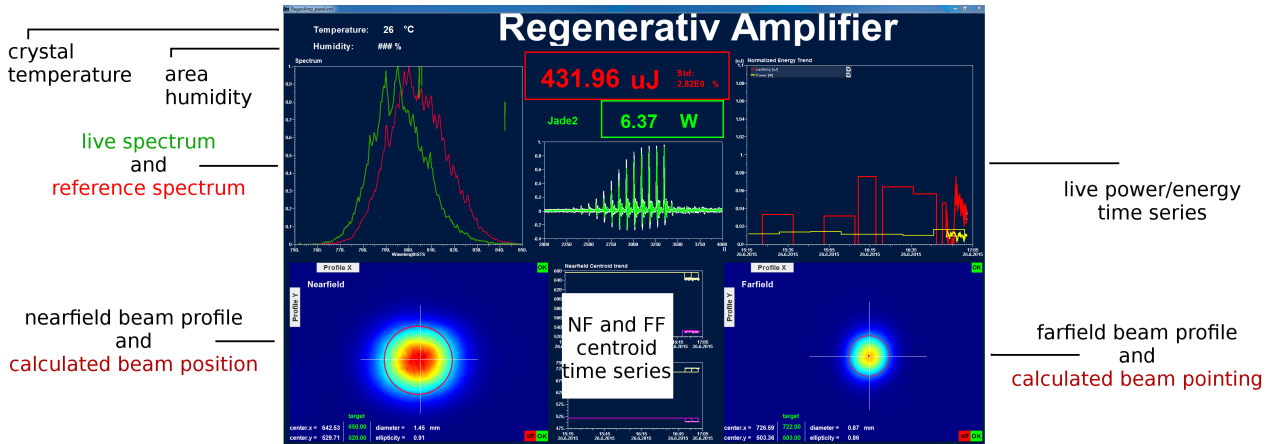


Figure 3.3: An example of a JDDD supervision panel for the Regen amplifier stage. There are a total of 8 such panels installed permanently within view in the ANGUS lab.

3.2 ANGUS supervision and control

In addition to the physics and technology that make generating the high-power ANGUS pulses possible, there is a significant amount of engineering and software investment needed to make the laser more reliable and available. That is, to reduce the probability of failure, decrease the variability of the working points, and decrease the time needed to bring the laser system up to specs.

The initial state of the laser system contained diagnostics within the laser chain that included 5 optical spectrometers, 4 CCD cameras (with an energy measurement associated to CCD counts), three quad-region diode beam pointing systems, all within a executable windows software with a LabView background. D. Trosien, V. Leroux, M. Schnepf, A.R. Maier, and the author spent significant time updating this setup.

The initial improvements involved the following: installing two more spectrometers to have every stage characterized, installing actual power and energy meters to have a true (calibrated) energy or power measurement of each stage, installing nearfield (NF) and farfield (FF) cameras to look at the beam position and pointing out of all of the stages (eliminating low quality quad-region sensors), and installing temperature sensors on all laser crystals and pump laser water supply lines to monitor thermal properties. This also involved monitoring the variables via self-made LabView software pushing to the TINE control system for the energy/power and

spectrum data (courtesy P. Duval DESY MCS), and integrating all cameras into the DOOCS camera server [101] (courtesy V. Rybnikov DESY FLA) and the beam centroid, stabilization, and picomotor communication servers (courtesy F. Peters DESY FSLA) which made our new auto-alignment possible. The auto-alignment has implications for the performance of the laser system, already shown on a lower power system in literature [102], which is beyond the scope of this work.

In addition to software to take and archive data we installed 8 monitors on the lab walls so that all data could be displayed via JDDD [103] (courtesy E. Sombrowski DESY MCS) and therefore always available. An example is shown in Figure 3.3 for the Regen amplifier. Although this is not a physics solution, these panels enable problems to be noticed very quickly, pinpointed to only within one specific subsection, and solved as fast as possible. Also, when there are no issues they allow for the laser to be brought to operating points in 30 minutes to 1 hour on a daily basis.

Since the exact topology and form was always changing, we undertook a 7 week long continuous test of the system (up to Amp1 or Amp2, without compression) during summer 2015. This test resulted in hundreds of thousands of data points from our already quite large set of on-line measurements.

We learned a significant amount from the test. For example, the TINE archive can only work with up to 1 Hz, which was known already. This is not significant for long-term trends, but if knowledge of fluctuations or high-frequency characteristics of data is desired then it's essentially not possible with the TINE archive. Additionally, operating on self-built servers meant for more operational complexity from a software point of view than was desired. Over the many months after the long term test we upgraded partially to a DOOCS optical spectrometer server (F. Peters DESY FSLA), M. Kirchen and S. J alas developed an in-house DOOCS server for the Gentec energy and power sensors installed as part of our upgrades to the system, and in general we expanded cameras and measurement devices where we were lacking. The most recent layout of the controls system for *only* the laser system includes 14 power or energy measurements, 8 optical spectrometers, and 23 cameras (through 6 ethernet switches) over 11 server computers, which in turn control 12 picomotor driven mirror mounts.

A few power measurements remain within the TINE controls system since they are implemented via digitized photodiode signals and that method is not fully implemented through DOOCS in the ANGUS lab. Additionally, two optical spectrometers are still within TINE, the XPW and Booster stages, because the spectral shape at that point in the laser system is very important and only within our TINE software do we so far have the ability to display reference spectra.

This communicates the complexity of the integration, but the amount of data involved also shows how important it is to measure and display relevant laser parameters during operation. This painstaking implementation of the DOOCS and TINE controls system for the entire laser chain and beyond empowered learning a lot about the system and solving problems at unprecedented speeds (crystal damage, back reflections, water leaks...). One novel example of learning from variables measured in the controls system, in this case the amplifier crystal temperatures and output energies, is outlined in the next section.

3.3 Cooling circuit case study

The operation of such a high-energy laser system at a rep-rate of up to 5 Hz results in significant thermal load on the amplifier crystals. Therefore as is standard practice, the Ti:Sapphire amplifier crystals are cooled via a closed-loop water-based cooling circuit. This case study will outline a few analyses that are interesting confirmations of the functionality of such a cooling circuit and demonstrate how inclusion of temperature sensors in the controls system can increase awareness of that functionality and of potential issues related to the amplifier crystal temperature. D. Trosien should be recognized for implementing these temperature sensors.

The physical phenomenon that is occurring is that the energy from the pump not converted to extracted seed energy is converted rather to heat within the crystals. Simply, the amount of heat left in the crystal is proportional to the difference between the extracted energy of the amplifier and the pump pulse energy.

Figure 3.4 shows this phenomenon in practice. When the energy extracted in the final multi-pass amplifier (Amp2) increases with a constant pump energy (done via increasing the input energy from Amp1) the cooling circuit equilibrium changes. The temperature on the

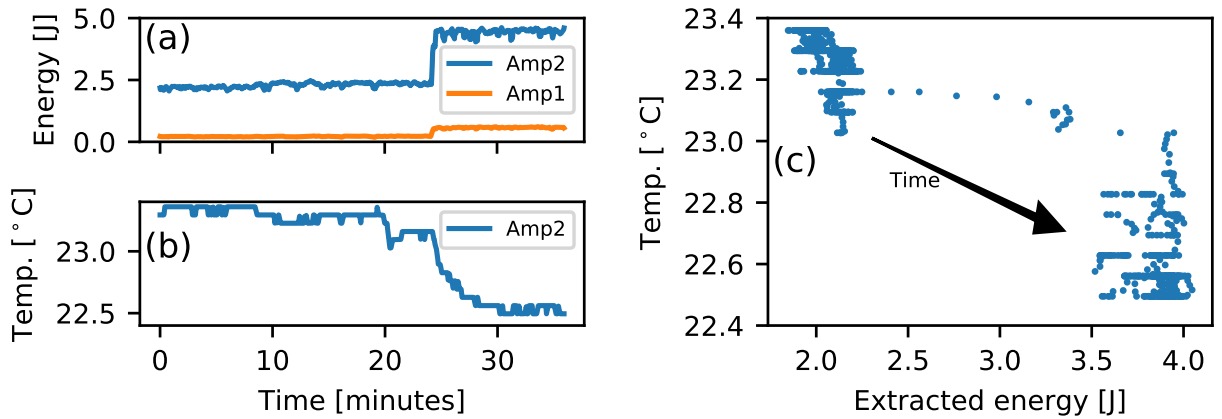


Figure 3.4: The Amp1 and Amp2 output energies are shown over time (a) with the corresponding Amp2 crystal temperature over time (b). Plotting the crystal temperature with the extracted energy from the amplifier (c) shows two specific groupings over time, corresponding to two different thermal equilibrium states.

crystal housing decreases because there is less total energy deposited as heat in the crystal, but rather converted to seed laser energy. This is reflected by two distinct operating temperatures corresponding to two distinct operation regimes with different extracted energies.

The cooling circuit itself, and also the amplifier crystals, are not operating in a completely isolated environment. Although the laser lab temperature is stabilized normally to an incredible $\pm 0.1^\circ\text{C}$, the lab operates in the real world where there are surprises. Over the span of years there have been a few brief periods where — especially during the summer — the lab air-conditioning system does not function at its peak level and the ambient temperature rises significantly. This occurs usually in parallel with operation of the highest energy pump laser (GAIA) where the load on the A/C system is largest. As the laser lab temperature increases so does the load on the cooling circuit, and the amplifier crystal temperature increases.

This can be seen in Figure 3.5 on two consecutive days. As the ambient lab temperature increased the Amp1 crystal temperature continues to increase at constant rate. This non-equilibrium state is very much undesired since it may cause changes in alignment or performance over time. As the A/C was repaired on the second day, the crystal temperature could again quickly reach an equilibrium.

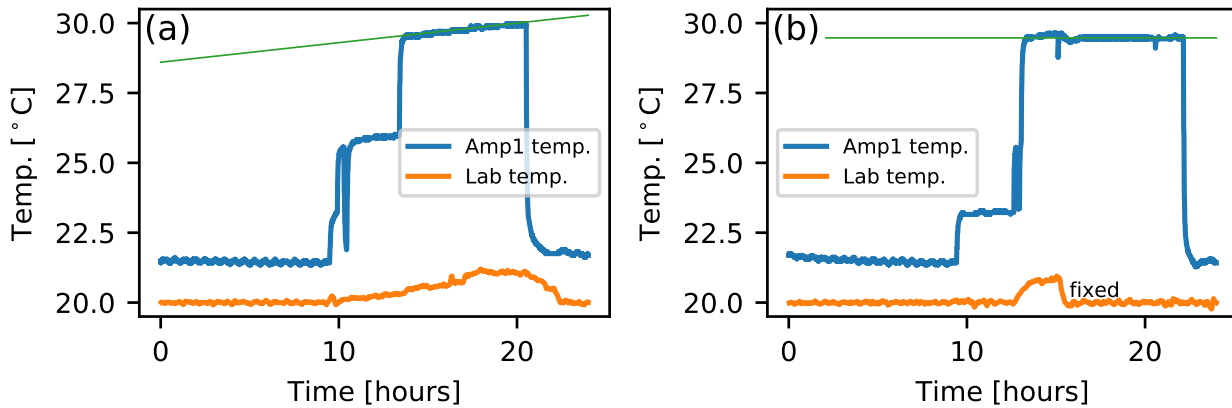


Figure 3.5: The Amp1 crystal temperature (blue) is shown over time together with the ambient temperature of the ANGUS laser lab (orange). Performance on two consecutive days showed no steady-state temperature (shown via the sloped line to guide the eye in (a)) until the laser lab temperature was stabilized via an A/C repair on the second day, and a steady state could be reached (b).

Although of course the surroundings can effect the performance of this cooling circuit, the ability of the coolant (water) to properly flow is the primary determinant of the amount of heat transfer. It was observed via the temperature sensor data that the equilibrium temperature was increasing over weeks and days. In parallel a visible decrease in the flow rate was seen on manual measurement devices. This was evidence of a blockage of the cooling circuit.

After troubleshooting various sections of the circuit a blockage was found to be in the PreAmp crystal. With further investigation it was discovered that it had reached the point of almost complete blockage of solid material. When cleaned and returned to operation the equilibrium temperature on one crystal in the circuit had decreased to below 25° C from above 30° C. This was an enormous improvement.

These three examples demonstrate how having temperature values in the control system in parallel with other laser parameters leads us to learn more about how the system operates, but also to quickly assess and narrow the source of potential or developing issues in the cooling circuits, which are crucial to operation.

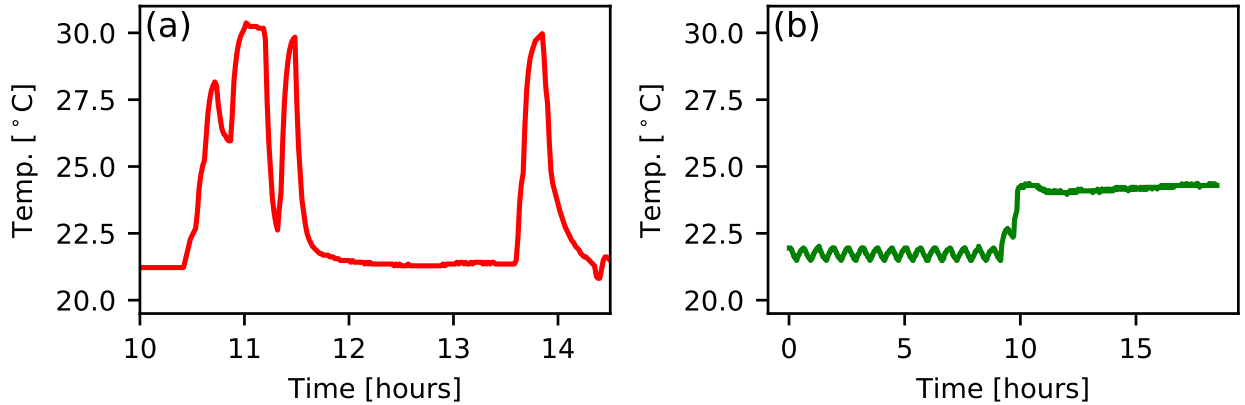


Figure 3.6: The Amp1 crystal temperature is shown on 19 July 2017 **(a)**, reaching temperatures above 30°C when all amplifiers are running. This very poor performance was due to the cooling circuit being blocked. After cleaning the cooling circuit the same crystal temperature was below 25°C in the exact same operating state **(b)** on the next day.

3.4 Design for compressed pump-probe beam for the LUX experiment

This section outlines the design of a pump-probe beam to be extracted from the main laser transport beamline, recompressed, and steered towards the interaction area of the LUX experiment. An overview of this can be seen in Figure 3.7. The use of the pump-probe beam for the LUX experiment could be many-fold: diagnosing the plasma interaction at the LUX target as can be done in many ways using a short-pulse diagnostic beam [104, 105], acting as a colliding pulse to control injection in the accelerating plasma wave [106, 107], interacting with the accelerated electrons to produce back-scattered x-ray photons [108, 109, 110, 111, 112], acting directly as a pump-probe with X-rays, or for auxiliary light-source generation (THz, HHG, OPA, etc) that could in-turn be used for a number of purposes. In the case of THz this could be for example as an electron beam probe [21] or for unique X-ray/THz pump-probe purposes [113]. It must be noted that the initial implementation will be at a limited energy so that some of the possibilities mentioned are not initially feasible. Additionally, each use case requires dedicated additional experimental and physical infrastructure that does not exist at present.

All of the use cases require very good temporal synchronization, which is why a design

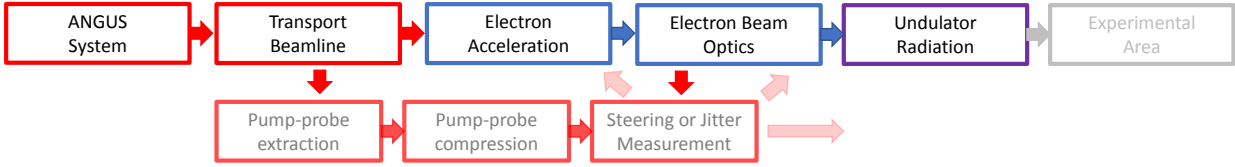


Figure 3.7: Overview of the pump-probe setup in relation to the LUX experiment. The temporal jitter measurement will be temporary, and the beam can be redirected to the electron acceleration area, or the experimental area.

for the measurement of the intrinsic temporal jitter is outlined. For the case that intrinsic temporal jitter is too large and must be actively stabilized, a design of a balanced optical cross-correlator setup is also outlined. In this case significant additional infrastructure would be needed and the performance of any active stabilization system would depend on the laser rep-rate and the frequency content of the vibrations causing the intrinsic jitter.

3.4.1 Extraction and compression

The first experimental step is to extract the beam from the 40 m ultra-high vacuum LUX laser transport beamline. This is accomplished via a 175 mm diameter 1% beamsplitter specially sourced from CVI Melles Griot to have enough bandwidth to extract the full spectrum of the driving laser. This, along with an AR-coated DN160 window have already been installed on the seventh mirror chamber in the laser transport beamline.

Then, the ~ 75 mm diameter laser will be decreased in size by a factor of six using a telescope, and steered with picomotor-enabled mirrors to further breadboards. The overall schematic of this can be seen in Figure 3.8. In the leak-through of the last mirror on this first breadboard (or via a pick-off beamsplitter) an afocal telescope with a further de-magnification of 5 would image the beam on to a NF camera to measure the beam profile and position, and a single lens will focus on to a FF camera to look at the focus and pointing. There is also the possibility to put a wavefront sensor in place to measure the wavefront of the beam (relevant for tight focusing) at the same imaged position as the NF camera.

After being steered to a second breadboard just before the target chamber, the laser will be recompressed using up to four chirped mirrors with -500 fs^2 of group-delay dispersion

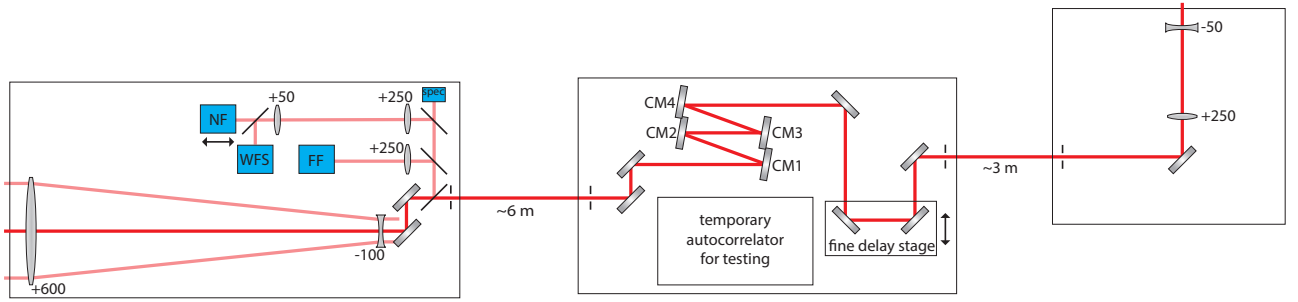


Figure 3.8: Diagram of the pump-probe extraction and recompression setup, showing the re-sizing, steering, and recompression of the extracted 1 % beam over three ceiling mounted breadboards in the LUX tunnel.

(GDD) per bounce, with 2 inch diameter. This is to compensate for the material dispersion and pulse stretching experienced via transmission through the beamsplitter, window, and telescope estimated to be between 1000-1500 fs². Finally, the recompressed pulse would be sent first to the laser outcoupling section via a third breadboard so that the intrinsic temporal jitter to the driving laser can be measured. All breadboards to mount the optics in the tunnel have already been installed on the ceiling in three locations.

3.4.2 Temporal jitter measurement

The first experimental step to assess the viability of the pump-probe beam at LUX is to measure and confirm the synchronization and jitter between the synthesized beam and the driver laser. This measurement of the synchronization must be done in a few steps.

First, the measurement on the ps level will be done with a simple electronic signal measurement using a very fast photo-diode detector and an equivalently fast oscilloscope. These components are available already in the ANGUS lab and the measurement is quite simple. To reach the fs-level synchronization and more importantly, to measure the jitter, is a more complicated and precise process.

The fs-level synchronization will be done as follows: the pump/probe beam and driver laser will overlap in a BBO crystal, which will produce sum-frequency generation light at the bisecting angle, subsequently imaged on a CCD. This is exactly the method of single-shot autocorrelation, but with two separate beams. The difference in this case is that the goal is

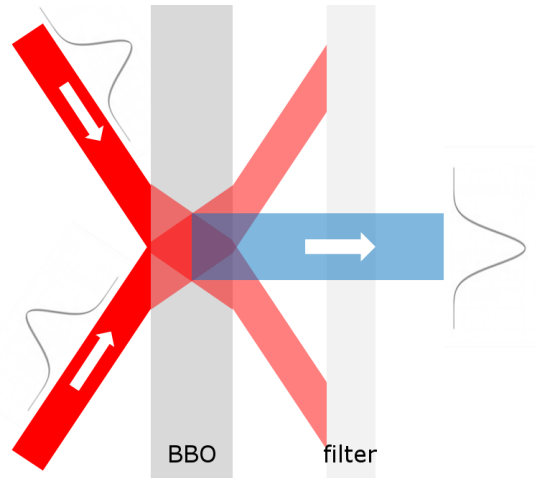


Figure 3.9: Simple and exaggerated sketch of the single-shot correlation principle. Two pulses, often a copy of the same pulse, gate each other via the sum-frequency generation in an active material (for example BBO). This allows generally for measurement of femtosecond pulses via the spatial width of the sum-frequency light, which is directly proportional to the pulse duration of the original beam. In our case, the position and the intensity of the sum-frequency can give information on the delay between the pump-probe beam and the driver laser with femtosecond precision.

not to measure a pulse duration, but to measure an offset between two pulses.

When measuring pulse duration, first the point of maximum signal is found, which corresponds to the temporal overlap of the two pulse copies. Then a calibration of the autocorrelation is done. This calibration is achieved by giving one pulse copy a known delay (simply via a translation stage) and measuring the spatial deviation of the signal on the CCD. This gives a direct pixel to time conversion, which is used to convert the width of the signal into an autocorrelation width, in units of time. Lastly, a form factor is applied to the autocorrelation width in order to finally come to the value of the pulse duration. This 'form factor' is a constant that is different depending on the temporal pulse shape assumed. For the common pulse shape of a $sech^2$ this form factor is $(1.55)^{-1}$.

In the case of measuring synchronization, or relative arrival time, it is not the width of the correlation signal that is relevant, but the position. And, very importantly, because two separate pulses are being measured that will need to be overlapped for experiments, a delay should not be purposefully introduced. The goal is to synchronize, which will be simply to get a maximum autocorrelation signal.

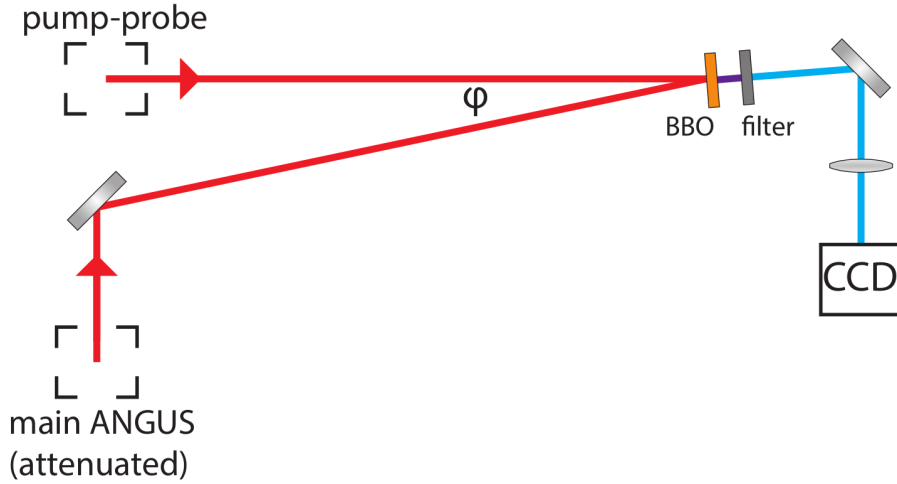


Figure 3.10: Our specific cross-correlation schematic for temporal jitter measurements. The lens will image the surface of the BBO crystal, and the angle between the beams will be made to be the minimum possible. The actual dimensions of this setup are not yet determined, so neither are the parameters such as angle or magnification.

The temporal jitter measurement, after synchronizing, depends on the fluctuation of the position of the autocorrelation signal and the proper calibration of that position. However, because a known delay won't be introduced to calculate the calibration, the calibration must be calculated from the actual geometry of the autocorrelation setup.

The relationship between timing offset and position is as follows:

$$\Delta x = \frac{c\Delta t}{2n \sin(\phi/2)} \quad (3.1)$$

Where c is the speed of light, n is the index of refraction of the BBO crystal, ϕ is the angle between the two beams, and Δt and Δx correspond to the time offset from synchronized and the distance displaced from the original position respectively. Then the measured statistics of the spatial offset, Δx , of the autocorrelation signal can be directly related to an RMS timing jitter of the pump/probe beam and driver laser.

The resolution of the timing jitter measurement depends completely on the calibration constant, as in Equation 3.2, and the imaging optics and CCD as shown in Fig. 3.10. Specifically for a setup using the refractive index of BBO:

$$\frac{\Delta t}{\Delta p} = (1.1 \times 10^{-8}) \frac{d \sin(\phi/2)}{M} \quad (3.2)$$

where M is the magnification of the imaging setup, d is the pixel size on the CCD, Δp is the offset of the autocorrelation signal in pixels, and the rest of the variables are as before.

In order to have the best resolution, the quantity $\frac{d \sin(\phi/2)}{M}$ should be minimized. In general this means the largest magnification possible, the smallest pixel size possible, and the smallest angle possible between the two beams.

It is not reasonable to say the largest or smallest possible, since there are practical limitations on the CCD pixel size and imaging setup dimensions, and an actual estimate should be done. If, for example, the imaging system is 10x magnification, the angle between the two beams is 20° , and the pixel size of the CCD is $1.67 \mu\text{m}$ then the resolution is 0.32 fs/pixel . This is a reasonable resolution, which would allow for timing jitter at or below 10 fs to be observed. It is very possible, that with only $\sim 10 \text{ m}$ of separate propagation that the beams will be intrinsically synchronized to below 10 fs, which would then be within bounds for what is needed for first experiments [114]. If the intrinsic synchronization level were not at the 10 fs level, then further improvements would be necessary, one of which is active path-length stabilization.

3.4.3 Optical-to-optical jitter stabilization

If the intrinsic temporal jitter between the high energy driving laser and the pump-probe beam were significantly above the sub-10 fs level defined as needed for experiments, additional investment would be needed. Although this is beyond the scope of this thesis, a simple design is outlined here. The stabilization would be in the form of a system to electronically measure the temporal jitter and to use that electronic signal to drive a motorized translation stage. The balanced optical cross-correlator (BOC) is a method to measure the synchronization and temporal jitter between two ultrashort pulses, with a linear sensitivity ideal for closed-loop stabilization [115].

The general schematic of a BOC consists of two separate cross-correlators, where one of the pair introduces a temporal delay on one of the pulses (on the order of the pulse duration),

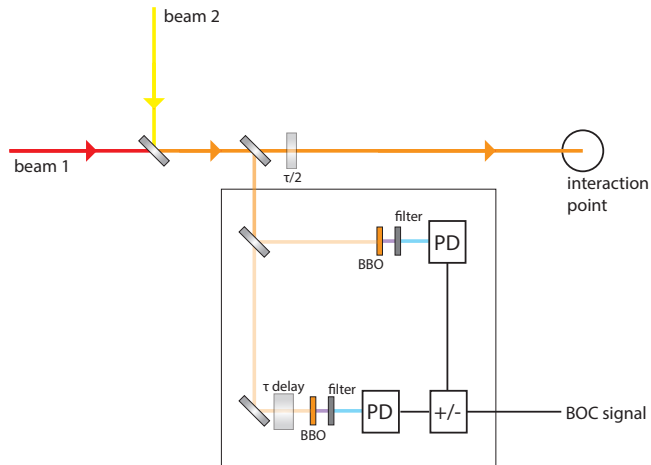


Figure 3.11: An example schematic for a BOC where the two beams to be jitter stabilized are colinear and have different frequencies. This allows them to be analyzed in each cross-correlator also colinear, getting rid of the second harmonic light from each beam using a simple filter and leaving only the sum-frequency light. The 'interaction point' is only a placeholder, for where an interaction requiring such high synchronization would take place.

shown in Fig. 3.11. In one of the arms one pulse arrives earlier and in the other arm that same pulse arrives later. In the path of the beams towards the interaction there must indeed be a similar fixed delay of $1/2$ that in the cross-correlator. Only with this additional delay arm the pulses overlapped on the interaction when the BOC is balanced.

The cross-correlators are operating using some physical mechanism for the correlation. This is most often sum-frequency generation (SFG), but can also be different nonlinear effects, for example a parametric process [116]. The remainder of this section is written as if the mechanism is SFG.

The signal of a given cross-correlator is maximum when the two incident pulses *within only this cross-correlator* are exactly overlapped in time. This is precisely analogous to the pulse duration measurement method of a scanning autocorrelator. When the pulses *within only this cross-correlator* are then delayed relative to each other the signal is lower. If these pulses are symmetric then the behavior of this cross-correlation signal should also be symmetric, again similar to the scanning autocorrelator.

The BOC signal is produced by the difference of two cross-correlators, wherein one of them has a given positive and constant introduced time delay of the pulses relative to each

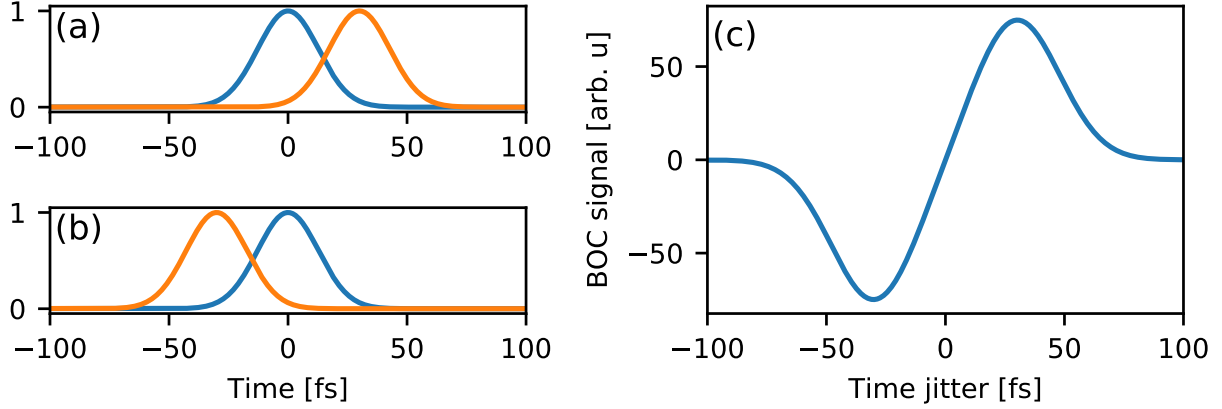


Figure 3.12: Example of an ideal BOC signal, given pulses of the same duration and energy. The pulses of 30 fs duration are offset by a constant $\tau_d/2$ in the first arm **(a)** and offset by the opposite time in the second arm of the BOC **(b)**. The expected behavior of the BOC with a given relative temporal jitter Δt **(c)** showing a linear behavior at the zero-crossing.

other, $\tau_d/2$ and the other has an equal and opposite offset. When the temporal jitter Δt is in one direction one of the cross-correlator arms will have a larger signal. Each cross-correlator should have same intensity in order to have the best timing jitter resolution, hence the naming "balanced". The signal can be explained by the following equation, and is shown exactly in the same form in the right-hand plot of Fig. 3.12.

$$\text{signal}_{\text{BOC}}(\Delta t) \propto \left[\int_{-\infty}^{+\infty} I_1(t - \Delta t) I_2(t - \tau_d/2) dt - \int_{-\infty}^{+\infty} I_1(t - \Delta t) I_2(t + \tau_d/2) dt \right] \quad (3.3)$$

This equation ignores any constants which would come from the sum frequency generation (χ_2 , etc), the photodiode efficiency or the circuitry, and generally assumes that these are the same in each arm of the BOC. Note that τ_d should be of the same order of the duration of the pulses in order to have a measurable signal, but also to have a reasonable slope and therefore resolution in the region where they are overlapped. Not all of the nuances are explained here of course.

The BOC signal essentially maps a given range of delays between pulses to a unique electronic signal amplitude, with very high accuracy. When the electronics are fast enough, one

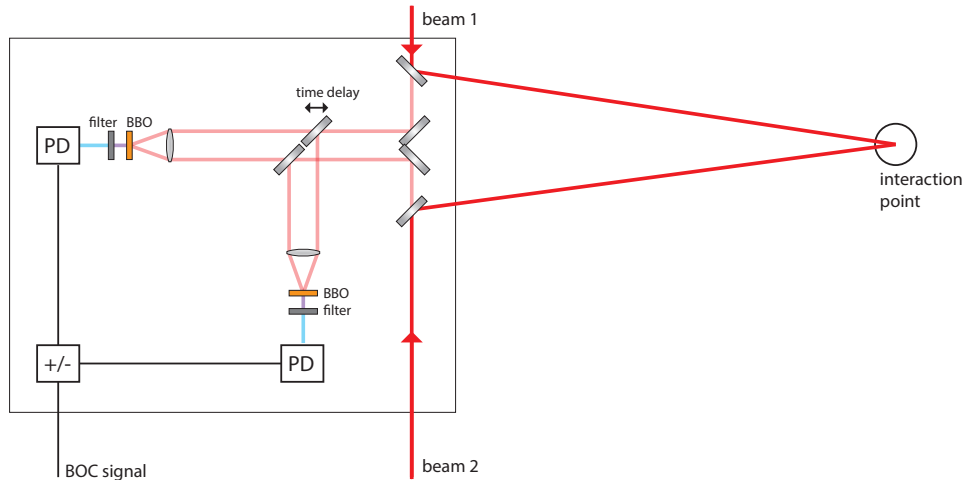


Figure 3.13: An example schematic for a BOC where the two beams to be jitter stabilized are not colinear and have the same frequency.

can then directly measure the delay between pulses in two separate beams for every pulse in the pulse train. If these pulses are already stabilized to each other then the value of the BOC signal would of course not change, and would only represent a constant delay. However, if there is relative statistical jitter, whether caused by a physical mechanism within the independent light sources themselves or purely from vibrations, air fluctuations, etc. then the BOC would show this with a fluctuating electronic signal amplitude. There are more complex or specific BOC configurations, for example with a single crystal [117].

Note that an intensity cross-correlator itself can also in principle measure the delay of pulses to a high accuracy, but it is not as useful as the BOC. This is because a cross-correlator is symmetric around the zero delay position (an even function), and therefore also has a minimum at the zero delay position. This means that there is no ability to discern positive or negative delays from each other, and that the signal is quite insensitive to delay exactly in the most important region. Therefore the method to measure the rms temporal jitter outlined in the previous section is not suited to compensating for that jitter. The BOC signal is an odd function and therefore has an approximately linear slope at the zero delay position. This solves both of the mentioned issues.

An additional level of complexity is added when the beams that should be synchronized and jitter stabilized are not colinear and have the same frequency. For high-power laser systems

this is almost always the case, since the pump-probe beam originates from the driving laser it has the same frequency, and because the pump-probe beam is not taking part in the initial interaction it must by constraint not be colinear (there are some diagnostic configurations that are colinear or are frequency-doubled for example, but the point is that these are not typical or all-encompassing).

In this more complex situation, the setup for a BOC becomes similarly more complex. The geometry of the two cross-correlators is not colinear, and the time-delay can no longer just come from a dispersive material. The resultant setup can be seen in Fig. 3.13. This is noticeably different than in Fig. 3.11, the more standard setup, but is tractable nonetheless.

The last and final step to stabilize the jitter that is measured by the BOC, would be to use the complete knowledge of the fluctuations at the full rep-rate to pre-compensate in a closed-loop topology. This takes the form of the combination of a BOC and a fast motorized delay stage, located before the position where the BOC measures, which can in the end compensate for fluctuations at some rep-rate below the full rep-rate of the beams (i.e. the Nyquist limit). This has been achieved with more complex schemes for cross-correlation for the application of single-cycle optical waveform synthesis [118, 119]. This would be a possible step in this case if the measured temporal jitter in the LUX pump-probe beam is outside of the desired range, but only if the oscillations are very slow. If the measured temporal jitter has characteristic frequencies above single Hz (which is very likely) then the jitter stabilization system would require some higher rep-rate femtosecond laser that propagates over the independent paths of the driver laser and pump-probe laser. Needless to say this would be a significant investment, and is beyond the scope of this thesis.

Chapter 4

Narrowband terahertz generation in PPLN with ANGUS

This chapter is a reproduction — with additional content (Sections 4.2.1 and 4.3.2, Figures 4.5, 4.6, and 4.8 and accompanying text) and text and style changes — of work already published in Optics Letters in June 2017 entitled "Narrowband terahertz generation with chirped-and-delayed laser pulses in periodically poled lithium niobate" [85]. Credit is given to all co-authors, especially F. Ahr, whose dissertation should be additionally referenced for details [120]. The author of this thesis contributed crucially to the experimental work, analysis, and drafting of the Optics Letters manuscript and all additions and changes within this thesis chapter are original.

The previous chapter outlined the Angus laser system and the improvements in diagnostics principally for laser-plasma acceleration. However, the properties of the laser system, specifically high energy and broad bandwidth, make it very useful for various other mechanisms. This chapter and the rest of the thesis outline the use and optimization of the chirped (stretched) ANGUS pulses for terahertz (THz) generation.

The last couple of decades have seen a tremendous surge in development of terahertz sources of high-energy and high-peak-field for applications ranging from linear and nonlinear THz spectroscopy [121], to compact, THz-based electron acceleration [15]. For spectroscopic applications, the low energy of THz photons enables gentle pumping for time-resolved pump-probe studies of material properties, while for electron accelerators, the millimeter scale of THz radiation offers the advantages of compactness and high-acceleration gradients which are beneficial for driving ultrashort X-ray sources. Optical sources of THz pulses based on difference frequency generation (DFG) are exceptionally promising for these applications due to the high efficiencies, high peak fields and high degree of tunability they offer. With the development of the tilted pulse-front technique [42, 47, 48], percent level optical-to-THz conversion efficiencies have been achieved — using Fourier limited broadband near-infrared (NIR) drivers

incident on bulk lithium niobate (LiNbO_3 , LN) — enabling generation of single-cycle pulses in the mJ-range. By comparison, the development of equivalent sources of multi-cycle THz pulses has lagged behind. Multi-cycle pulses, which have narrower bandwidths and accordingly longer pulse durations, offer complementary parameters relative to single-cycle pulses, and are advantageous for applications such as driving compact linear accelerators [13, 14] and tuned excitation of specific material transitions. Recent work in THz generation has therefore seen a greater emphasis on development of efficient multi-cycle sources.

Among the primary challenges are achieving high conversion efficiencies and scaling to high energies. High efficiencies in nonlinear optical conversion processes require high incident optical intensities and management of the phase mismatch between optical and THz waves, which tends to be large in most nonlinear materials due to differences in the linear index for the two waves. Quasi-phase-matching in periodically poled lithium niobate (PPLN) has emerged [71, 75, 86] as a promising candidate for phase matching in narrowband THz generation due to the large second order susceptibility, χ_2 , of lithium niobate. Recently, conversion efficiencies up to 0.12 % and THz energies of $\sim 1 \mu\text{J}$ were demonstrated by using Fourier-limited femtosecond pump pulses with optimized bandwidths and by using cryogenic cooling to minimize THz absorption in the PPLN crystal [76]. To produce the mJ-level THz pulses needed for acceleration applications [15], however, pump pulses in the range of 1 J are required. But scaling to Joule energies with short pump pulses is problematic because the energy that can be applied to the nonlinear crystal is limited by the intensity threshold for optically-induced damage and by the limited aperture of commercially available PPLNs. A solution is thus to increase the pump pulse duration to allow greater energy to be carried, since the damage threshold is increased at large pulse durations.

Chirping, i.e. temporally stretching of the IR pump, as proposed in [86, 34], offers one method to increase the pulse duration and therefore scale up the pump-pulse energy. A side effect of chirping, however, is that the instantaneous spectral content of the optical pulse is reduced, limiting the nonlinear conversion process that requires optical photons with frequencies separated by the frequency of the generated THz to be overlapped in both space and time. This effect can be compensated by adding a second chirped pulse with an appropriate delay to provide the required instantaneous spectral content.

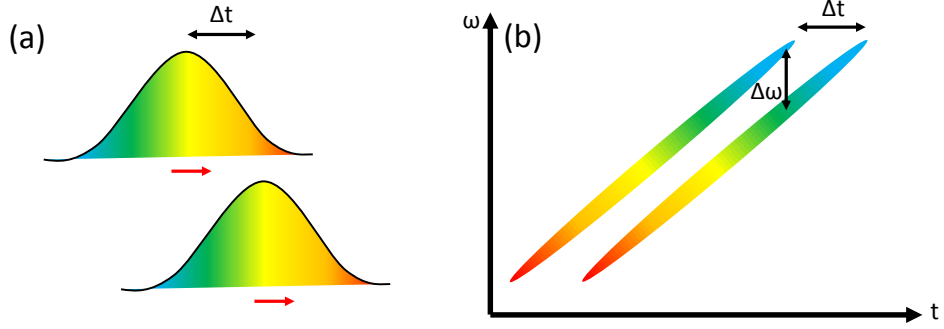


Figure 4.1: **(a)** Conceptual temporal arrangement of collinear chirped-and-delayed pulses. **(b)** Wigner-plot illustrating the spectral content of the chirp-and-delay pulses vs. time. $\Delta\omega$ represents the instantaneous optical frequency difference between the two pulses and Δt is the relative time delay.

4.1 Concept of chirp-and-delay

The chirp-and-delay concept was first described in 1994 to produce tunable, narrow-band THz waves via photo-conductive antennas [78]. Chirp-and-delay has been used to produce higher energy pulses of $10 \mu\text{J}$ [80] in a hybrid approach employing the tilted pulse front technique, however, these pulses contained only 10 optical cycles and is thus not ideal for applications requiring very narrow-band radiation, for example electron acceleration. Here, the use of chirp-and-delay in combination with a periodically poled medium is demonstrated for the first time and whereby record energies of narrow-band multi-cycle THz radiation were generated. PPLN crystals were investigated with varying poling periods and lengths and the effect of cryogenic cooling on the conversion efficiency was studied.

DFG requires the presence of two distinct frequency components overlapped in space and time. These components can be provided by a single pulse of sufficiently large bandwidth or by two narrow-band pulses with distinct central frequencies. In the chirp-and-delay concept, two narrow-band components are provided at a given time by broadband but chirped pulses combined with well-defined temporal delay Δt , as schematically illustrated in Fig. 4.1(a). In this case, the instantaneous frequency of each pulse varies essentially linearly in time, but the instantaneous frequency difference $\Delta\omega$, is fixed by the delay and the chirp rate as shown in Fig. 4.1(b).

The delay can then be tuned so that $\Delta\omega(\Delta t_{\text{opt}}) = \Omega$, where Δt_{opt} is the optimal delay

to achieve the desired THz angular frequency Ω . Assuming a second order spectral phase coefficient, i.e. group-delay dispersion (GDD) ϕ_2 , which is equivalent to a linear chirp rate of $1/\phi_2$, the optimum delay is

$$\Delta t_{\text{opt}} = \Omega\phi_2. \quad (4.1)$$

Optimizing THz generation in periodically poled crystals requires $\Delta\omega$ to be tuned to the phase matched THz angular frequency Ω , which is primarily determined by the poling period according to

$$\Omega = \frac{c}{\Lambda|n(\Omega) - n_g|}, \quad (4.2)$$

with c the speed of light, Λ the poling period, and $n(\Omega)$ and n_g are the phase and group refractive indices for the THz and NIR waves respectively [122, 123]. To a lesser extent Ω is also determined by the temperature through the temperature-dependent indices of refraction [72, 74, 76]. The relative THz bandwidth $\delta\Omega/\Omega$ and hence the number of cycles generated N of THz produced when quasi-phase-matched can be approximated by: $\delta\Omega/\Omega = \Lambda/L \propto 1/N$, where L is the crystal length [86, 124]. By contrast, in bulk LN the THz pulse length, and thus the number of optical cycles, is directly determined by the IR pulse duration [80].

4.2 Experimental overview

Experiments were done using the ANGUS 200 TW double CPA, Ti:Sa-based laser system providing up to 6 J pulses at 5 Hz, compressible to 25 fs, outlined in the previous chapter. The spectrum was centered at 800 nm with a FWHM bandwidth up to 35 nm, resulting in chirped pulses up to 260 ps FWHM duration resulting from a GDD of $\phi_2 = 2.3 \text{ ps}^2$. The experiments used the output of Amp1, which has a maximum energy of 1.2 J in this case, but the maximum energy used for the results in this chapter was below 300 mJ due to constrictions on the crystal size and allowable fluence.

A train of pulses of identical, nearly linear chirp and tunable delay was created from the uncompressed beam by using a 38 % partial reflector (PR) mounted on a delay stage with the

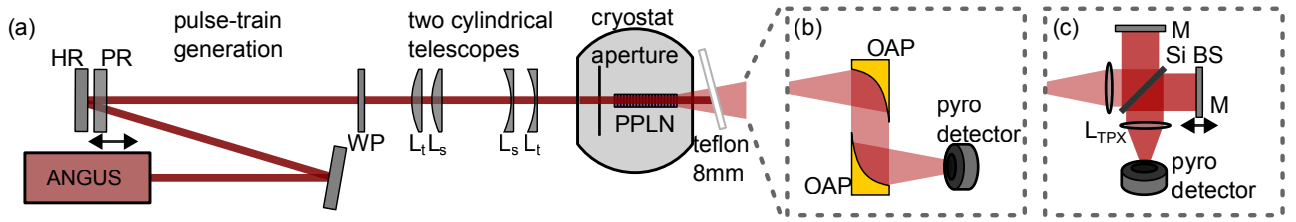


Figure 4.2: **(a)** Chirp-and-delay setup using a combination of partial reflector (PR) and high reflector (HR) to generate a chirped pulse pair plus lower-energy trailing pulses. **(b)** THz pulse energy measurement setup. **(c)** THz frequency measurement setup based on a Michelson interferometer. **KEY:** WP: half wave-plate; L_s : sagittal lens; L_t : tangential lens; OAP: off-axis parabola; L_{TPX} : TPX lens; M: Silver mirror; Si BS: silicon beam splitter.

PR coating facing a high reflector (HR), as shown in Fig 4.2(a). This combination resulted in two pump pulses of approximately equal intensity followed by a series of pulses with significantly lower energies originating from the multiple reflections. The energy of the pulses was tuned using a waveplate and two thin film polarizers (not shown), while a second half-waveplate (WP) matched the polarization of the chirped-and-delayed pulses to the optical axis of the PPLN. Two cylindrical telescopes matched the beam shape to the clear aperture of the PPLN: the tangential and sagittal telescopes reduce the vertical and horizontal beam size to 3 mm and 10 mm, respectively. The PPLN was mounted in a cryostat for cryogenic cooling using liquid nitrogen to reduce THz absorption in the crystal. A ceramic aperture installed inside the cryostat just in front of the PPLN input surface mitigated the heat load and acted as a mask to shape the beam and ensure it wasn't clipped by the crystal. The entrance and exit ports of the cryostat were fused silica windows anti-reflection (AR) coated for 800 nm. The transmission ratio of the windows for THz pulses was calibrated independently, and was found to be 80 % in our frequency range.

4.2.1 Detector calibration

Due to the inherent rep-rate of the ANGUS laser system, the rep-rate of THz generation is of course fixed to exactly 5 Hz. This is quite an unusual rep-rate for THz generation since most sources are very low pulse energy, but at kHz or higher repetition rates. Therefore generic THz detectors are optimized and calibrated to work at these higher rep-rates, detecting the average power rather than single pulse energy.

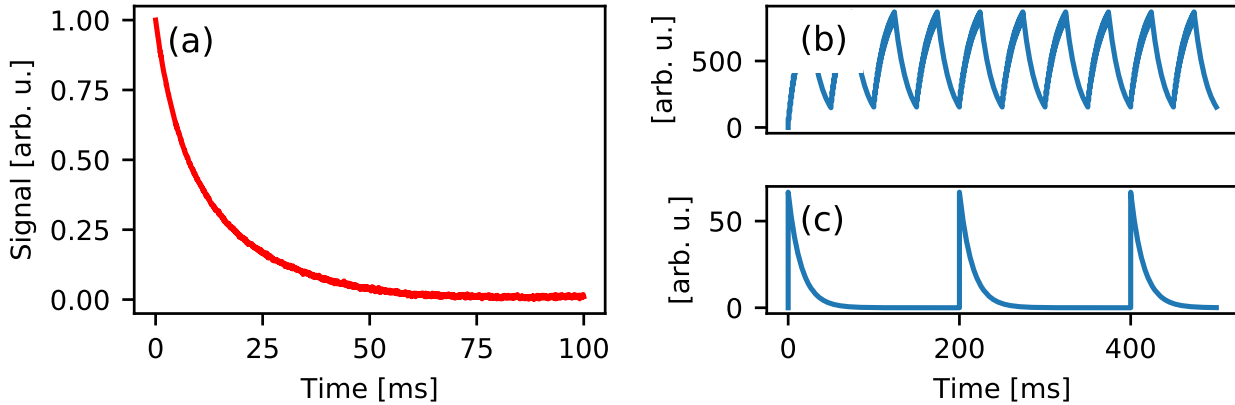


Figure 4.3: An example of the measured fall time of the pyro-electric detector **(a)**, which has a 15 ms fall-time averaged over hundreds of examples. The simulated response at a laser rep-rate of 1 kHz chopped to 20 Hz **(b)** is compared to a signal at 5 Hz **(c)** to calibrate the detector for experiments using ANGUS.

Our pyro-electric detector (Gentec-EO: THZ9B-BL-BNC) was calibrated specifically for 1 kHz rep-rate chopped at rep-rates of 5, 10, 20, and 25 Hz. This calibration is a simple nW/mV conversion for the peak-to-peak amplitude of the detector. Because the pyro-electric effect works in this case as a simple response to an impulse, the detector can be modeled using the measured response time to calculate the response of the detector to a single pulse of THz radiation.

Figure 4.3(a) shows an example of the measured response time of the detector to a single THz pulse. This was measured to be 15 ms by averaging the fit exponential curve to hundreds of examples of such a response. Figure 4.3(b) shows the simulated response to a 1 kHz signal, which agrees well with actual measurements, and Figure 4.3(c) shows the simulated response to a single pulse using exactly the same simulation parameters. The ratio of this peak-to-peak signal in the simulations gives us the ratio to be applied to the original calibration number to calibrate the detector for single pulses. This calibration is used in the rest of this work and was confirmed with experimental data from N. Matlis.

4.3 Experimental results

THz was generated using PPLN crystals of four different poling periods: $\Lambda = 125 \mu\text{m}$, $212 \mu\text{m}$, $330 \mu\text{m}$, and $400 \mu\text{m}$, obtained from HC Photonics (excluding the PPLN at $330 \mu\text{m}$, which is provided by Prof. T. Taira). To measure the THz pulse energy, two gold-coated off-axis parabola of 4" focal length were used to collect the THz and focus it onto a pyro-detector (Gentec-EO: THZ9B-BL-BNC). In an interchangeable setup, the frequency of the THz could also be measured using a Michelson interferometer with a 3.5 mm thick silicon wafer as a beamsplitter and a variable delay in one arm. The THz was collimated into the interferometer using a 150 mm focal length TPX lens. The interference pattern was then determined by focusing the THz with a second TPX lens onto the pyro-detector and scanning the variable delay. An 8 mm thick Teflon plate was used to dump the IR pump before the THz detection setups and to allow measurement of the transmitted optical spectra using an HR4000 fiber spectrometer (Ocean Optics).

In order to verify the chirp-and-delay mechanism the dependence of the optimum delay on the frequency of the generated THz was measured, which, from Eq. 4.1, is expected to be linear. The THz frequency was varied by using crystals of different poling period, and the THz output was then measured as a function of the delay (by scanning the position of the PR) for each of the four poling periods (Fig. 4.4). Panel 4.4(a) shows that the optimum delay depends inversely on the poling period, as expected from Equations. 4.1 and 4.2. The development of additional substructure for larger poling periods is noted, which is attributed to the presence of residual third-order dispersion in the chirped pulses and the presence of a pulse train from the HR/PR combination rather than the ideal case of two isolated pulses. A detailed analysis of these effects has been done, and will be presented in the following chapter.

The connection between the poling period and the THz frequency is well established, and has been measured previously [73, 76]. For completeness, however, the frequency of the THz generated by the $330 \mu\text{m}$ and $212 \mu\text{m}$ poling period crystals (which produced the larger signals at cryogenic temperatures) was measured using the interferometer (Figs. 4.4(b) and (c)). Using sinusoidal fits, THz wavelengths of 0.83 mm and 0.55 mm, corresponding to frequencies of 0.361 THz and 0.544 THz were determined, in good agreement with the values of 0.370 THz and

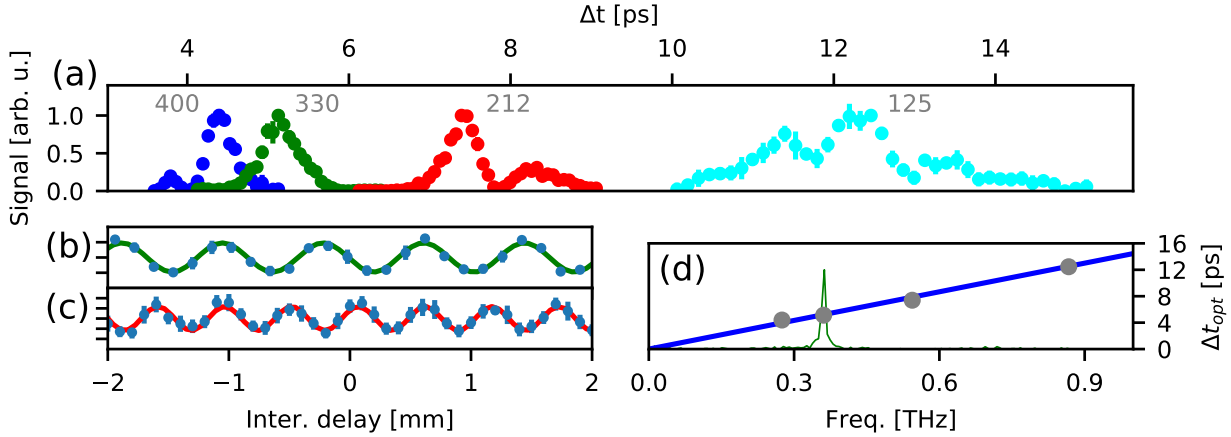


Figure 4.4: Delay scan results. **(a)** Normalized THz signal vs. delay for PPLN poling periods of 400 μm , 330 μm , 212 μm and 125 μm . **(b)** & **(c)** Interferometer data (dots) and sinusoidal fits (lines) for crystals of poling period 330 μm and 212 μm yielding THz wavelengths of 0.83 mm and 0.55 mm, respectively. **(d)** Comparison of measured (grey dots) and predicted (blue line) optimum delays for four poling periods. In this case the 330 μm and 212 μm were at 80 K, and therefore produced slightly higher frequencies than at room temperature.

0.574 THz, respectively, predicted by Equation 4.2 and using IR refractive indices from [125] and THz refractive indices from [126] extrapolated to 80 K. Wu et al., 2015 [126] is used as the benchmark in this thesis, but there are variations in reported indices of refraction and absorption coefficients for THz in the literature, especially at low temperatures [127, 45, 128, 126]. This could be a source of error and will be discussed at more points in this chapter and thesis. For the 125 μm and 400 μm poling period crystals, which produced lower THz signal levels and were therefore not possible to measure in our interferometer, values were used for the frequencies of 0.867 THz and 0.275 THz respectively, which were measured using the identical crystals in a previous work [76].

The dependence of the optimal delay on THz frequency is plotted in Figure 4.4(d). The measured delays (grey dots) agree well with the prediction based on Equation 4.1 and using the GDD of the ANGUS system, verifying the chirp-and-delay mechanism. For example, the 330 μm poling period crystal had a measured optimum delay of $\Delta t = 5.13$ ps in very good agreement with the predicted delay of 5.22 ps at 0.361 THz.

The THz output as a function of frequency (at constant fluence) should have a peaked

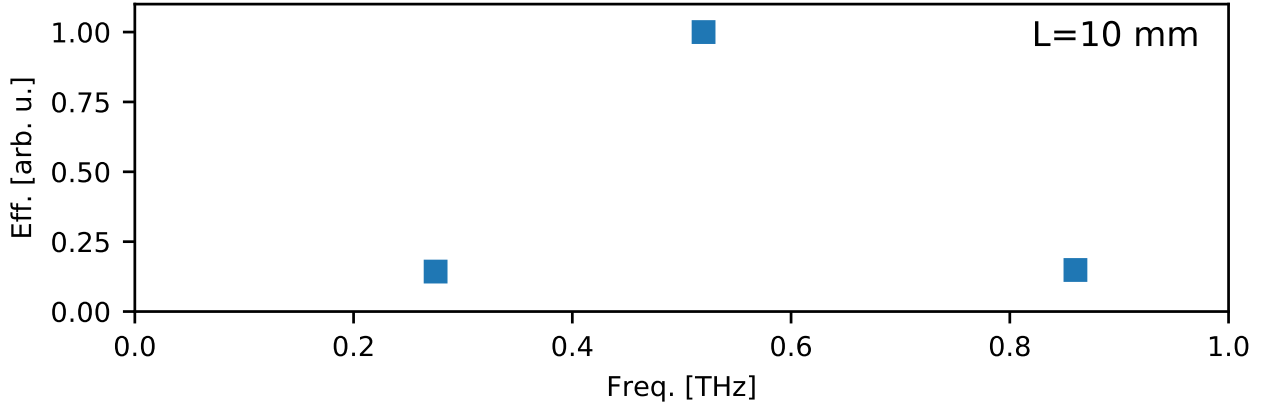


Figure 4.5: Scaled THz output for three different frequencies at room temperature (produced via poling periods of $400 \mu\text{m}$, $212 \mu\text{m}$ and $125 \mu\text{m}$ all at 10 mm length). This shows the peaked behavior at around 0.5 THz, which is predicted by analytic theory.

behavior at around 0.5 THz due to the interplay between frequency and absorption. Crystals of 10 mm length for the three poling periods of $400 \mu\text{m}$, $212 \mu\text{m}$ and $125 \mu\text{m}$ were used in this case. Comparing the output (at room temperature only still) and using the frequencies of 275 GHz, 520 GHz, and 860 GHz a clear peak can be seen in the measured output in Figure 4.5.

Because the efficiency was highest at the intermediate frequency, the output at high pump fluence was studied specifically with crystals of $212 \mu\text{m}$ poling period only.

4.3.1 THz output energy and conversion efficiency

The chirp-and-delay scheme was then optimized by studying the THz output as a function of the incident pump fluence for varying crystal temperatures and interaction lengths. To distinguish between the intrinsic performance of the scheme and engineering factors such as transport of THz to and from the crystal or Fresnel losses at the surfaces, the performance was characterized using two primary metrics in this chapter: 1) the internal conversion efficiency (hereafter in this chapter, "efficiency"), defined as the ratio of the THz energy before exiting the crystal rear surface and the IR input energy after entering the crystal front surface and 2) the THz energy extracted from the crystal.

The first result is the behavior of the THz generation efficiency as crystal length is

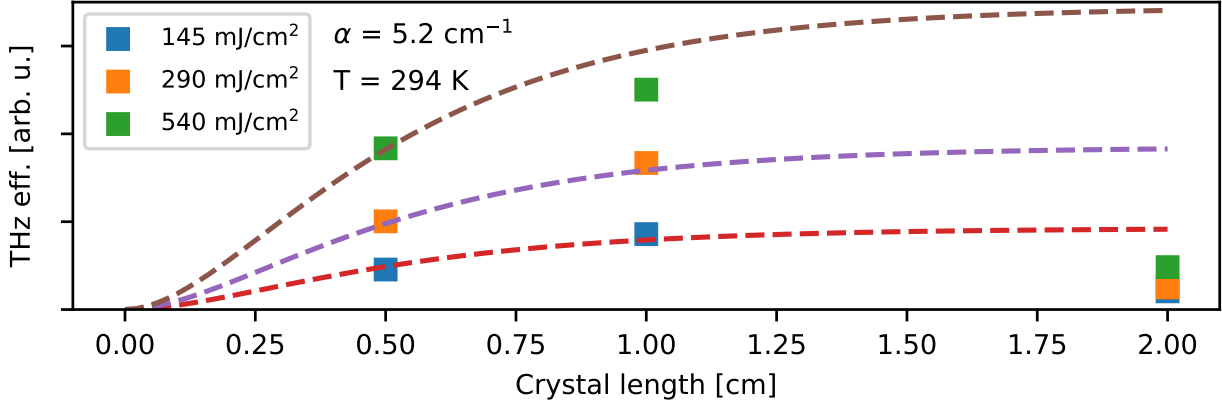


Figure 4.6: THz efficiency for three different length crystals all at room temperature with $212 \mu\text{m}$ poling period. Three fluences are shown (squares) along with the analytic theory curve (dashed lines) using an absorption of 5.2 cm^{-1} from [126]. This agrees quite well for the two lower fluences for the 5 mm and 10 mm length, but in all cases the 20 mm length crystal had significantly lower efficiency than expected.

changed. Figure 4.6 shows the efficiency at room temperature for the three crystals available of 5 mm, 10 mm, and 20 mm length. Three fluences of 145, 290, and 540 mJ/cm^2 are shown, and in all three cases the efficiency with a 10 mm crystal was only slightly higher than with 5 mm, and the efficiency with 20 mm length was significantly lower. The former behavior can be explained by the high absorption coefficient in PPLN at room temperatures. Using a value of $\alpha=5.2 \text{ cm}^{-1}$ for the absorption coefficient, computing the analytical curve of the form $([1-\exp(-\alpha L/2)]/\alpha)^2$, and scaling the curve according to the fluence it can be seen that the dashed lines in Figure 4.6 agree well with the measurements.

However, the low efficiency with 20 mm cannot be explained by the analytic form, since it is lower than at 10 mm. This must be due to the effect of the absorption of THz along the length, modifying the spectrum of the IR pulse and thus decreasing the ability of the IR pump to produce THz after a certain length. There is no direct evidence for this, but the signs of cascading that will be shown shortly corroborate that the modification of the spectrum does indeed occur. The fact that the data point at 10 mm and 540 mJ/cm^2 is also less than the analytical curve may be evidence of this effect occurring even at that length once the fluence gets high enough. Another way to phrase this is that once the efficiency or total absorbed THz

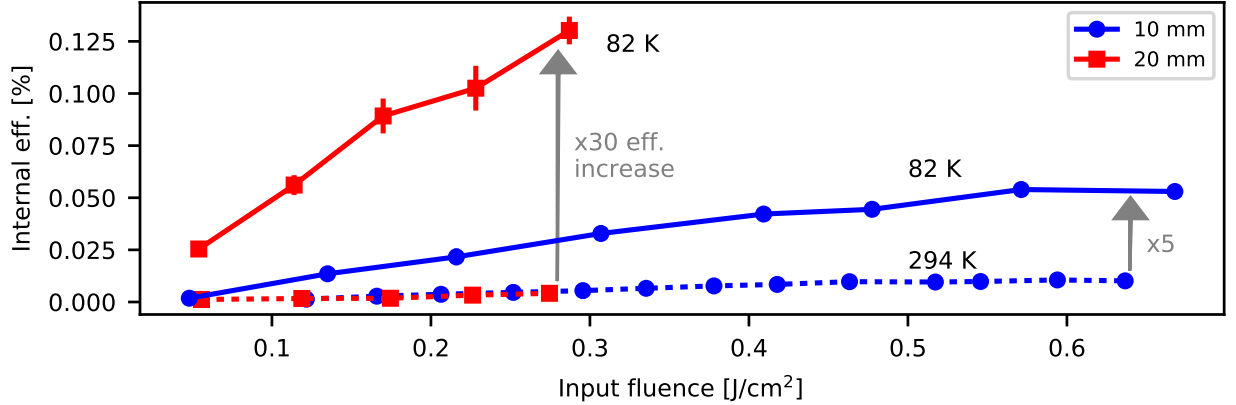


Figure 4.7: Conversion efficiency of 212 μm poling period PPLNs at room- (dotted) and cryogenic (solid) temperature as a function of pump fluence, showing drastic improvement with cooling.

gets large, either by increasing the fluence or the length or both, the THz output cannot be accurately predicted by the analytic equations.

In order to increase the output, both at longer lengths and in general, the crystals were cooled with liquid nitrogen in order to decrease absorption. Figure 4.7 shows the internal conversion efficiency vs. incident pump fluence at room and cryogenic temperatures for two crystal lengths of 212 μm -poled PPLN.

At room temperature (294 K), the efficiency is similar for the 10 mm and 20 mm long crystals as already mentioned. This large absorption coefficient limits the effective interaction length to only a few millimeters for both crystals [73, 76]. Therefore at room temperature the process is absorption dominated. By cooling the crystals to 82 K the absorption coefficient was reduced to 2.6 cm^{-1} (according to [126]), which significantly increased the effective interaction length, allowing greater advantage to be taken of longer crystals and thus improving the conversion efficiency. Compared to room temperature, the cryo-cooled 10 mm long crystal showed a five-fold increase in conversion efficiency, while the 20 mm long crystal showed a 30-fold increase, demonstrating the exponential benefits of reducing the THz absorption. This clear increase in efficiency with longer crystals when cryo-cooled is in stark contrast to QPM in PPLN when pumped with compressed pulses [76]. This is a demonstration of the advantage

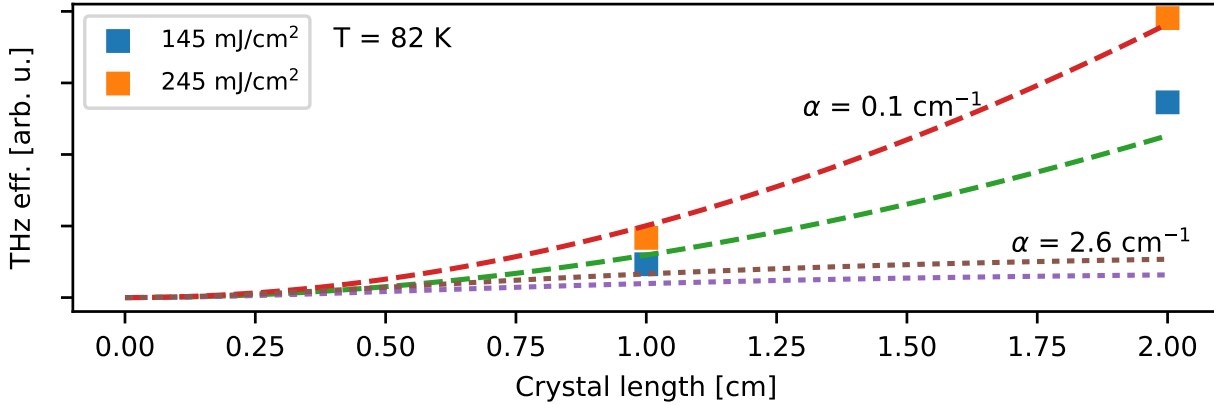


Figure 4.8: THz efficiency for two different length crystals at cryo temperature with $212 \mu\text{m}$ poling period. Two fluences are shown (squares) along with the analytic theory curve using both an absorption of 2.6 cm^{-1} from [126] (dotted lines), and of 0.1 cm^{-1} (dashed lines). It is clear that the lower absorption coefficient agrees more closely for both fluence levels.

of avoiding strong nonlinear effects when pumping with stretched pulses.

For the 10 mm crystal the internal efficiency saturated at a value of 0.054% at a pump fluence of 0.571 J/cm^2 , well below the damage threshold. For the 20 mm crystal in contrast, damage was observed at a lower threshold than expected, and limited the internal efficiency to 0.13% at a pump fluence of 0.287 J/cm^2 , where saturation had not yet occurred. It is unclear if the difference in damage threshold is attributable to a difference in the nonlinear interaction or in the quality of the crystal.

A record multi-cycle THz energy of $40 \mu\text{J}$ was achieved at a frequency of 0.544 THz , using the 10 mm, $212 \mu\text{m}$ -poled PPLN crystal (with an aperture of $3 \text{ mm} \times 10 \text{ mm}$) at cryogenic temperature. Although the 20 mm piece exhibited a higher peak efficiency, the energy output was limited to $12.8 \mu\text{J}$ by a smaller aperture of 3 mm diameter.

Returning to a similar analysis of the THz efficiency with length, one can compare the expectations of the analytical theory to the experiment now at cryo-temperature. A similar plot as previous can be seen in Figure 4.8. In this case there are only two lengths of 10 mm and 20 mm, and only a fluence up to 245 mJ/cm^2 can be compared due to the damage in the longer crystal.

The important result, already communicated via the very high efficiency, is that with length the output increases (at least up to 20 mm). However, the increase when at 80 K from 10 mm to 20 mm cannot be properly predicted with the analytical behavior and the absorption coefficient of 2.6 cm^{-1} from [126]. Only when using a purposefully lower absorption coefficient of 0.1 cm^{-1} do the results make sense (Fig. 4.8, dashed lines). Additionally, the efficiency data in Figure 4.8 is scaled exactly the same way as the data at room temperature in Figure 4.6, so this lower absorption coefficient is also needed to explain the amount of increase from room temperature to cryo-temperature *at each length*. Therefore, it is clear that there is a discrepancy in the absorption coefficient data from the literature. It could be that this varies with each individual sample, since it is already known that the properties depend on the doping level of magnesium oxide (used to increase the damage threshold) [127, 128]. For lack of a known resource that is correct at all temperatures and frequencies, Wu, et al. [126] will continue to be used as the benchmark in this thesis.

4.3.2 THz output during cooling

The increase in THz output energy when cooled to temperatures around 100 K is a crucial result, especially in the longer crystal. However, it may in theory be possible that cooling to even lower temperatures could even further increase the THz generation efficiency. The output at intermediate temperatures was measured under the same experimental conditions to attempt to answer this question.

Theoretically since the absorption coefficient continues to slightly decrease as temperatures decreases below 100 K, the output should also continue to increase. Still, this effect should be very small and the increase in efficiency would be similarly modest. Figure 4.9(b) and Figure 4.10(b) show slightly conflicting results, but specifically in the 20 mm long crystal there was no noticeable increase in THz output from 120 K to 81 K strongly indicating that cooling to temperatures below 80 K is not advantageous.

What is also shown in the shape of the delay curves in Figure 4.9(a) and Figure 4.10(a) is that during cooling the centroid of the curves shifts toward a larger delay. Although this is not a strong result, it corroborates the result from [73, 76] that as the crystals are cooled the output frequency increases due to the changing THz refractive index (and therefore phase

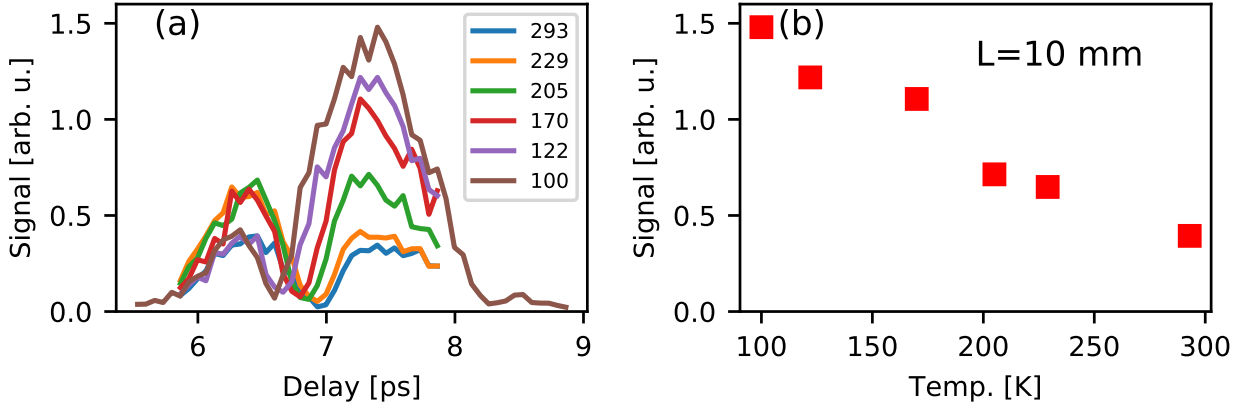


Figure 4.9: Delay scans (a) and maximum output (b) during cooling of a 10 mm long 212 μm poling period PPLN.

matching condition). The two-peaked nature of the delay behavior also likely adds to the slight difference in behavior during cooling for the crystals of two different lengths. The nuanced explanation of this, related to the complex field produced by the combination of third-order phase and the pulse-train produced by the HR/PR combination, will be outlined in the next chapter.

4.3.3 Evidence of cascading in IR spectrum

The transfer of energy between the optical and THz fields necessarily results in a modification of the optical spectrum, providing another means of diagnosing the nonlinear process. For instance, conservation of energy dictates that the centroid shift of the optical spectrum represents an upper limit to the conversion efficiency (referred to in this work as the "intrinsic efficiency"). In addition, for efficient Terahertz generation an energy transfer process known as cascading is required to circumvent the Manley-Rowe limit [129]. During cascading, optical photons take part in the nonlinear frequency conversion process multiple times, producing effectively multiple THz photons for each optical one. This process can result in both red- and blue-shifting of these photons by multiple times the frequency of the THz photons. These effects are illustrated in Figure 4.11. The transmitted optical spectrum shows an overall red-shift of the centroid from 798.1 nm before the interaction to 801.4 nm after the interaction,

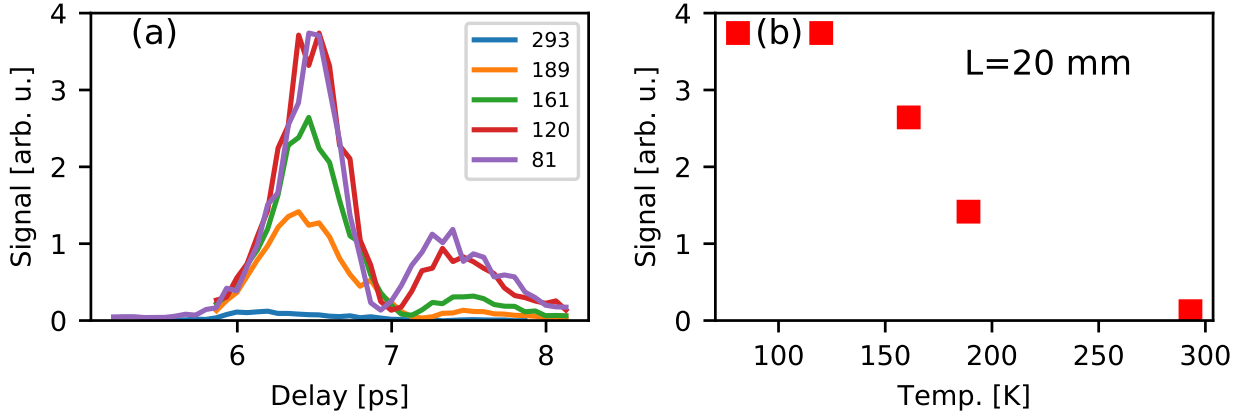


Figure 4.10: Delay scans (a) and maximum output (b) during cooling of a 20 mm long $212 \mu\text{m}$ poling period PPLN.

corresponding to an energy loss of 0.41%, which is also the intrinsic efficiency. Note that in this case the intrinsic efficiency of 0.41 % is 3.2 times larger than the internal efficiency measured directly, signifying the still non-zero absorption at 80 K. The difference spectrum, depicted by the grey shaded area in Figure 4.11, also shows evidence of the cascading process since the red- and blue-shifts are separated from the original peak by an energy larger than the THz photon energy.

The proof-of-principle results demonstrated here can be improved upon in several ways. Of particular importance is implementation of an AR coating to reduce the $\sim 44\%$ loss to the extracted THz energy from Fresnel reflections at the crystal exit face. In addition, the small amount nonlinear chirp imparted to the optical beam by the ANGUS stretcher is estimated to induce a frequency difference, $\Delta\omega$, that varies over the spectrum of the two chirped pulses such that only a portion of the pump pulses are phase matched to the THz frequency Ω . Compensating for the higher order dispersion in the pump pulse, a significantly increased conversion efficiency is estimated, hopefully approaching the 1 % level for a $212 \mu\text{m}$ -poled PPLN crystal of the ideal length. Finally, by increasing the crystal aperture sizes to the maximum that is currently possible [130], it may be possible to increase pump energies to the Joule level and take full advantage of the capabilities of current Ti:Sapphire laser systems. These details will be further explored in the following chapters, but the results presented so far show that

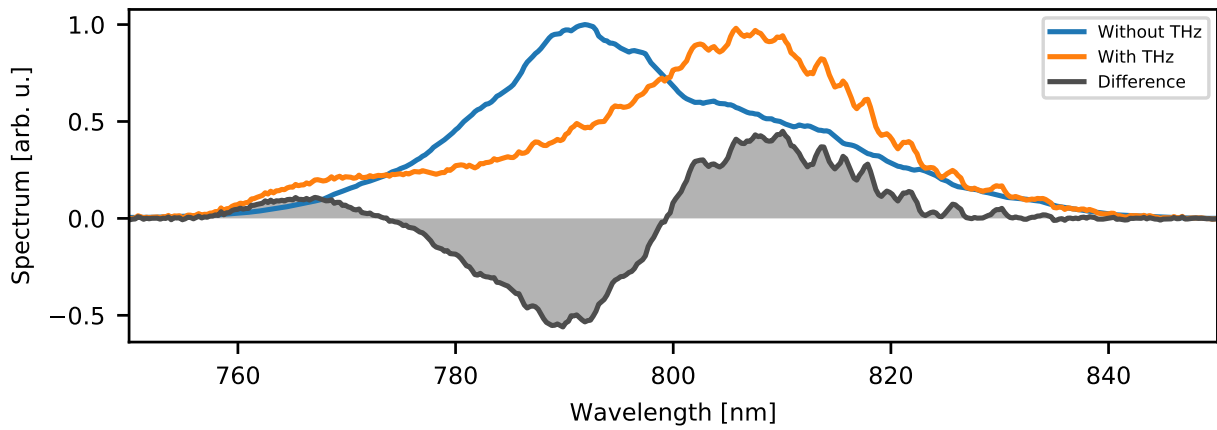


Figure 4.11: Pump spectra before (blue) and after interaction with the 212 μm PPLN (orange). The shaded graph demonstrates an energy transfer due to THz generation. For this measurement the crystal was cooled to 82 K and operated with a pump fluence of $F = 0.287 \text{ J}/\text{cm}^2$.

chirp-and-delay pumping of PPLN is a promising scheme for generating narrowband THz pulses at the mJ level required by future applications.

Chapter 5

The effect of third order dispersion on narrowband terahertz generation via trains of chirped pulses

K. Ravi should be recognized for his initial sharing of a script to calculate the analytic output for pulses without TOD, which was used as a jumping off point for many of the calculations in this chapter. The results presented in this chapter are being prepared for submission in a peer-reviewed journal.

The previous chapter showed that the method of chirp-and-delay can be used to produce high-energy THz pulses, especially using a broadband Ti:Sapphire based system to generate THz in the 0.5 THz frequency range using quasi-phase-matching (QPM) in periodically-poled lithium niobate (PPLN) [85].

However, there were known complexities in those results which implied that the complete process was not understood. First and foremost, the efficiency of the process measured to be in the 0.1% range was not as high as in ideal theoretical predictions [34], showing in the 1% range. The THz output as a function of delay was peaked as expected, but also showed complex features (seen in Fig. 4.4(a)) that were not at the time explained. Additionally, there were nuances that led us to believe that the full pump pulse was not taking part in the process; specifically that the modification of the pump spectrum at high fluence did not occur in the entire pump spectrum, but only the central portion (seen in Fig. 4.11).

This chapter outlines how principally the higher order spectral phase on the NIR pump - but also the complex train of pulses from the experimental setup - contribute to these nuances and the decreased efficiency compared to the ideal prediction. The exact effect of the higher-order phase will be derived, but the concept can already be visualized using the Wigner-style plots common in the field of DFG. The simple plot, seen in Figure 4.1 first and again in Figure 5.1 now shows the general effect of TOD on the process, where now less of the energy

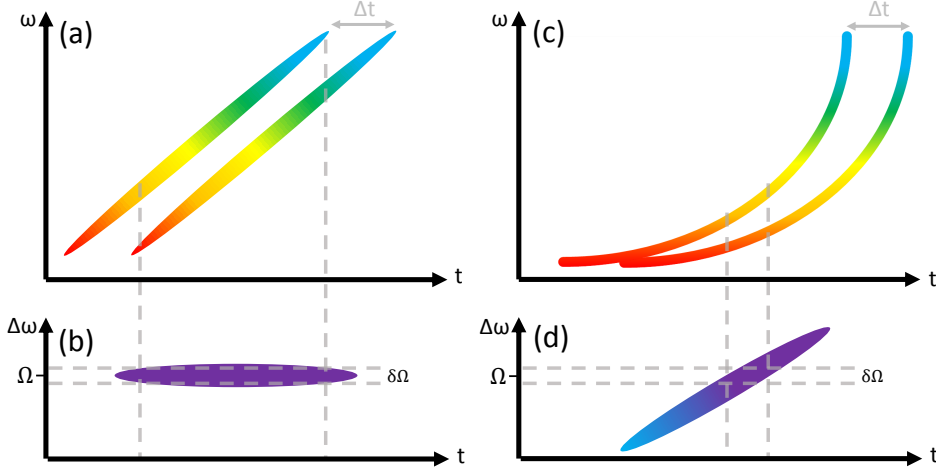


Figure 5.1: Chirp and delay concept including now the general effect of higher order phase. (a) and (b) are the separate overlapped NIR pulses without any TOD and the resulting difference frequency. (c) and (d) are the same now with TOD (not to scale) showing that less of the overall difference frequency content is within the THz bandwidth $\delta\Omega$.

of the pump pulses is within the quasi-phase-matching bandwidth. The effect of the TOD on difference frequency generation in general with standard phase matching will also be discussed, along with implications on the temporal properties of generated THz.

5.1 Properties of phase matching with chirped-and-delayed pulses

The general description of THz generation, first via quasi-phase-matching of chirped and delayed pulses, is as follows, derived from QPM equations in the spectral domain including absorption and the approximation of a reduced $\chi_2^{\text{eff}} = 2\chi_2/\pi$, and ignoring group velocity dispersion [34]

$$A_{\text{THz}}(\Omega, z) = \mathcal{F}_{t \rightarrow \omega} [|A_{\text{opt}}(t)|^2] \frac{i\Omega\chi_2^{\text{eff}} [e^{i\Delta kz} - e^{-\alpha(\Omega)z/2}]}{n(\Omega)c (\alpha(\Omega) + 2i\Delta k)} \quad (5.1)$$

$$\Delta k = \frac{\Omega(n(\Omega) - n_g(\omega_0))}{c} - \frac{2\pi}{\Lambda}, \quad (5.2)$$

where A_{opt} is the combined optical field of the input chirped pulse-train, with single pulses centered at ω_0 . Ω is the phase matched THz angular frequency, and χ_2^{eff} and α are the

second-order nonlinearity and absorption coefficient of the medium. $\Delta k = 0$ is the condition for perfect phase matching, where Λ is the poling period of the nonlinear medium, and n and n_g are respectively the standard and group refractive indices within the medium. A_{THz} is the generated THz field amplitude. If there is no quasi-phase-matching then the term with Λ is removed and the χ_2 is no longer reduced.

The optical field must contain frequency content at the phase matched frequency in the medium, which is contained within the analytic expression. The frequency content term and the phase matching term are both peaked in amplitude, so if they do not peak at the same THz frequency then the THz field will be low. This is especially true when the phase matching is narrow-band, which is the case as the length of the quasi-phase-matching medium increases [124]. Because of this, the 'difference frequency content' will be an important concept in this chapter that essentially determines the suitability of the combined input NIR pump pulses for producing THz at a given frequency. Because the output THz energy is proportional to $|A_{\text{THz}}|^2$, the relevant optical property for THz energy is $|\mathcal{F}_{t \rightarrow \omega} [|A_{\text{opt}}(t)|^2]|^2$, which will be referred to as the 'difference frequency content' of the pump pulse-train henceforth.

An important additional condition not reflected directly in the equations here, but only indirectly within the difference frequency content, is that the optical pump pulses must have significant bandwidth in order to have enough total overlap at the optimum delay. Since the optimum temporal spacing Δt_{opt} between optical pulses is fixed by the chirp rate ($1/\phi_2$) and phase matched THz frequency Ω ($\Delta t_{\text{opt}} = \Omega\phi_2$), and the chirped NIR pulse duration is fixed by the chirp rate and optical bandwidth $\delta\omega_L$ ($\tau_L = \delta\omega_L\phi_2$) there is a lower limit on the optical bandwidth for efficient DFG. For significant temporal overlap $\tau_L \gg \Delta t_{\text{opt}}$ must be satisfied and therefore $\delta\omega_L \gg \Omega$ is a condition for the optical bandwidth.

What is also important, in addition to the difference frequency content, is of course the nonlinear material properties and how they depend on frequency. This is reflected within the phase matching term in equation 5.2, that is, the part of the equation that is not the difference frequency content of the pump pulses. The THz energy is proportional to $n(\Omega)|A_{\text{THz}}|^2$, so the relevant term that depends only on material parameters ($n(\Omega), \alpha(\Omega), L$) assuming $\Delta k = 0$ is:

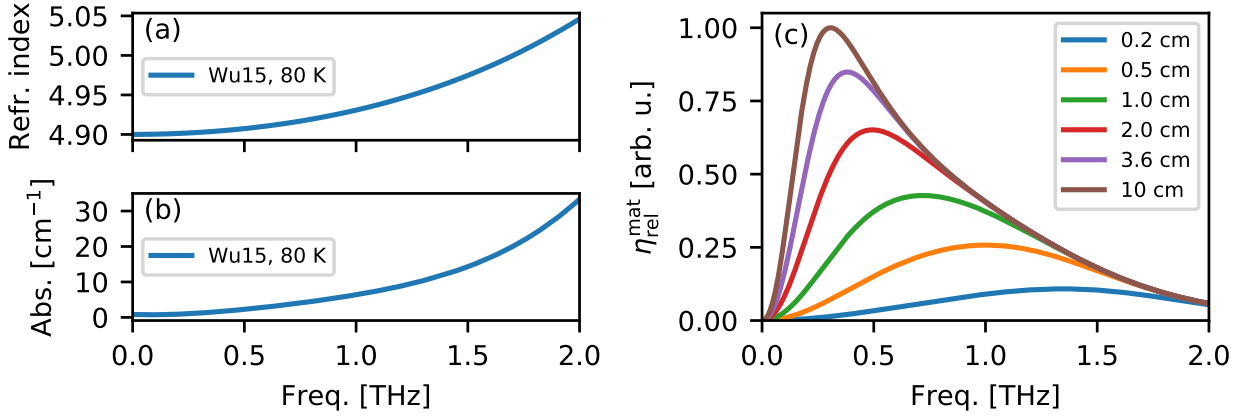


Figure 5.2: The THz refractive index of PPLN (a), and the absorption coefficient (b), both at 80 K with data from [126]. This data alone can inform the relative efficiency due only to the material properties, which is shown for different lengths in (c) with an arbitrary vertical scale.

$$\eta_{\text{rel}}^{\text{mat}} \propto n(\Omega) \left| \frac{\Omega}{n(\Omega)} \frac{[1 - e^{-\alpha(\Omega)L/2}]}{\alpha(\Omega)} \right|^2. \quad (5.3)$$

This can be thought of as the relative efficiency due only to material properties, $\eta_{\text{rel}}^{\text{mat}}$. This is only valid of course when $\Delta k = 0$, which is relevant when the quasi-phase-matching bandwidth is narrow. For all of the results reported in this work from long PPLN crystals, above 5 mm and up to 36 mm in length, the bandwidth is below 10 % and as low as 1 % [124]. Because the experimental work in this thesis and this chapter all deals with PPLN, the example of this concept is shown using PPLN material properties measured in [126] in Figure 5.2, although the concept is general for narrowband phase matching.

The relative efficiency, which is directly proportional to THz output energy assuming an ideal pump input at a every frequency, shows that the interplay between increasing frequency and increasing absorption results in a maximum for any given length. The location of this maximum decreases in frequency as the length of the crystal is increased, due to the quickly increasing absorption in PPLN with increasing frequency above 1 THz. The example of PPLN in Figure 5.2 shows clearly that for any length, but especially cm-scale lengths needed for the output THz to grow, the best is the 0.5 THz range.

There are other nonlinear materials that are useful for THz generation, for example gallium phosphide (GaP), which does not have a large absorption peak until roughly 11 THz [131] and has been used in QPM schemes [132]. Zinc telluride (ZnTe) is also used as a very common material for detecting THz [133, 134], and has also been used to generate THz. However, in addition to the known absorption peak at 5.32 THz [135] there are also minor peaks at 1.6 THz and 3.7 THz [136]. These absorption peaks are very important for the generation of broadband THz radiation (in addition to of course the ability to phase match across that bandwidth [131]), but also inform what range of frequencies are ideal for phase matching narrowband THz.

If one considers the situation now with direct phase matching, where the medium is no longer periodically poled and therefore does not set a limited phase matching bandwidth, then the relative efficiency no longer relies on $\Delta k = 0$. The relative efficiency is still proportional to $n(\Omega)|A_{\text{THz}}|^2$, but includes non-perfect phase matching and the phase matching term is now different:

$$\eta_{\text{rel}}^{\text{mat}} \propto n(\Omega) \left| \frac{\Omega}{n(\Omega)} \frac{[e^{i\Delta k L} - e^{-\alpha(\Omega)L/2}]}{(\alpha(\Omega) + 2i\Delta k)} \right|^2 \quad (5.4)$$

$$\Delta k = \frac{\Omega(n(\Omega) - n_{\text{g}}(\omega_0))}{c}. \quad (5.5)$$

Therefore the output THz for a given frequency at a given length depends strongly on the phase matching and there are minima at frequencies where the absorption is not necessarily high. Using GaP as an example, and using IR properties from [137] and THz properties from [131] shown in Figure 5.3(a–c), the relative efficiency of the direct phase matched process is shown in Figure 5.3(d). The IR group refractive index is 3.62 at 800 nm pump wavelength [137]. Note now that the relevant lengths are now sub-mm due to the short coherence length at these frequencies.

This shows that there are regions between the phase matching dips of approximately 0–3 THz, 3–6 THz, and 6–8 THz (depending on the length) where narrowband terahertz could have a high output. There is also the same interplay between frequency and absorption overlaying the effect of phase matching, which results in the region with the highest output being between

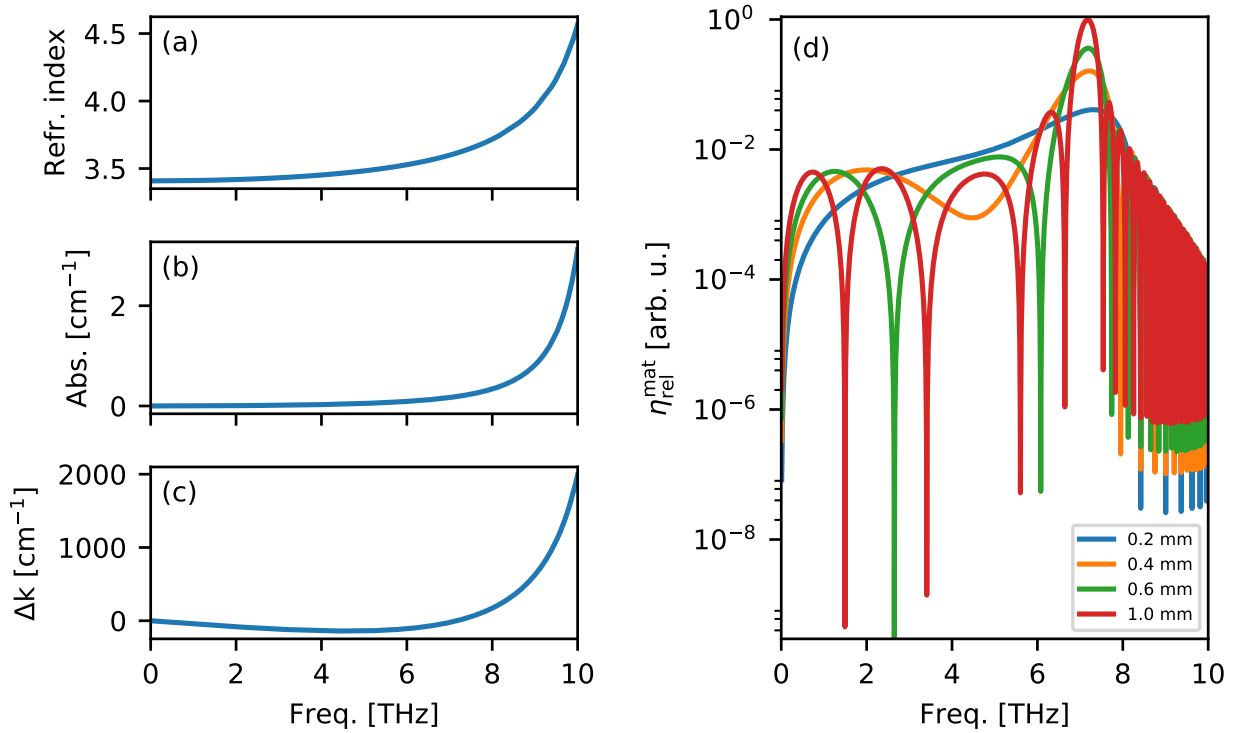


Figure 5.3: The THz refractive index of GaP **(a)**, the absorption coefficient **(b)**, and phase mismatch Δk **(c)** at room temperature using data from [131, 137]. This data alone can inform the relative efficiency due only to the material properties, which is shown for different lengths in **(d)** normalized to the maximum at 1 mm length. Now since there is only direct phase matching the phase mismatch at certain frequencies causes steep minima depending on the length.

6–8 THz depending on the length. In this region the output increases reliably in magnitude with the length, while also decreasing in width, due also to the fact that there is perfect phase matching at 7.17 THz when pumped at 800 nm.

Still, the PPLN material properties are the most relevant to this work, and importantly also for producing high energy THz radiation in general due to the higher nonlinear coefficient.

The equations in this section as well as the concept of the optical difference frequency content, and the behavior of the THz output only due to material properties are very important to understanding scaling of THz generation via chirp-and-delay. These equations however do not include effects on the spectrum of the NIR pulse-train as THz is generated, which is present in interactions at high efficiency due to cascading of the nonlinear process [129, 76, 85]. This means that quantitative results only apply at low efficiencies, but can also inform the process in general.

5.2 Temporal phase description of IR pump pulses

The use of the stretched ANGUS pulses in the experiments that will be referenced in this chapter — without any significant modifications to the temporal properties — fixes those temporal properties as exactly the same that exist within the power amplifiers of the laser system. Because the properties of the grating stretcher that produces this stretched pulse are quite well known, so are the spectral phase in second-order ϕ_2 and third order ϕ_3

$$A_{opt}(\omega) \propto \exp \left[-i \left(\phi_0 + \phi_1(\omega - \omega_0) + \frac{\phi_2}{2}(\omega - \omega_0)^2 + \frac{\phi_3}{6}(\omega - \omega_0)^3 + \dots \right) \right]. \quad (5.6)$$

It will be assumed that knowledge of higher orders is not necessary. The spectral phase produced in a grating stretcher are well-known and shown in section 2.1.1, but in general a stretched and therefore chirped pulse may be produced from a variety of methods. In any case, all of these methods also introduce higher order spectral phase. It is possible to produce the temporal envelope and phase of the pulse by using two Fourier transform algorithms. However, this method is not quite satisfactory since it does not clearly inform the exact shape of the temporal phase in a large parameter range and requires a very large number of points when

a pulse is stretched significantly (and therefore becomes computationally complex and time intensive).

McMullen et al, 1977 [29] derives an exact representation for the complex temporal electric field of a pulse with arbitrary second order (GDD= ϕ_2) and third order (TOD= ϕ_3) spectral phase. This was done in the context of predicting pulse profiles for compressed pulses traveling through media, but is crucial for understanding the difference frequency created using the chirp-and-delay method for stretched pulses with TOD. The exact temporal optical field is as follows:

$$E(t) = Re \left\{ 2E_0 \sqrt{\frac{2\pi \ln(2)}{\delta\omega_L^2}} \exp[-i\omega_0 t] \exp \left[\frac{2a}{\phi_3} \left(\frac{4a^2}{3\phi_3} - t \right) \right] Ai \left[\left(\frac{2}{\phi_3} \right)^{1/3} \left(\frac{2a^2}{\phi_3} - t \right) \right] \right\} \quad (5.7)$$

$$a = \frac{2 \ln(2)}{\delta\omega_L^2} - i \frac{\phi_2}{2}, \quad (5.8)$$

with $\delta\omega_L$ as the FWHM spectral width of the intensity, ω_0 the central frequency, ϕ_2 the GDD, ϕ_3 the TOD, $Ai[]$ the Airy function, and a just a constant for bookkeeping. This is following the style of the reference for simplicity.

Two assumptions are necessary to simplify this representation and to approximate the Airy function with simpler functions. The first is $\phi_2 \gg (4 \ln(2)/\delta\omega_L)^2$ (or $\phi_2 \gg \tau_0^2$), which means that the pulse is significantly stretched. In this case the stretched pulse duration can be approximated as $\tau_L = \delta\omega_L \phi_2$ and a reduced to $a = -i \frac{\phi_2}{2}$. The second necessary assumption requires the magnitude of the argument in the Airy function to be very large. Rewriting the argument of the Airy function using the simplification for a results in

$$\left| \frac{\phi_2^2}{2\phi_3} \left(\frac{2}{\phi_3} \right)^{1/3} \left(1 - \frac{2t\phi_3}{\phi_2^2} \right) \right| \gg 1, \quad (5.9)$$

which can then lead to a simplification based on the asymptotic behavior of the function as the argument is large in magnitude. The appendix of [29] has more detail about both the asymptotic approximation, which reduces the Airy function, and an additional Taylor expansion to further simplify the result. Both rely on ϕ_3 being small. However, this is quite an abnormal inequality since it has the variable t within it.

Replacing t in the inequality with the stretched pulse duration $\tau_L = \delta\omega_L\phi_2$ and assuming that both the outer factor is large and the additional factor to unity in parenthesis is small results in

$$|\phi_3| \ll \left| \phi_2^{3/2} \right| \quad (5.10)$$

$$|\phi_3| \ll \left| \frac{\phi_2}{\delta\omega_L} \right|, \quad (5.11)$$

removing all small numerical factors. The first is a restriction on the magnitude of TOD overall, which corresponds to the local curvature of the phase, and the second is a restriction on the magnitude of the phase difference across the entire bandwidth of the pulse. Note that the values for ANGUS of $\phi_2 = 2.3 \text{ ps}^2$, $\phi_3 = -0.0044 \text{ ps}^3$, and $\delta\omega_L \approx 15 \text{ THz}$ satisfy these two inequalities ($0.0044 \ll 3.5$ and 0.15 respectively). The final resulting field with all approximations is

$$E(t) = \text{Re} \left\{ E_0 \sqrt{\frac{\tau_0}{\tau_L}} \left(1 - \frac{\phi_3 t}{\phi_2^2} \right) \exp \left[\frac{-2 \ln(2) t^2}{\tau_L^2} \right] \exp \left[-i \left(\omega_0 t + \frac{t^2}{2\phi_2} + \frac{-\phi_3 t^3}{6\phi_2^3} \right) \right] \right\}, \quad (5.12)$$

ignoring constant phase offsets and using $\tau_0 = 4 \ln(2)/\delta\omega_L$ and τ_L to keep it more compact. This is a Gaussian pulse of duration τ_L with a negligible change in envelope, and a significant additional temporal phase. This temporal phase comes directly from the spectral phase parameters. One can write then the instantaneous frequency $\omega(t) = -d(\text{phase})/dt$ as:

$$\omega(t) = \omega_0 + \frac{1}{\phi_2} t + \frac{-\phi_3}{2\phi_2^3} t^2. \quad (5.13)$$

Now it can be seen that the linear chirp comes only from the GDD as is the case also with zero TOD, and the quadratic chirp comes from the TOD, scaled by the GDD to the third power. This is significant since one can now write the instantaneous frequency analytically, and it is clear that the quadratic term does not depend only on the TOD. A similar analysis is shown from a different perspective in [138] and also related to Terahertz generation in [139].

5.3 Effect of the TOD and pulse-train on input IR field

The previous section showed that with certain assumptions on the magnitude of the spectral phase orders, a stretched pulse with third-order can be approximated as a Gaussian with only a significantly different temporal phase. Now the factor that impacts DFG and THz generation is the effect that this significantly different temporal phase has on the available difference frequency content. This approach will take into account a driving pump pulse-train that is either many pulses as produced in an etalon as was used in [85], or simply two pulses of equal amplitude, always with a constant time delay between successive pulses. The spectral phase values used here will always be those of the ANGUS pulses, i.e. GDD of 2.3 ps^2 and TOD of -0.0044 ps^3 .

When creating such a train of pulse a partial-reflector (PR, $R=38\%$) and a high-reflector (HR) are used, which is essentially an etalon, there is a theoretically infinite train of pulses with the energies $E_1 = R, E_n = R^{n-2}(1 - R)^2$, with the first two pulses having approximately equal energy. Then the total optical field can be written as a sum of this pulse train:

$$A_{\text{opt}}(t) = \sum_{n=1}^{\infty} E_n A_n(t - (n - 1)\Delta t) \quad (5.14)$$

$$A_n(t) \propto \exp\left[\frac{-2 \ln(2)t^2}{(\delta\omega\phi_2)^2}\right] \exp\left[-i\left(\omega_0 t + \frac{t^2}{2\phi_2} + \frac{-\phi_3 t^3}{6\phi_2^3}\right)\right]. \quad (5.15)$$

This produces a much different picture of the input IR energy than analysis using only GDD, or only a pair of pulses. Because there is TOD, i.e. a curved frequency across the pulses, and in the case of the infinite pulse train many pulses overlapping, there is now complex temporal interference which includes even an effect on the overall envelope of the IR energy.

The significance of this can be seen in the changes on the field of the delayed and overlapped pulses $|A_{\text{opt}}(t)|^2$, and on the difference frequency content available for producing THz defined as $|\mathcal{F}_{t \rightarrow \omega} [|A_{\text{opt}}(t)|^2]|^2$. These changes are summarized in Figure 5.4 at one temporal delay of 5.78 ps , in order to produce 400 GHz radiation with the assumed GDD of 2.3 ps^2 . The shown examples are two isolated pulses without and with TOD, and a train of 10 pulses as from the described PR/HR combination also without and with TOD.

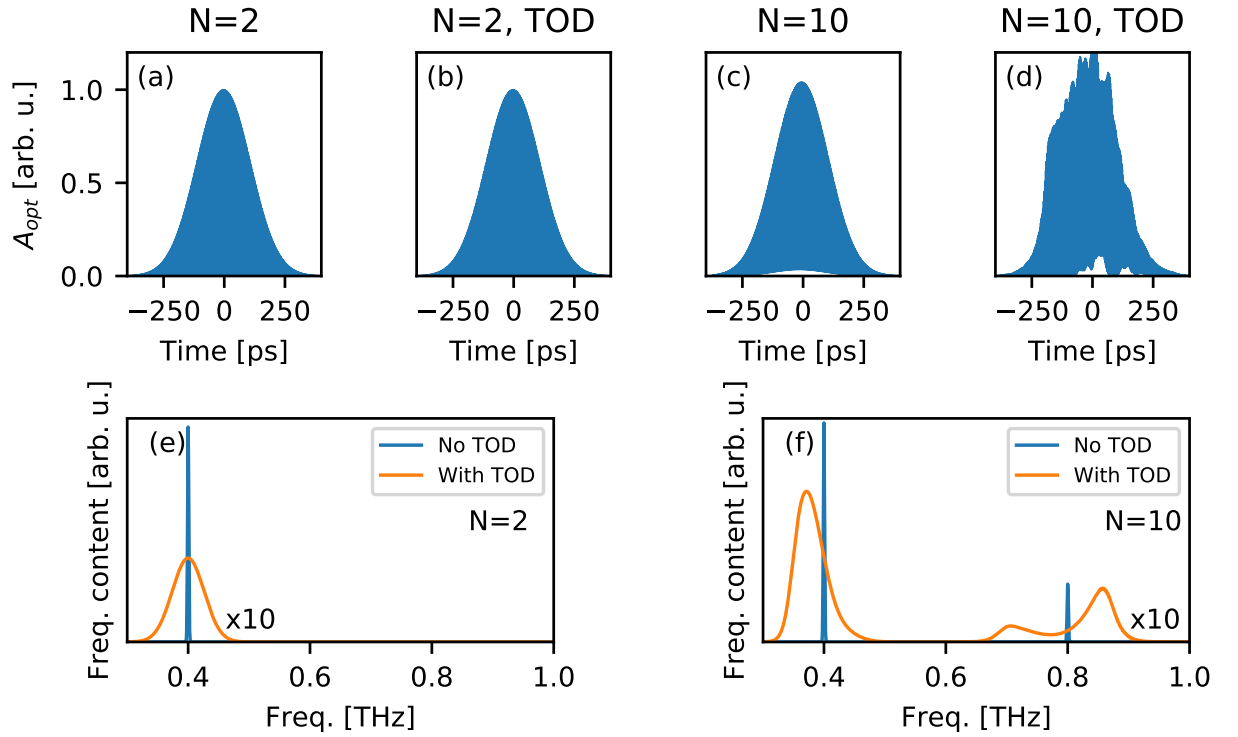


Figure 5.4: Comparison of the total pulse train envelope (**a–d**) and frequency content (**e–f**) at one time delay of 5.78 ps producing frequency content centered on 400 GHz with permutations of no TOD (blue) and a TOD of -0.0044 ps^3 (orange), 2 pulses and a pulse train ($N=10$). Not visible within the field amplitude in (**a–d**) is the temporal interference, producing amplitude variations with a frequency corresponding to the difference frequency shown in (**e–f**).

In these cases the envelope of the overlapped pulses is largely unchanged when there is no TOD or no pulse train (Fig. 5.4(a–c)), except with both TOD and the longer pulse-train (Fig. 5.4(d)). In that last case the envelope becomes significantly more complex, and also has a larger peak field due to the more complex temporal interference. Although these effects on the envelope are somewhat instructive, it is only the difference frequency content that has a direct consequence on the DFG process.

The difference frequency content is sharply peaked when the TOD is zero (Fig. 5.4(e)) regardless of the number of pulses, which is equivalent to saying that across the envelope the instantaneous difference frequency does not vary significantly. In the case with zero TOD and a train of ten pulses, there are higher harmonics present in the frequency content. This is because in this case there is still significant overlap between the first and third pulse, or second and fourth, etc. including many pulses in the pulse train and therefore also many harmonics (only the first higher frequency peak is shown). Because the overlap is less and the energy in the $N > 3$ pulses is significantly lower than the first and second, the frequency content in these harmonics is also usually much lower than that in the principal.

When the TOD of -0.0044 ps^3 is included however (Fig. 5.4(f)), the difference frequency content is no longer as sharply peaked. With only two pulses the peak of the frequency content is more than an order of magnitude lower and wider than the case without TOD. This is a consequence of the difference frequency varying across the pulse significantly. In the case with a longer train of ten pulses and also finite TOD, the frequency content gets similarly more complex as did the envelope. This is due to the complex temporal interference between all number of pulses.

It is instructive to another level to view this increased complexity in the difference frequency content at various temporal delays (equivalently different generated THz frequencies). Figure 5.5 shows the same permutations of number of pulses and TOD at an additional three temporal delays (2.89, 8.67, and 11.56 ps) that would produce 200, 600, and 800 GHz radiation respectively.

The broadening and decrease of the frequency content is present in all cases. However, the complexity of the difference frequency content increases with the temporal delay (and

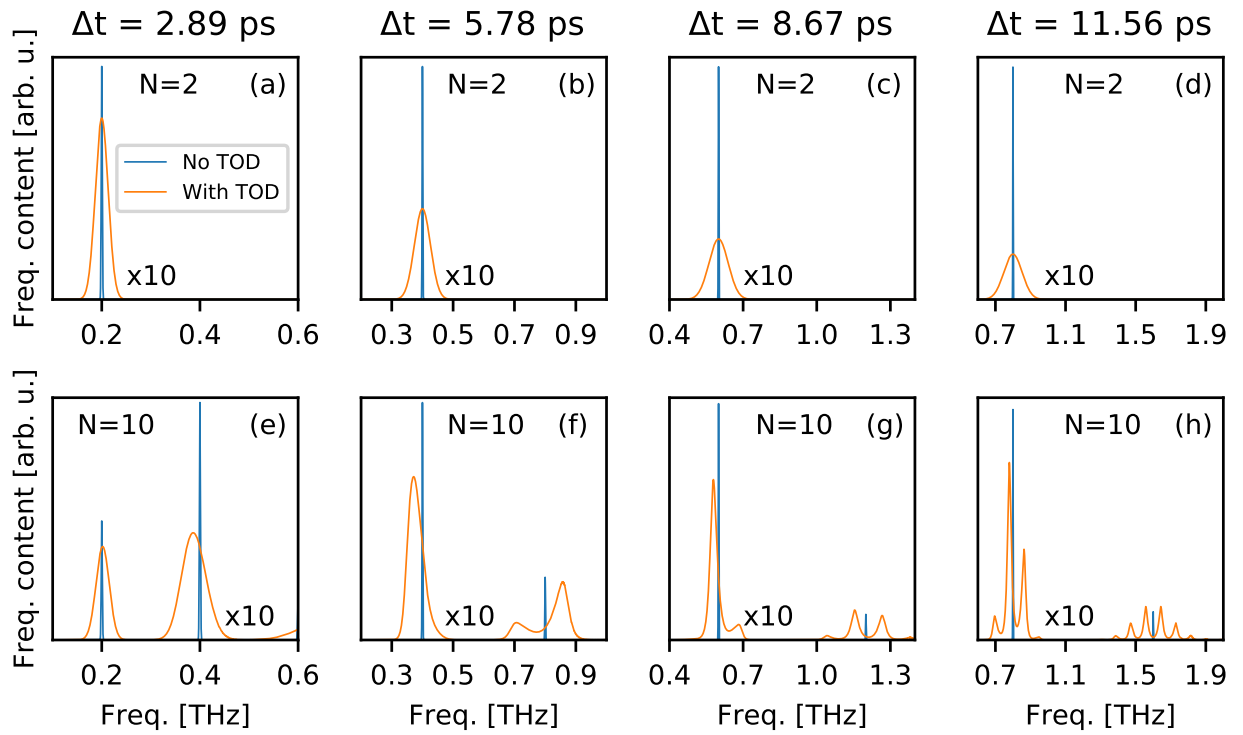


Figure 5.5: Comparison of the total pulse train difference frequency content with permutations of no TOD (blue) and a TOD of -0.0044 ps^3 (orange), 2 pulses (a–d) and a pulse train ($N=10$) (e–h), at the four different delays $\Delta t=2.89, 5.78, 8.67, 11.56$ ps necessary to produce frequency content centered on 200, 400, 600, and 800 GHz respectively. (b) and (f) are a duplication of Figure 5.4(e–f).

therefore generated THz frequency when passed through the nonlinear medium). This is a result of the increase in the space between overlapping frequency components as the temporal delay increases. As there is a larger time between each pulse in the train, at any given point in time there are frequencies overlapping that produce a difference frequency more different than the central difference frequency, but at that point in time the difference in frequency between the different pulses in the train is larger.

The result of this analysis is that the presence of TOD on the chirped pulses used to create a pulse-train will decrease the peak available frequency content for the DFG process. If the produced pulse-train is more complex than just two pulses of the same energy then increased complexity occurs as well. The following sections will show some experimental nuances resulting from these physics, verifying the conclusion, along with some supporting theoretical explanations.

5.4 Signature of TOD in experimental data

The presence of TOD has a significant effect on the DFG process via its impact on the available difference frequency content, as shown in the previous sections. In the following sections experimental results verify this, and some of the nuances of this effect are expanded upon. Past experiments using an infinite train of broadband chirped pulses in PPLN [85] showed the viability to produce high-energy (tens of μJ) THz pulses in the 0.5 THz range at a relatively high efficiency (0.13%). Along with these results the work also showed the expected dependence of the optimum temporal delay and output THz frequency on the parameters of the PPLN, and the increase in efficiency when the crystal is cooled to cryogenic temperatures (reducing the THz absorption).

The experimental apparatus used for these past results and the results presented here is reproduced in Figure 5.6. The driver laser is the Ti:Sapphire-based ANGUS laser system, with relevant temporal properties the same as those already used in the previous section: $\phi_2=2.3\text{ ps}^2$, $\phi_3=-0.0044\text{ ps}^3$. The pulse-train is created with a PR/HR combination to produce two equal pulses and a train of lower energy pulses, with the spacing between each subsequent pulse a constant Δt . The beam is resized to fit approximately the aperture of a given crystal using

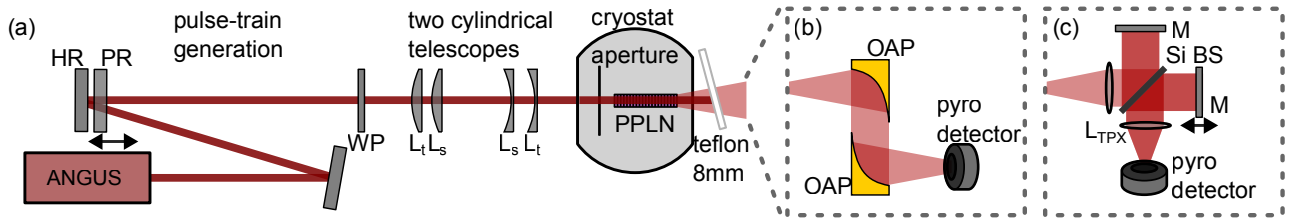


Figure 5.6: Chirp-and-delay experimental setup, reproduced from the previous chapter. This HR-PR combination produces a train of pulses rather than two pulses of equal energy.

cylindrical lenses, and the THz is collected using a pair of off-axis parabolic mirrors (OAPs) on to a pyroelectric detector (Gentec-EO: THZ9B-BL-BNC). In the case of the crystal with $330\ \mu\text{m}$ poling period there are no lenses used to demagnify the pump beam, and a single TPX lens is used to focus the THz beam onto the pyroelectric detector. A longitudinal interferometer was used to measure the center frequency in the case of the two crystals with the highest THz output. The output IR energy is dumped on a sheet of Teflon, and the spectrum of that scattered output is measured with a combination of a diffuser and a fiber spectrometer. The input IR spectrum is recorded automatically with the laser controls system. The crystal is contained within a small vacuum chamber to allow for cryogenic cooling to roughly 80 K.

Results from the previous work [85] will now be revisited with the TOD analysis in mind, and effects will be elucidated using additional complementary measurements not yet shown.

5.4.1 Output pump spectrum

The measured output pump spectrum shows significant red-shifting due to the THz generation process (Fig. 5.7(a-c)), already shown once in the previous chapter (Fig. 4.11). This is due to, in the case of highly efficient generation, the cascading of the DFG process whereby IR photons take part in the frequency down-conversion process multiple times. Equivalently, the pump spectrum must change as the IR photons are shifted many times. This is easy to imagine in the case of a narrow-band pump [84], but in the case of a broadband pump the cascaded IR remains within the original bandwidth. However, it can be seen that especially at low fluence and with shorter crystals, but even still at high fluence, the shifting of the IR spectrum does not take place across the whole spectrum. This 'dip' in the spectrum is a signature of the THz generation process not being phase matched at every point in time across the individual

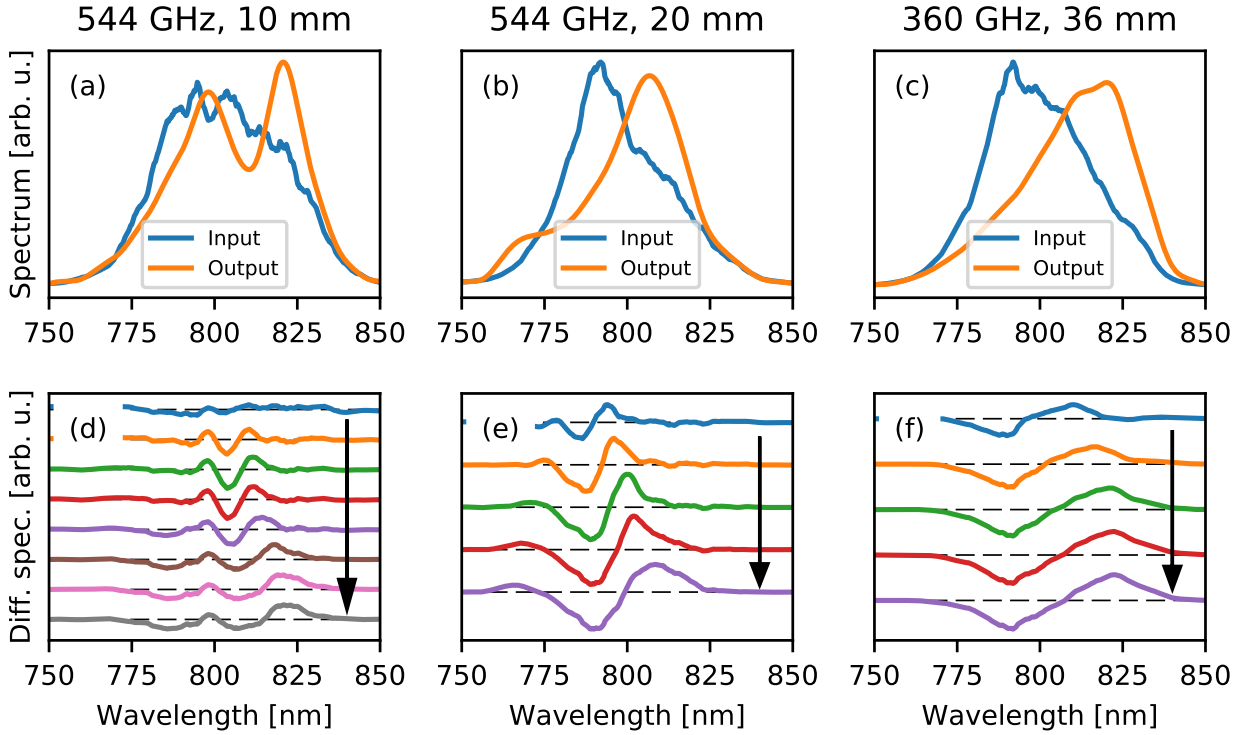


Figure 5.7: Comparison of input and output IR spectrum for three different experimental scenarios of 544 GHz and 5 mm crystal length **(a)**, 544 GHz and 10 mm crystal length **(b)**, and 544 GHz and 36 mm crystal length **(c)** all at 82 K. The difference between the input and the output spectrum at increasing fluence levels is shown **(d–f)** in these varying scenarios with the arrows pointing from lower towards higher pump fluence (with a maximum of ~ 600 , 300, and 200 mJ/cm^2 in **(d–f)** respectively), showing the magnitude of the dip increasing and shifting towards longer wavelengths.

chirped pulses in the pulse train (and therefore also spectrum, since the the chirp of the pulses relates both spectrum and time).

Note that a 'dip' is most clearly visible in the two shorter crystal cases because in shorter crystals there is less THz absorption, so the output spectrum in those shorter crystals better represents the effect of the actual output THz on the pump spectrum. In the case of the longer crystal (Fig. 5.7(c)) the pump spectrum has been affected by more THz that was later absorbed so it is not a dip and rather a complete shift.

It is possible using the simple temporal phase relation already derived to show that the dip is a direct consequence of the TOD. Since one can write the instantaneous frequency

analytically as in equation 5.13, the difference frequency at a delay Δt can also be written when the pulses are assumed to be copies of each other:

$$\Delta\omega(t) = \left[\frac{\Delta t}{\phi_2} + \frac{\phi_3 \Delta t^2}{2(\phi_2)^3} \right] + \left[-\frac{\phi_3 \Delta t}{(\phi_2)^3} \right] t. \quad (5.16)$$

With pulses that are not copies of each other, such as in [81, 82] this relationship becomes much more complex. If the expected THz frequency ν_{THz} is known, then it can be calculated which part of the delayed and overlapped pulses will be beating at that frequency at the time delay Δt . For this analysis only two pulses will be assumed, since they contain the majority of the total pump energy. Fixing the difference frequency to exactly the frequency of the generated THz as follows

$$2\pi\nu_{\text{THz}} = \frac{\Delta t}{\phi_2} + \frac{-\phi_3}{2\phi_2^3} (t_{\text{gen}}^2 - (t_{\text{gen}} - \Delta t)^2) \quad (5.17)$$

fixes as well where the THz at exactly that frequency is being produced within the pump pulses. At a given delay there is a time t_{gen} in the first pulse that is producing THz and a time $(t_{\text{gen}} - \Delta t)$ that is producing THz in the second pulse

$$t_{\text{gen}} = \frac{\Delta t}{2} + \frac{\phi_2^3}{\phi_3} \left[\frac{1}{\phi_2} - \frac{2\pi\nu_{\text{THz}}}{\Delta t} \right]. \quad (5.18)$$

Since the relationship between time and frequency is already known (simply the instantaneous frequency $\omega(t)$) then so can the portion of the *spectrum* responsible for the THz production at different delays in the first and second pulse. Since the first and second pulse have equal energies (again, ignoring in this case lower energy pulses in the pulse-train) then the spectral content producing the THz most efficiently is

$$\omega_{\text{avg}} = \frac{\omega(t_{\text{gen}}) + \omega(t_{\text{gen}} - \Delta t)}{2} = \omega_0 + \frac{\phi_2}{2\phi_3} - \frac{2\pi^2\nu_{\text{THz}}^2\phi_2^3}{\Delta t^2\phi_3} - \frac{\Delta t^2\phi_3}{8\phi_2^3}, \quad (5.19)$$

which is the average frequency in the combined IR pump pulses that is responsible for creating THz. One can then convert to wavelength

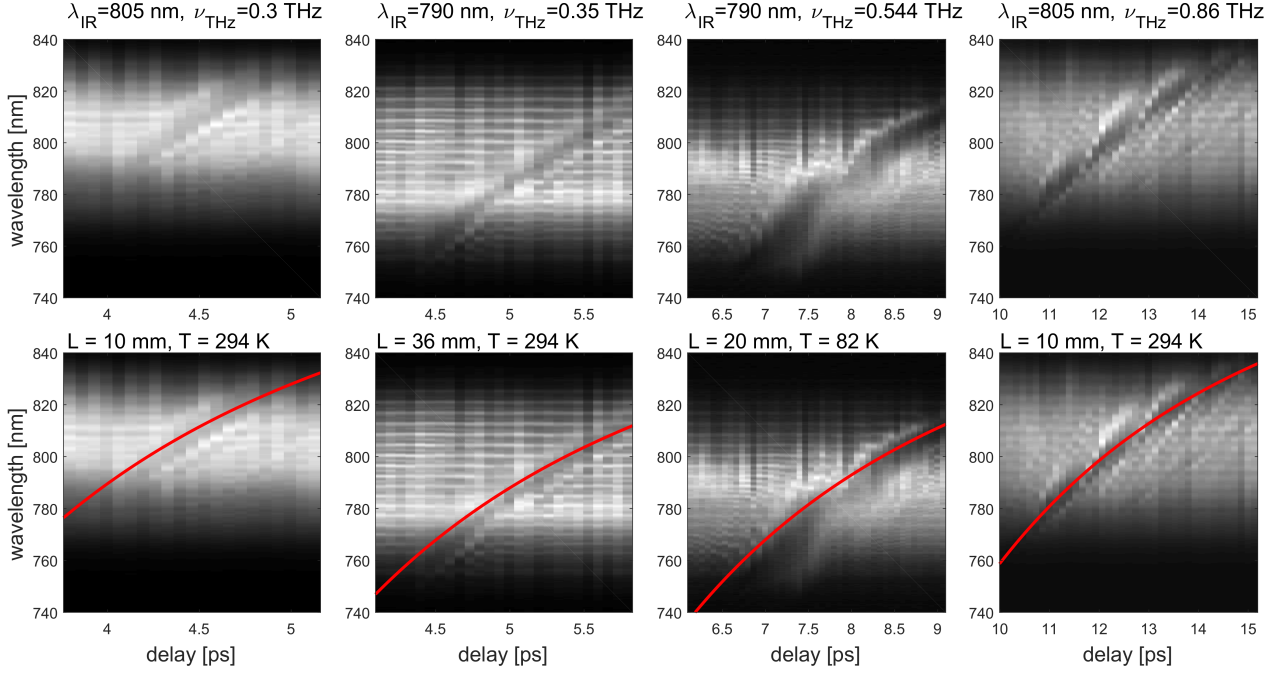


Figure 5.8: Experimental output IR spectrum during a delay scan of a train of IR pulses generating THz in four different poling period PPLN crystals of either 10, 20, or 36 mm length. The upper row and lower row are just duplicates, so that the theory curve is more easily seen. The red line in the lower row is exactly equation 5.20 for each case.

$$\lambda_{\text{avg}} = \frac{2\pi c}{\omega_{\text{avg}}}, \quad (5.20)$$

and compare directly to the measured experimental data. This is shown in the upper row of Figure 5.8. As the temporal delay is changed in four different cases, the spectral location of the 'dip' moves across the pump spectrum. This location in the spectrum fits remarkably well with the λ_{avg} calculated above, shown in the red lines in the lower row of Figure 5.8. This is direct experimental evidence of the non-complete participation of the pump spectrum in the DFG process.

5.4.2 Delay behavior

This section shows the expected behavior of THz output as a function of temporal delay in the PPLN, and shows that the observed complexity can only be predicted when including

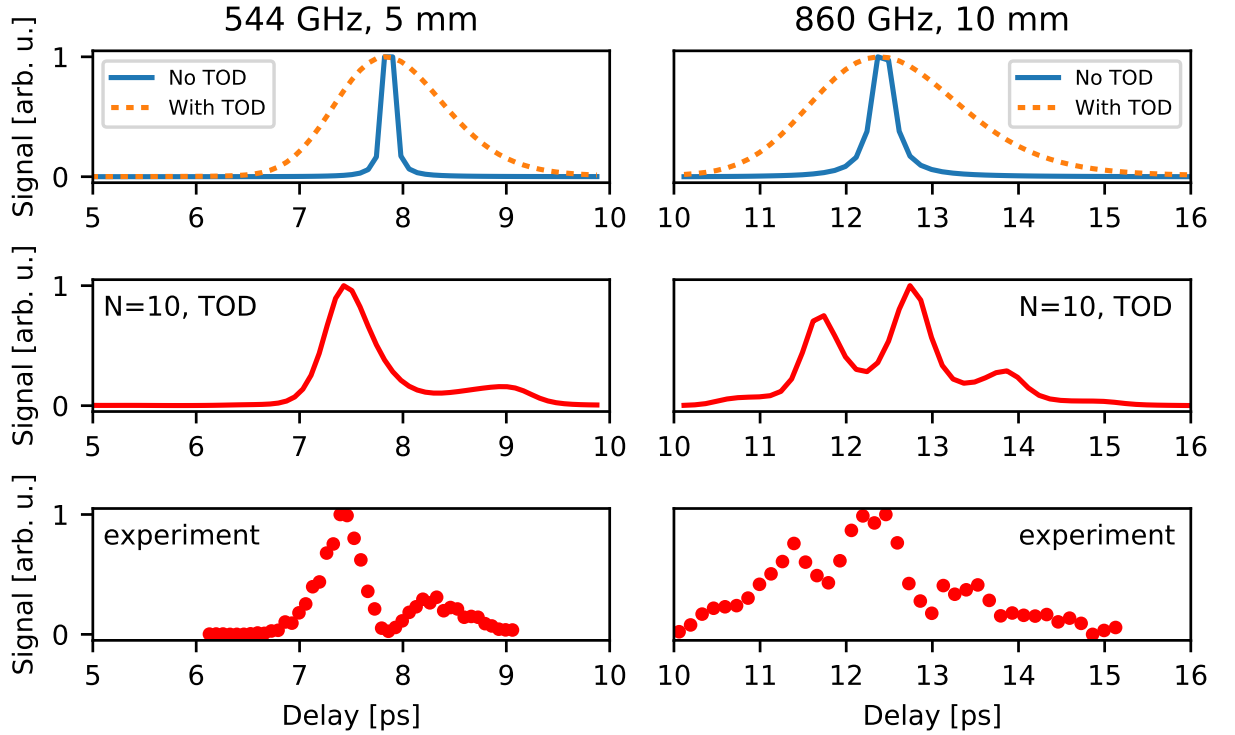


Figure 5.9: Comparison of calculated delay scan behavior, by calculating the expected output of the THz generation process at each time delay with two fixed PPLN crystal properties. Including permutations of no TOD and realistic TOD, 2 pulses and a pulse train. The width of the delay scan increases when TOD is included, but the complexity seen in experiments is only visible when including the whole pulse train.

both TOD and the entire pulse train, confirming another experimental result that is directly caused by the TOD.

The THz output can be calculated according to equation 5.2 using the calculated difference frequency content via an FFT of the optical field to frequency space. The most simple expected behavior is that as the temporal delay sweeps over the predicted optimum ($\Delta t_{\text{opt}} = \phi_2 \Omega$) the THz output peaks. This corresponds to the delay where the largest amount of the difference frequency content is within the QPM bandwidth. This was observed experimentally in [85] and behaved as expected when using crystals of different poling periods producing different frequencies. However, in more than one case the output as a function of delay was not as simple as a single peak.

Using the already shown increase in complexity of the envelope and frequency content, it can be reasoned that the combination of TOD and the entire pulse train can explain this complexity. Figure 5.9 shows the calculated THz (with arbitrary vertical scale) as a function of delay for the two cases with the most complexity (also the two highest frequencies). Similar to the qualitative behavior of the frequency content, the delay behavior is sharply peaked when no TOD is present. When TOD is present, but the calculation is still only with two pulses, the output is lower and spread over a wider range of delays. However, only when both the TOD and pulse train are included in the calculations can the complexity on the delay behavior be reliably reproduced. Although the curves do not exactly match with the FFT+analytic calculation, the agreement is remarkably good qualitatively.

5.5 Effect of TOD on efficiency of THz generation via quasi-phase-matching

It was shown so far that the inclusion of TOD in the DFG process vastly changes the specifics of the interaction between the overlapped pulses in the pulse-train and therefore also the generation of the lower frequency THz radiation. The inclusion of TOD in analyses showed that the THz is only generated from a certain portion of the input pump spectrum, and that when including the entire pulse-train present in experiments, previously uncharacterized features can be explained. However, it is most important for applications requiring very high THz energies that the efficiency of the process remains high and therefore more of the total pump pulse energy can take part in the THz generation.

What was shown in an earlier section is that the peak available difference frequency content decreases when TOD is present. If the THz generation process were infinitely broadband then this would have no effect on total THz energy, but when narrowband THz pulses are being produced within cm-long PPLN crystals, the bandwidth of the process is similarly narrow. Therefore this decrease of the peak frequency content also results in a decrease of the output THz energy.

A simple, limited calculation can be done using just the calculated difference frequency as in equation 5.16, the first-order optimum temporal delay $\Delta t = \Omega\phi_2$, and the NIR pulse

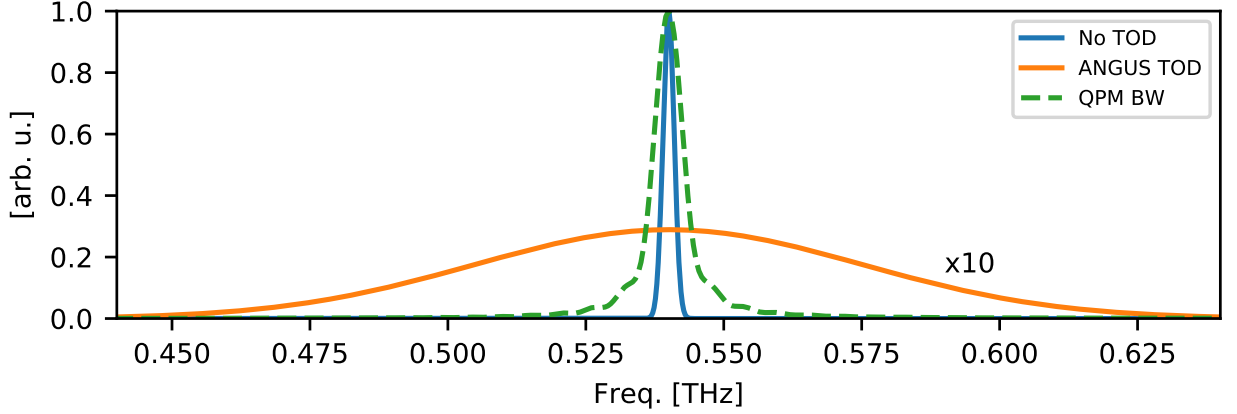


Figure 5.10: The frequency content of ANGUS pulses at $\Delta t = 7.8$ ps (540 GHz) with and without TOD shown along with the QPM bandwidth in a 2 cm long PPLN crystal matched to that frequency (dashed line).

duration $\tau_L = \delta\omega_L \phi_2$. Using the linear term of the difference frequency at the optimum delay ($-\phi_3\Omega/\phi_2^2$) combined with the THz bandwidth $\delta\Omega$, the total duration of time that is producing THz can be found to be $(-\delta\Omega\phi_2^2)/(\phi_3\Omega)$. Dividing this finally by the stretched pulse duration one arrives on a first-order approximation of portion of the input pump pulse that is producing THz. This can be thought of a relative efficiency only due to the amount of TOD, $\eta_{\text{rel}}^{\text{TOD}}$, of:

$$\eta_{\text{rel}}^{\text{TOD}} \approx \left(\frac{\delta\Omega}{\Omega} \right) \left(\frac{\phi_2}{\phi_3\delta\omega_L} \right). \quad (5.21)$$

The first term depends only on the parameters of the produced THz, and the second term depends only on parameters of the NIR pump. With the ANGUS parameters and 1% relative THz bandwidth $\eta_{\text{rel}}^{\text{TOD}} \approx 0.06$ (defined to be 1 without TOD). This only applies with the assumptions previously noted for deriving the difference frequency, and of course also only applies for reasonably large ϕ_3 values, since it would diverge as ϕ_3 tends to zero. This is also assuming that $\delta\omega_L \gg \Omega$ so that the majority of NIR pump pulses are overlapping, therefore the NIR pump bandwidth should not be seen as a free parameter when only using this as a guide. This simple result shows clearly that the relative efficiency is lower for narrower bandwidth THz, and lower with larger TOD. Interesting however is that the relative efficiency in this relationship should increase with GDD.

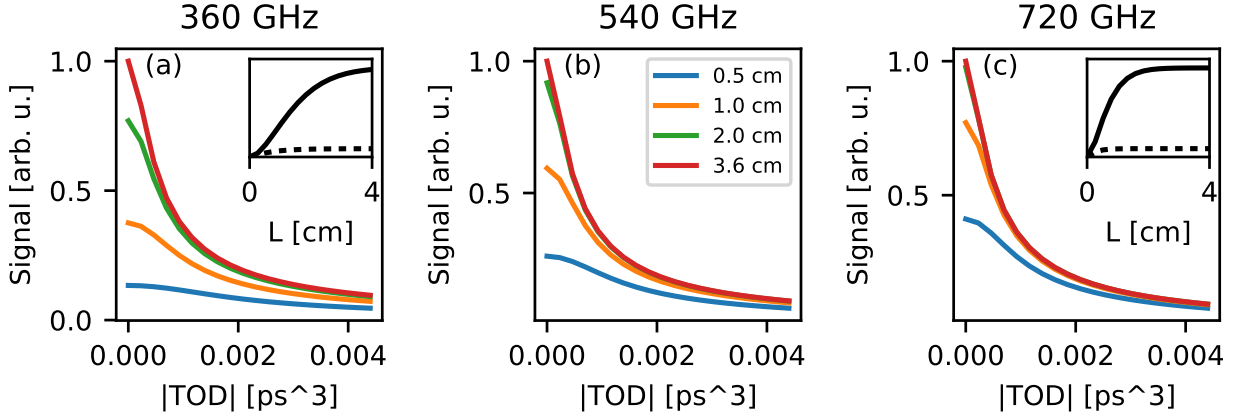


Figure 5.11: The effect of TOD on the THz generation efficiency for different frequencies and lengths with the ANGUS pump parameters in a PPLN crystal. Calculations are made with the FFT+analytic method and therefore do not take in to account cascading or other nonlinear effects. Shown are the continuous effect of TOD at 360, 540, and 720 GHz at lengths of 0.5, 1.0, 2.0, and 3.6 cm. Shown additionally as insets are the calculated THz output as a continuous function of length at 360 GHz and 720 GHz with zero TOD and TOD=-0.0044 ps³.

Going beyond the simple estimate, the output THz can be calculated at different lengths, frequencies, and TOD magnitudes as in the previous section using equation 5.2 and an FFT to calculate the difference frequency content. A basic visualization of this is shown in Figure 5.10 at 540 GHz. The frequency content with ANGUS parameters is shown with and without TOD (-0.0044 ps³) at $\Delta t = 7.8$ ps (with 2 pulses of equal energy), along with the QPM bandwidth from a 2 cm long crystal.

As was already shown at multiple frequencies when there is no TOD present the frequency content is narrow and fits completely within the bandwidth in this case. With TOD present the frequency content is much wider. Because the bandwidth in the presented example is wider than the frequency content without TOD the THz generation efficiency discrepancy is less than the ratio of the peaks shown, since the THz efficiency depends on the frequency integral of the product of the frequency content and QPM bandwidth. As the crystal becomes longer the bandwidth decreases, which increases the discrepancy between the output with and without TOD for this same reason.

The results of the detailed calculations at 360, 540, and 720 GHz frequencies for many

lengths using PPLN material properties and the ANGUS GDD and $\delta\omega_L$ are shown in Figure 5.11. As TOD is increased, output THz is significantly decreased. This decrease is more severe the longer the crystal, which corresponds to THz with a narrower bandwidth.

The unique properties of PPLN are represented in the increased absorption as the frequency increases. The output at 720 GHz reaches a given percentage of the maximum at a shorter length than at 360 GHz, which is due to the increased absorption and therefore a shorter absorption length. The insets show this effect for all length up to 4 cm, which is already well above the absorption length at 720 GHz.

5.6 Discussion of the effect on chirp of THz pulses

Because the analysis so far has only been in the frequency domain, the effect of the TOD on temporal properties of the THz has not been mentioned. When quasi-phase-matched one may posit that due to only a small portion of the pump pulses (in both frequency and time) being responsible for THz generation due to TOD, that the duration of the THz is significantly smaller than if the TOD was not present. However, the picture of the temporal extent of the pump pulses that is within the phase matching bandwidth in Figure 5.1(d) is not directly translatable to the temporal properties of the THz. This is due to the group velocity walk-off that still exists between the THz and NIR (despite being phase matched). The most extreme example of this is the multi-cycle nature of THz produced when pumping with a compressed pulse in PPLN, where pump pulses are some 100 fs, but THz pulses are still ~ 50 ps [71, 73, 76].

Outside of effects on the temporal envelope of the THz, it is also possible that the TOD imparts a chirp on the THz pulses. However, in the case of quasi-phase-matching in long PPLN crystals, the narrowband nature of the phase matching bandwidth allows for production of terahertz only at that very small range of frequencies within the bandwidth. It is sure that there is non-phase matched terahertz generated outside of the QPM bandwidth, but that would only contribute to possibly depleting the pump and not be present in the eventual high energy THz output. Taking into account that pulse duration is significantly determined by the crystal length and not only the temporal extent of the phase matched pump pulses, then the chirp in this case must be small.

The THz chirp b_{THz} will simply be defined as the derivative of the instantaneous frequency of the THz (non-angular frequency) such that

$$\nu_{\text{THz}}(t) = \nu_{0,\text{THz}} + b_{\text{THz}}t + \dots \quad (5.22)$$

If one imagines that over the entire pulse duration of the produced THz at 500 GHz central frequency, for example assuming $N=100$ total poled domain periods and therefore ~ 200 ps, the instantaneous frequency varies over the whole QPM bandwidth of ~ 5 GHz, then the chirp on the THz pulse would be quite small ($b_{\text{THz}} \approx 2.5 \times 10^{-5} \text{ THz}^2$). This can be expressed generally as the ratio of the THz bandwidth ($\sim \nu_{\text{THz}}/N$) to the THz pulse duration ($\sim N/\nu_{\text{THz}}$) producing an expression for the THz chirp $b_{\text{THz}} \approx (\nu_{\text{THz}}/N)^2$. In reality this is not exactly the case since the difference frequency content of the IR pulses always over-fills the QPM bandwidth even at one time, so this would just be an upper bound on the chirp from the QPM process.

It must be noted however, that if the THz generation process is not quasi-phase-matched (for example in thin nonlinear crystals [79]), or the phase matching is very broadband, then these arguments would not apply. The chirp on the THz would then be related directly to the linear term in the instantaneous angular frequency of the overlapped optical pulses $-\phi_3\Delta t/\phi_2^3$ derived earlier when $\Delta t = \phi_2\Omega$. So in a case such as this, without a limitation to the bandwidth, the chirp on the THz pulses would be significant as $b_{\text{THz}} = -\phi_3\nu_{\text{THz}}/\phi_2^2$, which differs only by a small factor from [139]. For ANGUS parameters ($\phi_2 = 2.3 \text{ ps}^2$, $\phi_3 = -0.0044 \text{ ps}^3$) at $\nu_{\text{THz}} = 500 \text{ GHz}$ this is $b_{\text{THz}} \approx 4.2 \times 10^{-4} \text{ THz}^2$. So in the case with no phase matching the chirp is 17 times larger than the *upperbound* with QPM. Therefore, if the chirped and delayed pulses are *copies* of each other and have TOD, the chirp must be expected or steps must be taken to remove it. Note that the higher the frequency is the larger the chirp. There may also be significant chirp present if the pulses are not exact copies. In two examples of chirp-and-delay in thin nonlinear crystals in the literature [81, 82] they use two separate OPAs that have specifically tuned GDD and TOD in order to produce THz and MIR pulses that have negligible chirp at the very small temporal delays relevant.

If the broadband pulse copies from ANGUS were used in a crystal such as GaP then matching the delay to a frequency band with low enough absorption and good enough phase

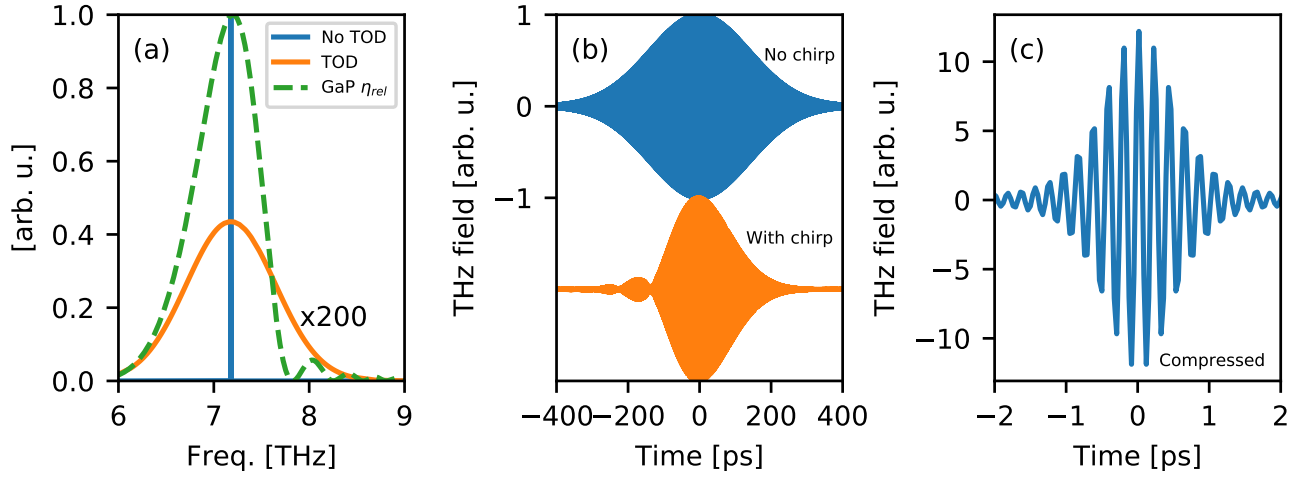


Figure 5.12: The frequency content of ANGUS pulses with $\Delta t = 103.75$ ps (7.179 THz) (a) with and without TOD, overlaid with the η_{rel} for 0.5 mm GaP (dashed). The THz pulses produced (b) with and without TOD on the pump pulses, that have either a linear chirp or flat phase respectively, and the THz pulse (c) if the chirped THz pulse were compressed.

matching, for example around 7.17 THz, the produced narrowband radiation would have roughly the spectral envelope of the entire difference frequency content, and a chirp corresponding to that derived in this section. This is shown in Figure 5.12, with ANGUS pulses at $\Delta t = 103.75$ ps for a 0.5 mm thick GaP. At 0.5 mm length the phase matching in the GaP is not quite as broadband as the frequency content when TOD is present, which additionally narrows the spectrum of the produced THz in addition to the chirp present.

In the case of the ANGUS parameters the THz produced when no TOD is present (Fig. 5.12(b)) has an extremely narrow bandwidth of 0.04% FWHM. In this case, contrary to quasi-phase-matching, the bandwidth of the THz depends on the pump pulses and not the crystal length. The THz produced when TOD is present has a larger bandwidth overall, but due to the chirp the envelope (and pulse duration) is only effected by the spectrum that is narrowed due to the limited phase matching in GaP. Figure 5.12(c) shows a THz produced that would result from compressing the broader chirped THz pulse produced when TOD is present on the pump. It could be that when driven strongly enough, compressing such pulses could result in very high field strength.

These calculations confirm that using such a pump with TOD would produce significantly different THz pulses than when TOD is not taken in to account. However, they also

show that if TOD were removed then the generated THz would be remarkably narrowband. From another point of view, varying the TOD on the pump pulses would also produce THz pulses with variable chirp, with a larger dynamic range at higher THz frequencies. These pulse could be either designed to have a certain chirp, or compressed to produce higher peak field.

5.7 Discussion of the effect of higher order terms

In addition to third-order dispersion, there are also higher order terms present in pulses stretched by most standard means. Although theoretically there are infinite orders for certain stretching methods, the relative magnitude decreases with order. This is the reason that the ideal theoretical predictions only considered the second-order phase (GDD) and this chapter has only treated so far the third-order phase (TOD). Of course the natural evolution is to consider the next order, fourth-order dispersion (FOD).

The two important theoretical considerations then are, what exact magnitude of FOD may a certain pulse have, and how is that FOD reflected in the temporal phase. So far only grating stretchers have been considered, since that is how the pulse is stretched for the laser involved in the experiments. Therefore only the FOD produced in a grating stretcher (Section 2.1.1) will be shown here. In the case of the ANGUS parameters the FOD is approximately $1.5 \times 10^{-5} \text{ ps}^4$.

Assessing the effect on efficiency requires knowledge of the effect of FOD on *temporal phase* and even more importantly the difference frequency. Unfortunately, the author has not found any analytic derivation of the exact temporal phase in terms of spectral phase orders above TOD. However, it is possible to guess this dependence via modeling a pulse in frequency domain including the FOD, taking the FFT, and unwrapping the phase. Repeating this procedure for the parameter space one can fit the GDD, TOD, and FOD to the quartic term in the temporal phase. This work is quite inexact, but a preliminary conclusion is that with including FOD there is a quartic term in the temporal phase proportional to ϕ_4/ϕ_2^4 . It would seem that the effect of such a term on the difference frequency is negligible, but due to the suspect nature of the analysis this should rather be determined experimentally.

5.8 Outlook

The effect of the TOD has been shown to be especially significant on the generation of THz with trains of chirped pulses. This effect applies for a wide-range of pump pulse properties and nonlinear media. In all cases the ANGUS properties were assumed for the pump pulses, and either PPLN or GaP were outlined for different regimes.

The first conclusion is that TOD changes the difference frequency content of the total pump IR energy, which is due to a varying difference frequency over time within the overlapped train of pulses. When there is additionally a longer train of >2 pulses the combination of TOD and this greater number of pulses adds complexity to the difference frequency content. Both the varying difference frequency and the increased complexity were shown via signatures in experimental results from quasi-phase-matching in PPLN driven by the ANGUS system at sub-THz frequencies.

The TOD effects go even further, as the change in the difference frequency content results as well in a decrease in the efficiency of the THz generation process via quasi-phase-matching. This was shown to be an effect of over an order of magnitude in calculations also for sub-THz frequencies in cm-scale length PPLN. This is most important for the work in this thesis, as it motivates the compensation of the TOD to increase the output THz energy.

Lastly, the effect of the TOD on broadband phase matched DFG was shown in the example of sub-mm length GaP (at a frequency of ~ 7 THz). In this case there are two effects: chirp that must exist when phase matching is broadband and the exact shape of relative efficiency due to material properties (due to changes in phase matching over the bandwidth of the frequency content). The combination of the chirp and spectral shape result in a drastically different THz pulse when TOD is present on the IR pump. If the TOD were removed on the pump, then the chirp on the THz would be removed and in this example the bandwidth could be as low as 0.04%. Conversely, if the chirped pulse would be compressed then few-ps long THz pulses could be produced, potentially at high energy.

Chapter 6

Asymmetric compensation of higher order phase effects for high-energy terahertz generation in PPLN

Parts of the work in this chapter were first shown preliminarily in the dissertation of F. Ahr [120]. N.H. Matlis should be given credit for the initial idea of asymmetric chirp compensation, derived and implemented experimentally in this chapter. The results presented in this chapter are being prepared for submission in a peer-reviewed journal.

In this chapter, motivated by the significant effect of TOD on the efficiency of the quasi-phase-matched chirp-and-delay process outlined in the previous chapter, methods for compensating for the TOD are outlined. After choosing the most viable method, experimental results along with a detailed analysis show the successful compensation for most of the negative effects of the TOD on output efficiency. With this compensation output energies of sub-mJ-level are reached.

Note that all results here are reported at cryogenic temperatures, since this is inarguably shown to increase output efficiencies and is therefore the most interesting regime.

6.1 Study for compensation of third-order phase

As described in the previous chapter, the third-order phase (TOD) affects the efficiency and therefore also total energy of generated THz in the chirp-and-delay experiments. This section provides an analysis of possible methods to compensate for this TOD in order to increase efficiency, and of course in the end to have a net higher THz energy.

The first possibility is to completely remove the TOD present in the pulses. The DAZZLER, an acousto-optic dispersive filter, is a device that uses acoustic waves in an active crystal to imprint semi-arbitrary spectral amplitude and phase modulations onto an optical pulse of suitable properties [89]. Although in general the DAZZLER can be used very well to compensate

for leftover phase or spectral aberrations up to fourth-order in a compressed pulse (to optimize pulse duration or pulse temporal profile), there is not sufficient dynamic range to compensate for relevant magnitudes of spectral phase to effect stretched pulses as in our experiment. Therefore, the DAZZLER in the ANGUS system is not suitable for the purpose of completely removing the TOD on its pulses.

Any transparent material with a wavelength dependent refractive index has well-defined dispersive properties as well, which could be a candidate for removing the TOD. For the grating stretcher for example, the phase change applied to a pulse depends on the path length of the various wavelengths, and the derivatives. The DAZZLER is more user-friendly in the sense that a software can apply specific phase values, which are then physically applied by the acoustic wave which is affecting the laser pulse. In the case of transparent materials, the various spectral phase values, in the same language as has been used so far (i.e. fs², fs³, etc) are related to wavelength derivatives of the refractive index, through the spatial frequency $k = n\omega$.

$$\frac{\phi_1}{L} = k' \equiv \frac{\partial k}{\partial \omega} = \frac{1}{c} \left[n + \frac{\partial n}{\partial \omega} \right] = \frac{1}{c} \left[n - \frac{\partial n}{\partial \lambda} \right] \quad (6.1)$$

$$\frac{\phi_2}{L} = k'' \equiv \frac{\partial^2 k}{\partial \omega^2} = \frac{1}{c} \left[2 \frac{\partial n}{\partial \omega} + \omega \frac{\partial^2 n}{\partial \omega^2} \right] = \frac{\lambda^3}{2\pi c^2} \frac{\partial^2 n}{\partial \lambda^2} \quad (6.2)$$

$$\frac{\phi_3}{L} = k''' \equiv \frac{\partial^3 k}{\partial \omega^3} = \frac{1}{c} \left[3 \frac{\partial^2 n}{\partial \omega^2} + \omega \frac{\partial^3 n}{\partial \omega^3} \right] = \frac{-\lambda^4}{4\pi^2 c^3} \left[3 \frac{\partial^2 n}{\partial \lambda^2} + \lambda \frac{\partial^3 n}{\partial \lambda^3} \right] \quad (6.3)$$

$$\frac{\phi_4}{L} = k^{(4)} \equiv \frac{\partial^4 k}{\partial \omega^4} = \frac{1}{c} \left[4 \frac{\partial^3 n}{\partial \omega^3} + \omega \frac{\partial^4 n}{\partial \omega^4} \right] = \frac{\lambda^5}{8\pi^3 c^4} \left[12 \frac{\partial^2 n}{\partial \lambda^2} + 8\lambda \frac{\partial^3 n}{\partial \lambda^3} + \lambda^2 \frac{\partial^4 n}{\partial \lambda^4} \right], \quad (6.4)$$

where all derivatives are evaluated at the central frequency or wavelength. With these equations the magnitude of the phase of each order, per unit length, can be calculated for a material for which the refractive index data exists as a function of wavelength or frequency. An example is SF11 glass, which has approximately $\sim 126 \text{ fs}^3/\text{mm}$ of TOD/mm at 800 nm. However, since the ANGUS pulses have $-4.4 \times 10^6 \text{ fs}^3$ of TOD, 34 m of SF11 would be required to completely remove the TOD on the pulses. It is clear that beyond the ability to even get so much SF11, that other mechanisms such as self-focusing would spoil the propagation through such a length of glass, and the pulse would be stretched massively in time due to the group velocity dispersion (k'') that is also present in SF11.

Dispersive mirrors are also a possible component-level solution to the TOD problem. Rather than providing a dispersion due to properties of a bulk material, dispersive mirrors have a complex multi-layer coating such that dispersion is experienced only during reflection. The layers can have varying thickness and composition such that a large parameter set is available to design the mirrors so as to allow for a large enough bandwidth for ultrashort pulses and to provide a tunable dispersion. These mirrors are often designed to have a specific value of GDD in order to, for example, compensate for accumulated GDD in a hollow-core fiber compressor [140]. It is also possible to rather provide a designed (but limited) TOD per reflection.

However, suppliers cannot provide mirrors than can compensate for even 1% of the TOD that is present in our stretched pulse. For example Layertec GmbH can compensate up to 500-1000 fs³ per reflection, FEMTOOPTICS (Spectra-Physics) can compensate up to 2400 fs³ per reflection, and Ultrafast Innovations can compensate up to 20000 fs³ per reflection. Even with tens of bounces the effect could only be on the percent level, and the aperture and damage threshold of these products is quite limited. The number of bounces necessary for meaningful compensation is essentially intractable with the beam diameter above 1 cm and beam energy above 100 mJ that are used in these experiments.

So far three simple components have been outlined that theoretically could compensate for the total TOD, but in practice cannot handle the amount present in the ANGUS pulses. The following are two methods that are reasonable, the first of which can completely remove the TOD present on the pulses, and the second is to only slightly tune the phase on each pulse which is shown to also compensate for the effects of TOD.

6.1.1 De-tuned grating compressor

Since all other methods cannot provide enough TOD to compensate for that in the stretched pulse, then it is possible to compensate partially for the TOD, or completely, while also decreasing the GDD on the pulse using a grating compressor [139]. It makes sense that since a grating stretcher has imparted such a large GDD and TOD, a compressor can equally remove them. Although this also decreases the maximum fluence possible on the crystal, it can accomplish what the other methods cannot.

Since the initial GDD and TOD on the pulse are known, this second compressor could simply compensate for each depending on the angle and separation of the gratings.

$$\phi_2 = \phi_2^{(0)} - \frac{\lambda_0^3 L}{\pi c^2 d^2 \cos^2(\theta_r)} \quad (6.5)$$

$$\phi_3 = \phi_3^{(0)} + \frac{3\lambda_0^4 L}{2\pi^2 c^3 d^2 \cos^2(\theta_r)} \left[1 + \frac{\lambda_0 \sin(\theta_r)}{d \cos^2(\theta_r)} \right] \quad (6.6)$$

The free parameters are as always angle of incidence (AOI, contained within the diffracted angle θ_r) and distance between the gratings L only the central wavelength ray. In order to have zero TOD, the relationship between these set parameters is fixed:

$$\phi_3 = 0 \quad (6.7)$$

$$L = \frac{-2\pi^2 c^3 d^2 \cos^2(\theta_r) \phi_3^{(0)}}{3\lambda_0^4 \left[1 + \frac{\lambda_0 \sin(\theta_r)}{d \cos^2(\theta_r)} \right]} \quad (6.8)$$

$$\phi_2 = \phi_2^{(0)} + \frac{2\pi c \phi_3^{(0)}}{3\lambda_0 \left[1 + \frac{\lambda_0 \sin(\theta_r)}{d \cos^2(\theta_r)} \right]}. \quad (6.9)$$

With the input to the compressor defined as having the ANGUS properties, the constraints for such a partial compressor are shown in Figure 6.1. There is a fixed relationship between the AOI and distance to have an output with zero TOD, but then the output GDD is fixed at a given set point. This output GDD is an additional possible constraint, since it means that the pulse duration of the zero-TOD pulses is now significantly shorter. This decreases the damage threshold on the crystal (and all optics), and also may have even more complex implications since the delays necessary to generate THz are now shorter ($\Delta t_{\text{opt}} = \phi_2 \Omega$).

There are even more hidden constraints however, since the grating compressor cannot have arbitrary physical dimensions. As the AOI is decreased the grating distance also decreases in order to maintain zero TOD output. This means the beam size that would fit in such a compressor gets too small. As the AOI is increased the distance also increases and it could become practically untenable. Lastly, gratings have a relatively low damage threshold themselves, which would likely be the limiting factor for total pump energy in the setup.

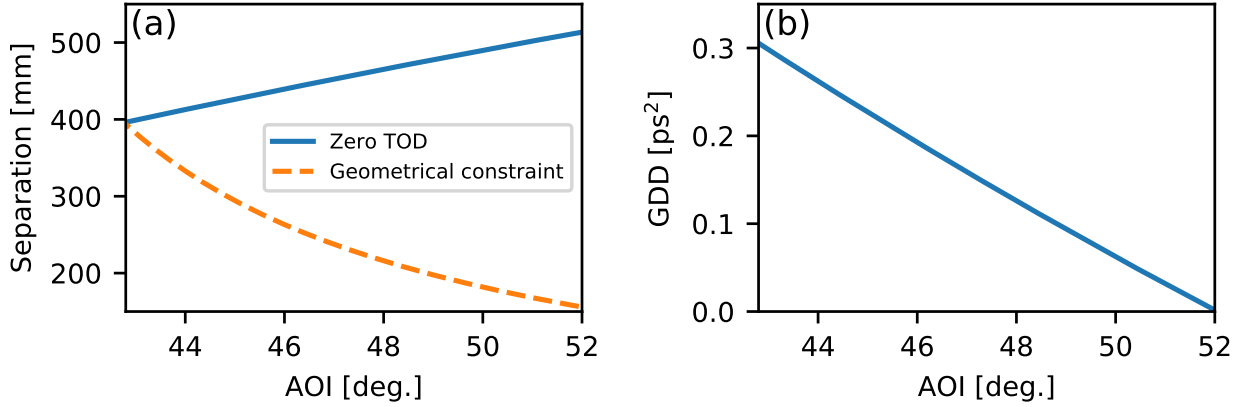


Figure 6.1: (a) Plot showing example parameters [angle of incidence (AOI), separation] for a 1480 lines/mm grating compressor such that the TOD would be set to zero at the output along with an example of a geometrical constraint on the minimum grating separation due to finite grating width, and (b) the remaining GDD at each set grating configuration corresponding to zero TOD.

For the reasons outlined this method was not chosen, but rather the asymmetric method in the following section.

6.1.2 Asymmetric compensation of phase

N.H. Matlis proposed the idea to compensate for the phase in only one pulse slightly to optimize the process. The idea was inspired by the slope of the dip in the output IR spectrum detailed in the previous chapter, but indeed it is inherent to the spectral phase.

By modifying only one pulse it may be possible to use much smaller total changes to accomplish the same result as if the TOD is completely removed. A Wigner-style plot showing this concept now contrasting to the default case with TOD can be seen in Figure 6.2.

The analysis of this concept is similar to the analysis for the difference frequency content of a train of identical pulses, except that now the spectral phase is not the same in each pulse. They are not identical copies of each other. Then there are two equations for instantaneous frequency, and the difference frequency content depends on the difference of these two

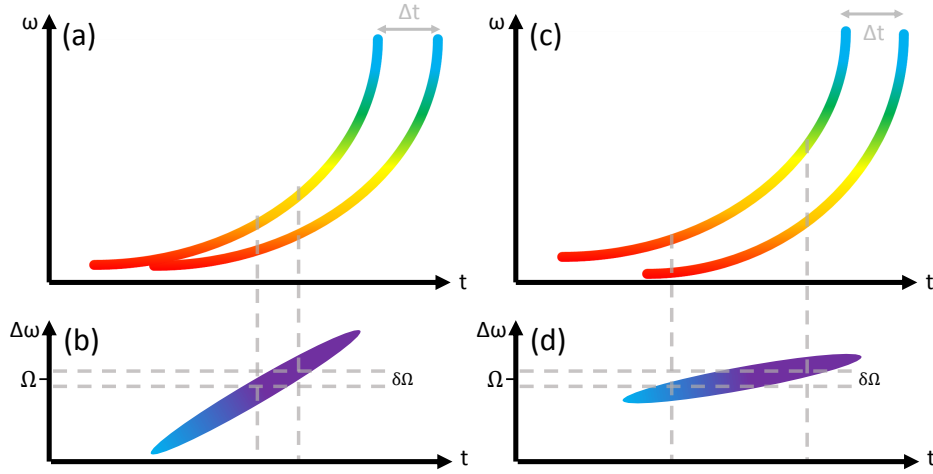


Figure 6.2: Chirp and delay Wigner plot showing the case with TOD and exact pulse copies, and an example of an increase in useful difference frequency content when only modifying one pulse. (a) and (b) are with TOD, but the pulses are exact copies. (c) and (d) are an example where only the pulse on the right in (c) has had its slope and curvature modified such that more of the difference frequency content is within the THz bandwidth $\delta\Omega$.

$$\omega_1(t) = \omega_0 + \frac{1}{\phi_2^{(1)}}t - \frac{\phi_3^{(1)}}{2(\phi_2^{(1)})^3}t^2 \quad (6.10)$$

$$\omega_2(t) = \omega_0 + \frac{1}{\phi_2^{(2)}}t - \frac{\phi_3^{(2)}}{2(\phi_2^{(2)})^3}t^2 \quad (6.11)$$

$$\Delta\omega(t) = |\omega_1(t) - \omega_2(t - \Delta t)|. \quad (6.12)$$

The calculation is made as follows: the GDD and TOD in the unchanged pulse, $\phi_2^{(1)}$ and $\phi_3^{(1)}$ are known properties of the laser, and the unknowns are the properties of the second pulse, $\phi_2^{(2)}$ and $\phi_3^{(2)}$, and the delay between the two Δt . Note that the delay can be positive or negative in this scenario. Since the pulses are no longer identical the sign of the temporal delay is significant.

The difference frequency is the following, which is the same as from the previous chapter, only now with less simplification and updated notation:

$$\Delta\omega(t) = \left[\frac{\Delta t}{\phi_2^{(2)}} + \frac{\phi_3^{(2)} \Delta t^2}{2(\phi_2^{(2)})^3} \right] + \left[\frac{1}{\phi_2^{(1)}} - \frac{1}{\phi_2^{(2)}} - \frac{\phi_3^{(2)} \Delta t}{(\phi_2^{(1)})^3} \right] t + \left[\frac{\phi_3^{(2)}}{2(\phi_2^{(2)})^3} - \frac{\phi_3^{(1)}}{2(\phi_2^{(1)})^3} \right] t^2. \quad (6.13)$$

The optimal scenario is when the difference frequency does not depend on time at all across the pulse, and the phase matching condition is met ($\Delta\omega = \pm 2\pi\nu_{\text{THz}}$). These assumptions result in the following three equations:

$$\pm 2\pi\nu_{\text{THz}} = \frac{\Delta t}{\phi_2^{(2)}} + \frac{\phi_3^{(2)} \Delta t^2}{2(\phi_2^{(2)})^3} \quad (6.14)$$

$$0 = \frac{1}{\phi_2^{(1)}} - \frac{1}{\phi_2^{(2)}} - \frac{\phi_3^{(2)} \Delta t}{(\phi_2^{(1)})^3} \quad (6.15)$$

$$0 = \frac{\phi_3^{(2)}}{2(\phi_2^{(2)})^3} - \frac{\phi_3^{(1)}}{2(\phi_2^{(1)})^3}. \quad (6.16)$$

The solution to this set of equations is:

$$\phi_2^{(2)} = \frac{(\phi_2^{(1)})^{3/2}}{\sqrt{\phi_2^{(1)} \mp 4\pi\nu_{\text{THz}}\phi_3^{(1)}}} \quad (6.17)$$

$$\phi_3^{(2)} = \frac{(\phi_2^{(1)})^{3/2}\phi_3^{(1)}}{(\phi_2^{(1)} \mp 4\pi\nu_{\text{THz}}\phi_3^{(1)})^{3/2}} \quad (6.18)$$

$$\Delta t = \frac{\phi_2^{(1)}}{\phi_3^{(1)}} \left[\phi_2^{(1)} - \phi_2^{(2)} \pm 4\pi\nu_{\text{THz}}\phi_3^{(2)} \frac{\phi_2^{(2)}}{\phi_2^{(1)}} \right]. \quad (6.19)$$

This is a nice compact result, which shows that if GDD and TOD are added to only one pulse then the difference frequency can be flat for all time (assuming there are no higher orders). With the ANGUS properties for 361 GHz the resultant changes in GDD and TOD predicted are 10046 fs² and -57905 fs³ respectively. At 558 GHz the predicted changes in GDD and TOD necessary for optimum compensation are 15583 fs² and -90000 fs³ respectively. These are two orders of magnitude below the total TOD on the pulse, and now much more easily accessible. The impact on the difference frequency can be seen in Figure 6.3 for various intermediate cases.

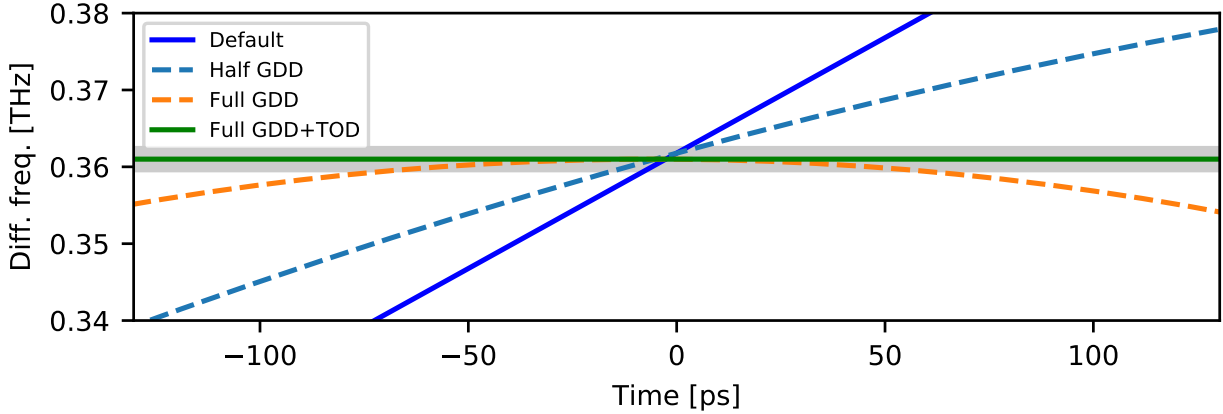


Figure 6.3: As the compensation is increased to the ideal amount with only GDD, the difference frequency bends so that a higher proportion of the total pulse overlap (200 ps) is within the QPM bandwidth indicated in grey. With full GDD compensation ($\Delta\phi_2 = 10046 \text{ fs}^2$) some part of the overlapped pulses is still not within the bandwidth, but it can be optimized further by adding the TOD compensation ($\Delta\phi_3 = -57905 \text{ fs}^3$).

As compensation gets closer to the ideal, a greater portion of the overlapped pulses in time (in this case ~ 200 ps long) has a difference frequency within the shown 1 % QPM bandwidth.

In the less general case where one can only tune the GDD for example, and therefore only have $\phi_2^{(2)}$ different from the laser parameters, then the difference frequency is similar to before

$$\Delta\omega(t) = \left[\frac{\Delta t}{\phi_2^{(2)}} + \frac{\phi_3 \Delta t^2}{2(\phi_2^{(2)})^3} \right] + \left[\frac{1}{\phi_2^{(1)}} - \frac{1}{\phi_2^{(2)}} - \frac{\phi_3 \Delta t}{(\phi_2^{(1)})^3} \right] t + \left[\frac{\phi_3}{2(\phi_2^{(2)})^3} - \frac{\phi_3}{2(\phi_2^{(1)})^3} \right] t^2, \quad (6.20)$$

but now with $\phi_2^{(2)}$ and Δt as the only free parameters, the difference frequency can only have the linear component removed, summarized in the following constraints:

$$\pm 2\pi\nu_{\text{THz}} = \frac{\Delta t}{\phi_2^{(2)}} + \frac{\phi_3 \Delta t^2}{2(\phi_2^{(2)})^3} \quad (6.21)$$

$$0 = \frac{1}{\phi_2^{(1)}} - \frac{1}{\phi_2^{(2)}} - \frac{\phi_3 \Delta t}{(\phi_2^{(1)})^3}. \quad (6.22)$$

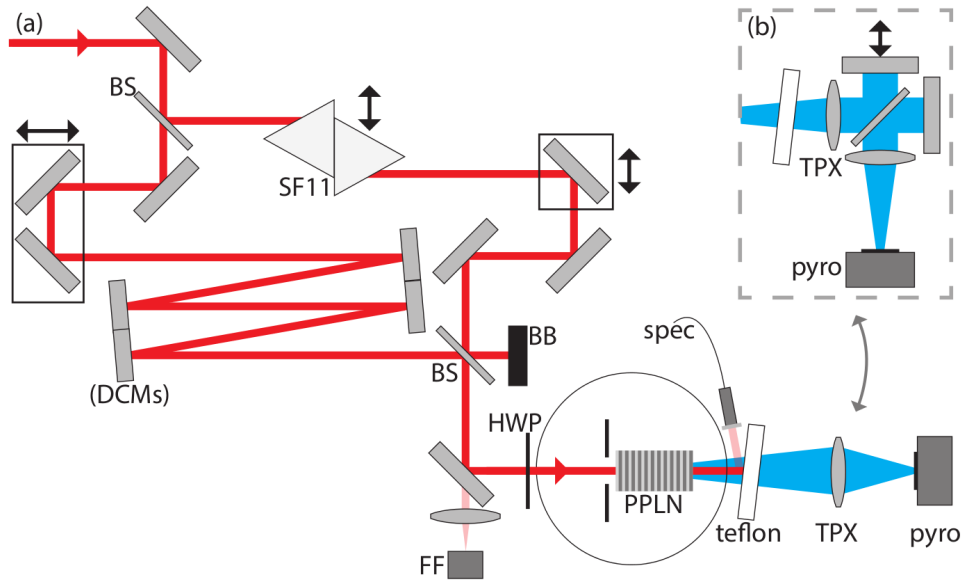


Figure 6.4: A diagram of the experimental setup in this chapter (a) with the longitudinal interferometer (correlator) used for frequency measurement (b). **Key:** BS: beamsplitter; DCMs: dispersion compensating mirrors; BB: beam block; FF: farfield camera; spec: optical spectrometer; pyro: pyro-electric detector.

There are other permutations of this concept, but the important conclusion is that full compensation now is experimentally accessible with readily available components. The rest of the chapter will outline the implementation and results from this method.

6.2 Experimental overview

An overview will be provided of various specific topics relevant to the measurements that will later be presented in this chapter. All measurements are at cryogenic temperatures of 82-92 K, achieved via a vacuum chamber dewar and liquid nitrogen cooling. All crystals used in these experiments are from Prof. Taira [130] with 10x15 mm² input aperture and 36 mm length. The crystals were pumped with a 13 mm diameter beam, which was clipped via a ceramic mask before the crystal input in order to fit onto the input facet.

A Mach-Zehnder-like setup (Fig. 6.4(a)) splits the pulses into copies via beamsplitters (BS), where they can be manipulated independently. In one arm the pulses can travel through a variable amount of SF11 glass, and in the other they can reflect of a varying amount of

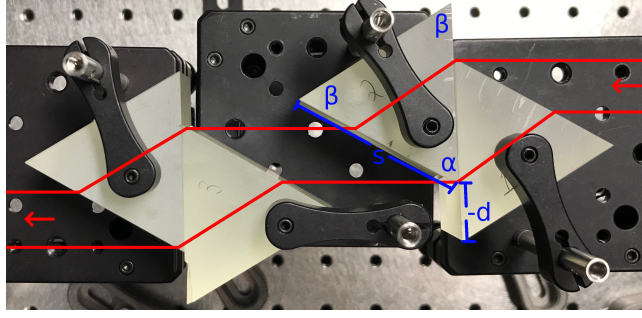


Figure 6.5: A diagram of the optical path (red) through a pair of SF11 prisms. The angles α and β (blue) are designed according to the material and design wavelength of 800 nm. The length of propagation within the medium then depends only on the geometry ($s = 50 \text{ mm}$) and the amount of overlap between the two crystals d . In this case shown $d = -15$ on both prisms such that the total length of SF11 is 69 mm.

high-TOD mirrors (DCMs). In the arms of the TOD mirrors there is a translate stage to freely tune the delay and in the arm of the prisms there is a translation stage to recover alignment for varying amounts of SF11. The pointing of the two arms is measured at the sub-mrad level to ensure proper phase matching using the farfield camera (FF) behind the last steering mirror. The output IR spectrum after generating THz is measured from the scattering of the teflon used to separate the IR and THz at the output of the crystal. The THz is either focused or collimated with 150 mm focal length TPX lenses for the energy measurement or frequency measurement respectively. The beamsplitter within the interferometer is silicon, which is close to 50/50 splitting for our sub-THz frequencies.

6.2.1 SF11 prisms

SF11 glass is used as the high-dispersion material to provide the $\Delta\phi_2$ due to its very high GVD of $187.5 \text{ fs}^2/\text{mm}$ [141] compared to other glasses and availability in prisms already suited for 800 nm.

The prisms are designed such that the base angle β is equal to the Brewster's angle at the desired wavelength, in this case 800 nm. Because the index of refraction of SF11 at 800 nm is 1.765 [141], $\alpha = 59^\circ$ and $\beta = 60.5^\circ$. In order for the laser beam to propagate through the pair of prisms properly, the apex angle corners must be opposite to each other, and the path within the prism must be parallel to the base (for there to be no spatial or angular chirp). This

fixes in addition $\theta_i = \theta_B$.

The last property for this alignment is the amount of SF11 traversed for a given setup. It is useful to define a variable d , which is the length in addition to matched prisms on the mated sides. In other words, when the prisms are mated corner-to-corner $d = 0$. So d is the overhanging face on the second prism, and is positive when the length through the prisms is larger than the length of the base. With this definition of d , simply for experimental convenience the length traversed through the SF11 is

$$L = (s + d)\sqrt{2(1 - \cos(\alpha))} = 0.985 \times (s + d), \quad (6.23)$$

where s is the length of the non-base side. An example of this can be seen in Figure 6.5 with two prism pairs, where $d = -15$ mm in both pairs, so that the total length is $2 \times (50 - 15) \times 0.985 = 69$ mm. The amount of GDD added is just proportional to this length.

6.2.2 High-TOD chirped mirrors

In order to additionally compensate the TOD outside of the effect of the SF11 glass, specialized high-TOD mirrors are needed. These are special custom optics from Ultrafast Innovations [142] that aim to provide only TOD and not other orders of phase for every reflection. The specifications of the optics were 20000 fs^3 at 5° angle of incidence, and the optics have a 2 inch diameter.

Although the company initially provided detailed specifications, they were not direct measurements of the phase. We set out to do our own measurements, with great help from Shih-Hsuan Chia [143] of F.X. Kärtner's group. Three samples were measured, including one at two positions using white-light interferometry (WLI) [144]. There was a total of 54 measurements to enable averaging. All three samples showed similar results, and the results are shown in Figure 6.6(b) and (c). After producing these data and sending them to the company we then received measurements from them to confirm those done at DESY (Fig. 6.6(a)).

The way that the TOD is calculated is as follows. The WLI measures the group-delay (GD) as a function of wavelength. The TOD can then be calculated using this, either by fitting

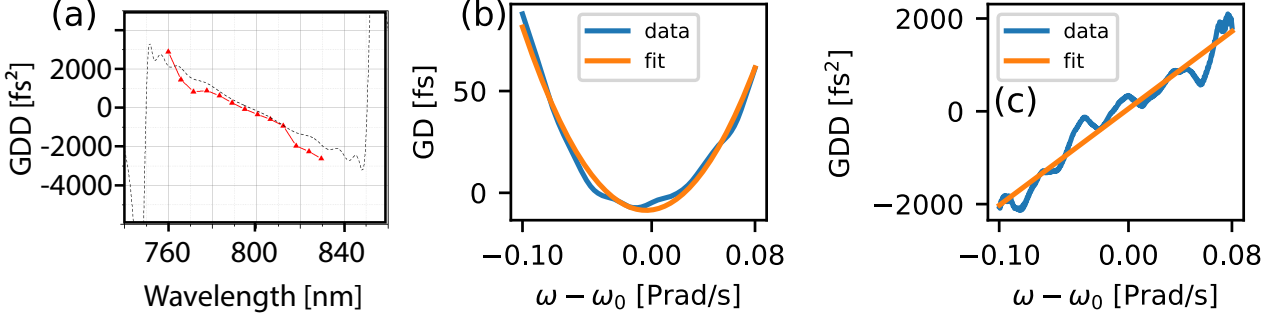


Figure 6.6: **(a)** Specifications (blue) and measurements (red) provided by the supplier for the high-TOD mirrors, and measurements performed at DESY with white-light interferometer showing the group delay (GD) measured **(b)** and the GDD calculated **(c)** from the derivative of the GD. The TOD can be calculated by either the quadratic term of the fit to the GD or the linear term of the fit to the GDD. Both result in values around 20000 fs³, although there is obvious noise in all measurements.

a parabola to the GD, or taking the derivative to get the GDD and then fitting a line. Both methods showed good agreement, calculating 20800 fs³ and 19800 fs³ respectively.

$$GD(\omega) = \phi_1 + \phi_2(\omega - \omega_0) + \frac{\phi_3}{2}(\omega - \omega_0)^2 \quad (6.24)$$

$$GDD(\omega) = \phi_2 + \phi_3(\omega - \omega_0) \sim \frac{-2\pi c\phi_3}{\lambda_0^2}(\lambda - \lambda_0) \quad (6.25)$$

The specifications and measurements provided by the supplier were given on the wavelength axis, so a simple conversion is necessary, as shown in the equation. Since all methods agree, then the mirrors can be deemed suitable. The significant presence of noise and oscillations in all measurements may however be a source of error, and the implications are not known.

6.2.3 Glass wafer for THz outcoupling

A significant engineering challenge on the path reaching the highest total efficiency of THz generation is removal of simple Fresnel losses at the output facet of the THz crystal. Although it is not directly related to the spectral phase compensation discussed and measured

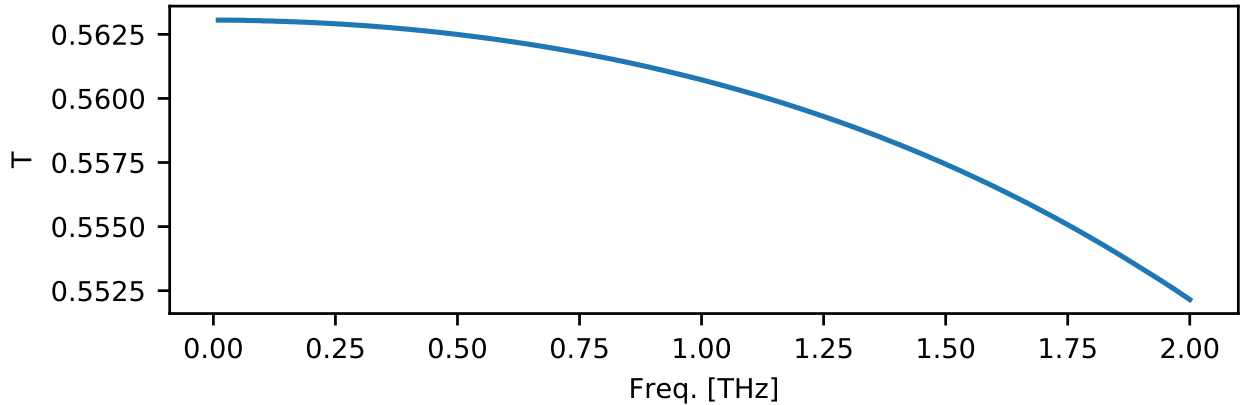


Figure 6.7: The expected Fresnel transmission at the PPLN exit surface for varying frequencies based on a fit to measured refractive index in [126] extrapolated to 80 K.

in this chapter, it is a crucial step in the path towards the highest usable THz pulse energies. Note that since these losses are due to the crystal face, they would be present even if the entire experiment were inside vacuum.

The Fresnel losses are relatively simple in terms of the refractive index of the medium

$$T_{\text{exit}} = 1 - \left(\frac{n_{\text{LN}}(\nu_{\text{THz}}) - 1}{n_{\text{LN}}(\nu_{\text{THz}}) + 1} \right)^2, \quad (6.26)$$

but since the refractive index of lithium niobate is so large in the THz range, the transmission at the output surface is only 56% for the range of frequencies relevant for lithium niobate (up to 1.5 THz).

This problem can be solved in a very similar fashion to simple single-layer AR coatings. These follow the rule that in order to have the ideal Transmission of 100% the AR coating should have $n_{\text{coating}} = \sqrt{n_{\text{medium}}}$ and the thickness of the outcoupling plate d of a quarter wave within the outcoupling plate material $d = c/(4n_{\text{coating}}\nu_{\text{THz}})$. This allows for the reflections at both surfaces to be equal and for them to constructively interfere in the forward direction, allowing for full transmission. With LN material parameters at cryogenic temperatures this requires a material with a THz refractive index around 2, and thickness of around 50-100 μm .

However, there is the additional engineering challenge of outcoupling the IR pump radia-

tion, which may be desirable for thermal management or damage threshold reasons, in addition to having unobstructed output diagnostics on the IR pulses. With an output surface already coated for IR wavelengths, the THz outcoupling plate can no longer be flush with the output surface. Therefore there must be a vacuum (or air) spacing between the output surface of the LN crystal and the THz outcoupling plate that is significantly thicker than the IR pump wavelength, but not thick enough to effect the performance of the THz outcoupling plate.

This can be analyzed with the so-called transfer-matrix method [145] where a matrix M represents the propagation of a electromagnetic wave through a medium ($k = 2\pi n/\lambda$) over a certain distance d

$$M = \begin{bmatrix} \cos(kd) & \sin(kd)/k \\ -k \sin(kd) & \cos(kd) \end{bmatrix}, \quad (6.27)$$

such that $(E(z+d), dE(z+d)/dz) = M \times (E(z), dE(z)/dz)$. The formalism is such that for multiple layers of materials with different thicknesses and refractive indices a system matrix M_s that represents the propagation through the entire N layer system is simply $M_s = M_N \dots M_2 M_1$. The transmission through any such system of layers is

$$T = \frac{k_N}{k_0} \left| \frac{2ik_0 e^{-ik_N L}}{-M_{21} + k_0 k_N M_{12} + i(k_N M_{11} + k_0 M_{22})} \right|^2, \quad (6.28)$$

where k_N, L are the wave number and thickness of the last layer, k_0 the wavenumber of the initial layer, and M_{xx} the matrix elements of total matrix for the system of layers.

With this formalism the transmission can be exactly calculated for the case relevant for THz outcoupling, which is a small vacuum gap between the lithium niobate and a plate of design thickness. This is a two layer system, with one layer vacuum and the other layer the THz outcoupling plate material.

Because simple fused silica or quartz has a refractive index just below 2 in the THz range [146], this is an ideal material for constructing the outcoupling plate. Additionally, precise sheets of aluminum foil can very easily have order $10 \mu m$ thickness, which is large enough to space the plate from the crystal exit surface. These parameters, in addition to the narrow range of generated frequencies from 0.3-0.6 THz will be calculated here.

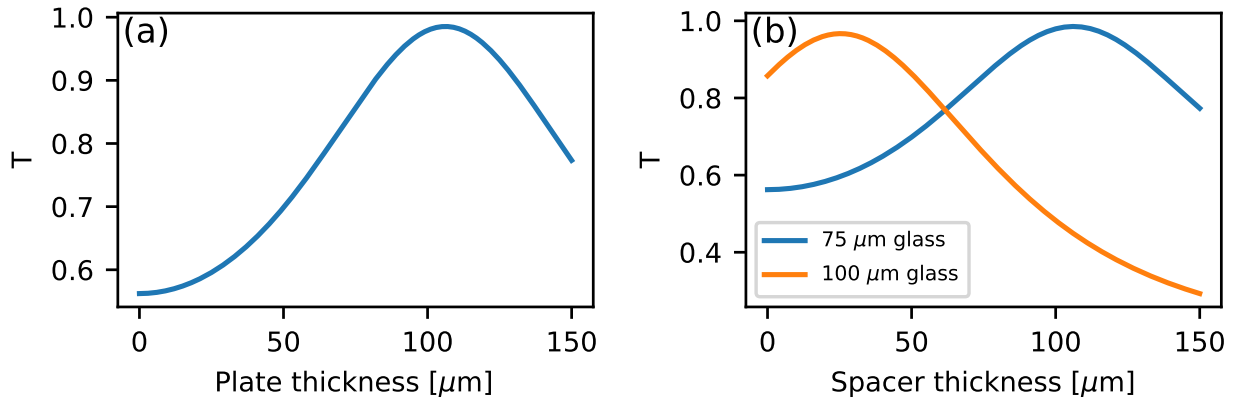


Figure 6.8: Transmission at the LN rear surface for 360 GHz radiation for varying glass plate thickness (a) and for varying vacuum spacing thickness for a 75 μm or 100 μm glass plate (b). Assuming a glass refractive index of 1.962 [146].

Seen in Fig. 6.8 is the transmission of 360 GHz radiation through a glass layer of varying thickness, and the transmission through a glass plate of 75 μm or 100 μm thickness with a varying vacuum distance between the plate and the crystal exit surface. Note that with the 75 μm there is a very close to ideal regime where the vacuum spacing is above 10 μm , but less than 50 μm . This means that using thin aluminum foil as a spacer, with an added thickness margin in anticipation of warping of the thin foil during installation, could be a successful method.

Fig. 6.9 shows similarly the transmission of 558 GHz radiation through a glass layer of varying thickness, and the transmission through a glass plate of 50 μm or 75 μm thickness with a varying vacuum distance between the plate and the crystal exit surface. There is a regime also quite close to the ideal 100% with similar vacuum spacing distances. So with this higher frequency and a thinner plate the foil spacer is still a potentially valid solution.

Fig. 6.10 shows an installed glass plate of the rear surface of the 330 μm crystal, with and without strips of 10 μm aluminum foil as a spacer (outside of the beam path) clamped to the crystal surface with two small and thin copper plates acting as leaf springs. When the wafer is attached directly to the surface the performance is better, however dust particles can be trapped between the surfaces which can either cause damage via heating or scratches during

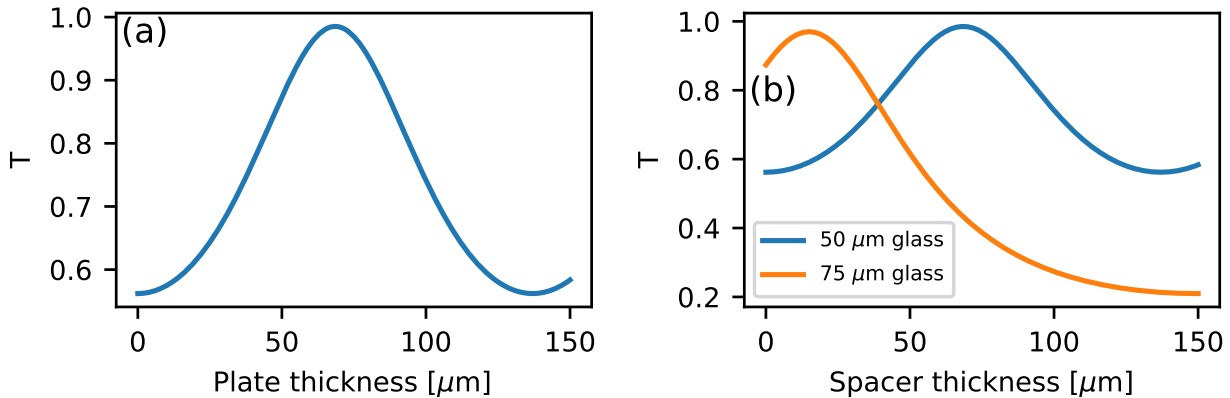


Figure 6.9: Transmission at the LN rear surface for 558 GHz radiation for varying glass plate thickness (a) and for varying vacuum spacing thickness for a 50 μm or 75 μm glass plate (b). Assuming a glass refractive index of 1.962 [146].

the cooling process. With the aluminum foil spacer there is potential for better functionality, but in our case it is likely that the foil did not retain its minimum thickness and became warped therefore spoiling the process. Measurements at 360 GHz with the 75 μm quartz wafer with the foil spacer showed a decrease to below 50 %. Even measurements at 360 GHz without the foil spacer and using the 100 μm fused silica wafer only showed a modest increase of $\sim 10\%$.

6.2.4 Purging of detection setup for calibration of absorption

For all of the measurements reported in the previous two chapters there was no purging involved. This is principally due to the fact that all THz radiation was very narrowband and well outside of significant absorption peaks. However, as will be explained in the following sections, radiation was generated at 558 GHz, which is very close to an absorption peak in humid air [147]. The experimental solution to this was to purge the volume where THz detection was taking place to ensure that the environment was free of water vapor. This was not done for the 361 GHz, since the absorption is orders of magnitude lower at this frequency.

The absorption peak is extremely narrow and near 556 GHz (Fig. 6.11(a)). The absorption at this peak and throughout the spectrum is mostly linearly dependent on the relative humidity (RH). The ANGUS laboratory is held at a very constant 51 % RH. An enclosure was

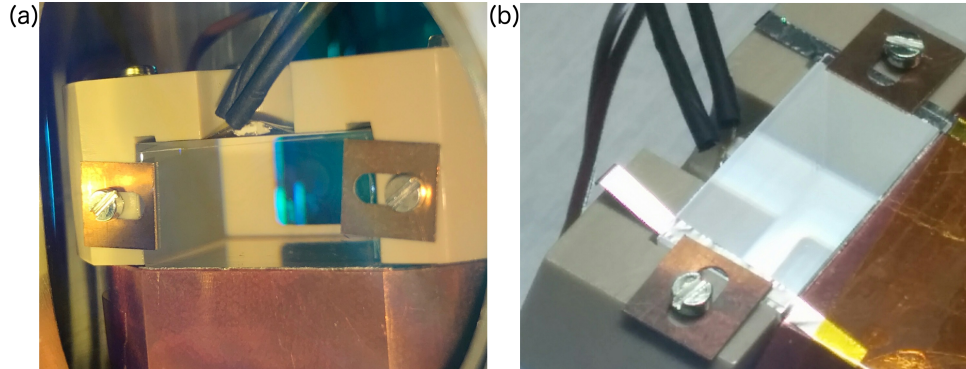


Figure 6.10: A photo of the installed $100\ \mu\text{m}$ fused silica plate **(a)** with no spacer, clamped to the PEEK holder. A photo of the installed $75\ \mu\text{m}$ quartz plate **(b)** with strips of $10\ \mu\text{m}$ foil. Both are on the output surface of the $10\times 15\ \text{mm}^2$ aperture, 36 mm long crystal producing 360 GHz radiation.

built with thick plastic walls and thin plastic foil covering areas where visual access is necessary (Fig. 6.11(d)). Two separate lines of dry Nitrogen were set to purge first the top of the enclosure with about 1 bar of pressure, and a small exit was left at the bottom of the enclosure to avoid any over-pressure.

Two measurement took place using this enclosure. The first was a test of the purging effect on the output THz at only this specific frequency of 558 GHz. After turning on the purge gas the output increased by 43% after only a few minutes (Fig. 6.11(c)). The output after this initial increase was very stable. Secondly, a very precise humidity sensor (courtesy of DESY MKK) was placed in two positions inside the enclosure. The first position was directly in the path of the THz propagation where it was very likely to be purged well and important to measure. The second position was in a lower corner of the enclosure where it was more difficult to purge, but less important. In both cases within less than 10 minutes the RH was confirmed to drop essentially to 0 (Fig. 6.11(b)). This confirms the functionality of the enclosure and means that the increase of 43% is a calibration of the absorption in the detection setup (only at this frequency).

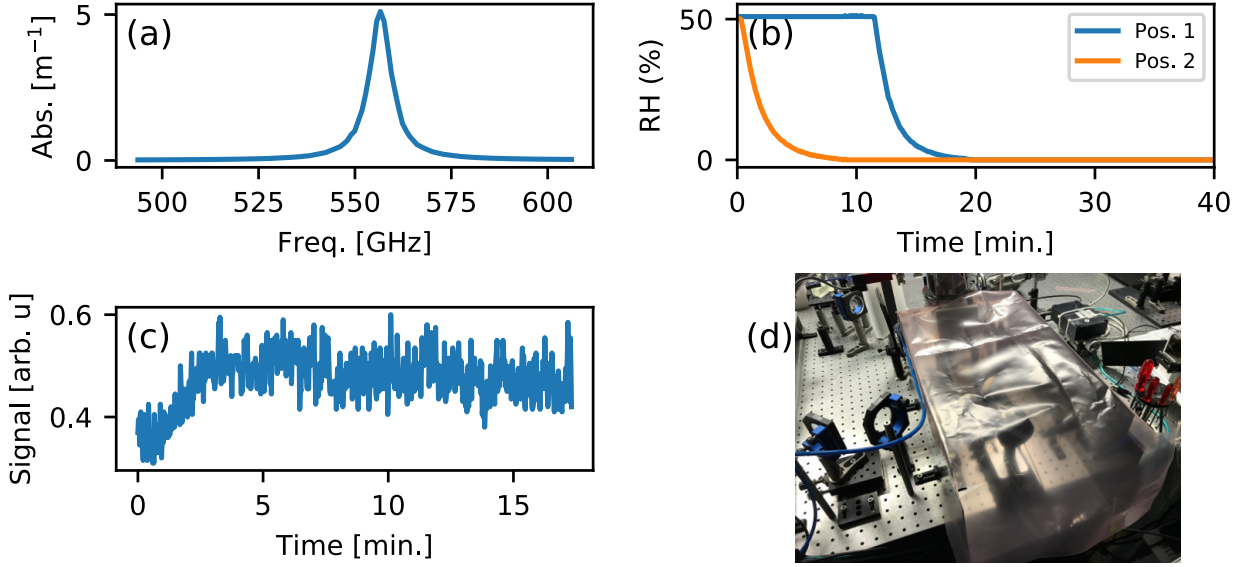


Figure 6.11: The absorption as a function of frequency **(a)** at 50 % RH taken directly from [147], the confirmation of the decrease in RH within the enclosure **(b)** at two measurement positions, the increase of THz output **(c)** at 558 GHz when purged, and a photo of the simple purging enclosure **(d)**.

6.3 Experimental results

The first and most important experimental step was to generate THz using the new Mach-Zehnder-like setup. This involved finding the temporal overlap, and also maintaining the relative alignment of the two arms when scanning the relative time delay. This was achieved, shown in Figure 6.12(a-b) for both the positive and negative time delay, for both crystals of 212 μm and 330 μm poling periods. This is important to note since now the delay is tunable over the whole range of delays on both side of t_0 , that THz can be generated at $+t_{\text{opt}}$ and $-t_{\text{opt}}$.

The THz generation in both crystals at expected delays confirmed that the new setup was suitable, and the chirp-and-delay method was indeed still responsible for the THz generation. An important note regarding the sensitivity to angle offset, is that the THz output was measured to decrease significantly with only a sub-100 μrad pointing difference between one arm and the other, seen in Figure 6.12(c). This decrease is a simple input-output measurement, and is the combination of the phase matching, outcoupling, and detection efficiency all decreasing when the angle between beams is increased. Because of this the far-field diagnostic just before the

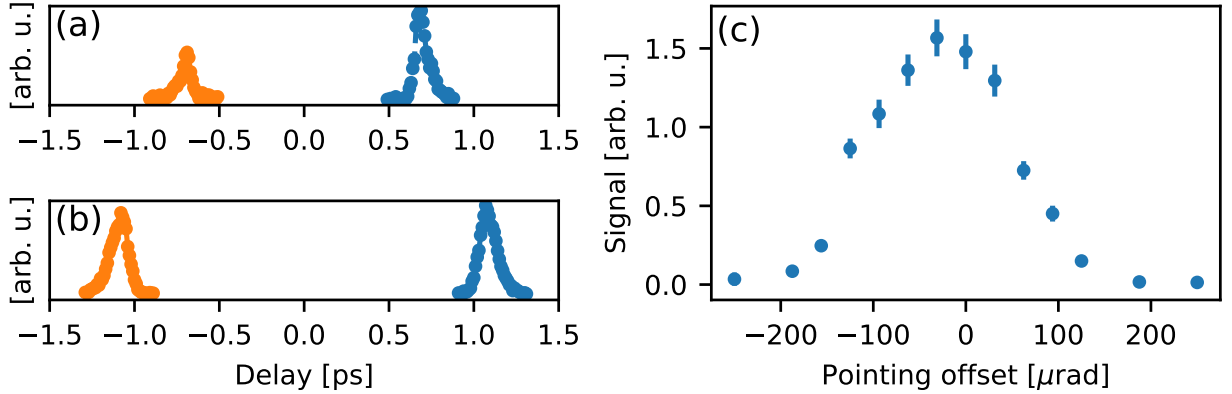


Figure 6.12: THz generated at positive (blue) and negative (orange) delays for both crystals of $330\ \mu\text{m}$ (a) and $212\ \mu\text{m}$ (b) poling periods. The fact that the optimal delays are as expected is confirmation that this is the chirp-and-delay process. The difference between the shape and magnitude of the positive and negative peaks is not clear at this point. The THz output with pointing offset between the two beams (c) was measured, enabled by the FF camera. This shows how the process is sensitive on the sub- $100\ \mu\text{rad}$ level.

input to the crystal, when both arms are colinear, was a crucial tool for day-to-day optimization and confirmation of proper alignment.

An additional confirmation was the measurement of the frequencies produced by both crystals. This was measured again using the longitudinal Michelson interferometer to measure the correlation signal and therefore the central frequency. Because these crystals are so long, these measurements are indeed all at cryogenic temperatures, so the produced frequencies must be those compared to the refractive index values at cryogenic temperatures measured in [126].

Figure 6.13(a-b) shows more than 9 cycles measured for both crystals, showing $361.65 \pm 0.1\ \text{GHz}$ (FFT gives $361.6\ \text{GHz}$ and sine fit shows $361.7\ \text{GHz}$ with negligible error) and $558 \pm 0.8\ \text{GHz}$ (FFT gives $557.4\ \text{GHz}$ and sine fit shows $558.5 \pm 0.7\ \text{GHz}$) generated by the $330\ \mu\text{m}$ and $212\ \mu\text{m}$ poling period crystals respectively. Figure 6.13(c) shows that this agrees well with the theoretically expected phase matched frequencies of $370\ \text{GHz}$ and $574\ \text{GHz}$ respectively (based on Equation 4.2 and [126]), especially considering the wide variation in reported refractive indices in the literature already mentioned, confirming also that the precision of the manufacturing is high.

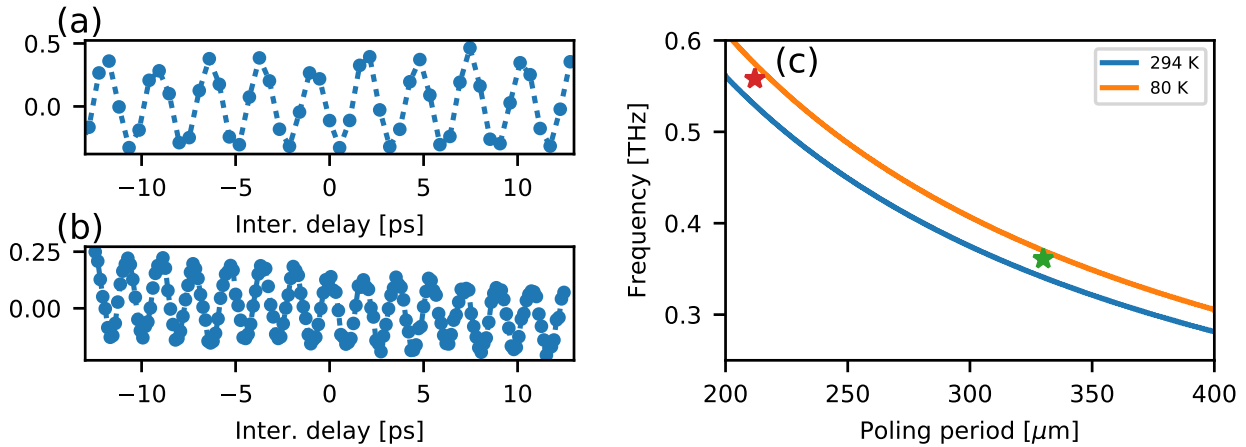


Figure 6.13: Correlation measurements for the 330 μm (a) and 212 μm (b) poling period crystals showing 361 GHz and 558 GHz central frequencies respectively. These measurements (stars) are in good agreement with theory (c) predicting 370 GHz and 574 GHz respectively.

These results together, confirmation of the chirp-and-delay in these two crystals with the Mach-Zehnder setup and measurement of the frequency, inform all of the further compensation measurements.

6.3.1 Optimization of THz energy with SF11 and TOD mirrors

The next step experimentally involved installing the SF11 prisms to attempt to optimize the THz output by adding the GDD imparted via the prisms to only one arm of the setup. As explained in a previous section, the length of SF11 that the pulses pass through depends only on the amount of overlap on the face of the prisms as long as the angle of incidence is set properly.

Therefore the prisms were installed with the angle of incidence at 60.5° and a measurement campaign with various amounts of SF11 was undertaken. In practice this was done completely for the 330 μm poling period crystal that produces 361 GHz radiation, and the afterwards for the 212 μm poling period crystal that produces 558 GHz radiation. However, to better communicate the results the steps are reported here in parallel for both crystals. The frequency generated affects all of the mechanism for compensation, so presenting them in parallel allows for showing this along with confirming that the compensation is indeed of the nature thought.

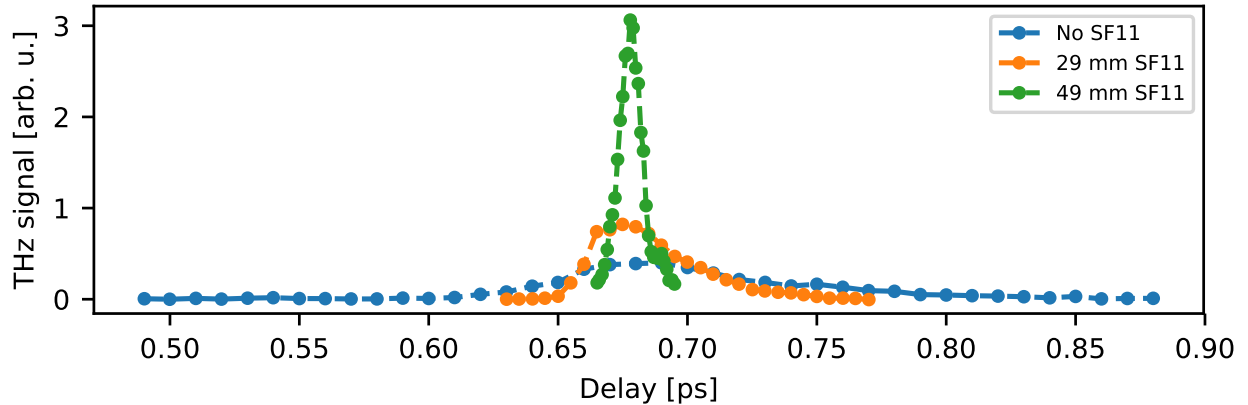


Figure 6.14: Example of three delays scans producing 361 GHz THz under the same experimental conditions with one beam propagating through various amounts of SF11. The width of the delay scans decreases and the output THz signal increases accordingly.

Shown first is the change in the delay scan nature as more SF11 is added in the one arm. This is shown in Figure 6.14 for 361 GHz and Figure 6.15 for 558 GHz. In both cases the delay scans become more narrow and the output increases. The narrowing is a result of the fact that the difference frequency is now changing less over time, so there are fewer delays where any of the difference frequency content is phase matched. The increase in output of course is a positive measurement of the beginning of compensation for the TOD.

As expected as well, the amount of SF11 needed to show a similar narrowing and increase in signal is more for the higher frequency output. This was already predicted when the asymmetric compensation method was derived (see equation 6.19).

After successfully showing the initial increase with various amounts of SF11 the compensation needed to be precisely optimized. This means measuring the output with many SF11 positions with similar experimental conditions. The results from this can be seen in the blue curves in Figure 6.16(a) and (c) without the TOD mirrors added. The optimum amount of SF11 for the 361 GHz radiation was 49 mm corresponding to 9200 fs^2 of GDD, which is very close to the predicted amount. The optimum amount of SF11 for 558 GHz radiation was 69 mm corresponding to 13000 fs^2 of GDD.

The next natural experimental step was to add the TOD mirrors in the arm where

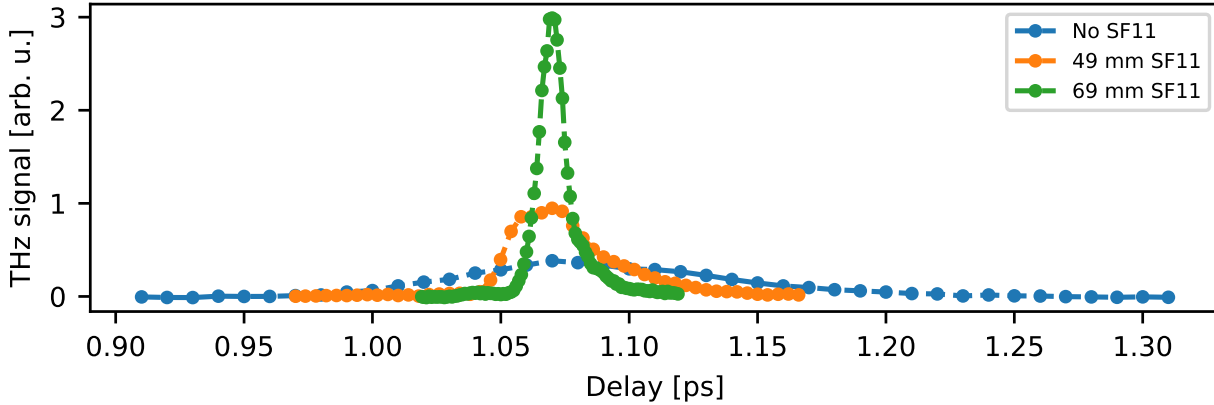


Figure 6.15: Example of three delays scans producing 558 GHz THz under the same experimental conditions with one beam propagating through various amounts of SF11. The behavior is the same as with the other crystal. The width of the scans decreases and the output increases.

there is no SF11 and reach a higher THz output. The first simple step as to do this only at the optimum amount of SF11 already found without TOD mirrors, but in the end finding the precise optimum required again scanning the amount of SF11 with varying numbers of TOD mirrors. The result of this with 0, 1, and 2 TOD mirrors (0, +20000, and +40000 fs³) is shown for the 361 GHz output in Figure 6.16(a) and for 0, 1, 2, and 3 TOD mirrors (0, +20000, +40000, and +60000 fs³) for the 558 GHz output in Figure 6.16(c). The optimum output found was 47.3 mm SF11 (8870 fs²) and 1 TOD mirror (20000 fs³) for the 361 GHz output, and 69 mm SF11 (13000 fs²) and 3 TOD mirrors (60000 fs³) for the 558 GHz output. Note that the global optimum with 1 TOD mirror has a different amount of SF11 for the 361 GHz output than the local optimum without any TOD mirrors. If there were TOD mirrors with less than 20000 fs³ per reflection available it may have been possible to fine-tune and find the optimum more precisely, especially for the 361 GHz case.

Figure 6.16(b) and (d) shows THz output dependent on added TOD (number of TOD mirrors) for the 361 GHz and 558 GHz outputs respectively. This shows very clearly that only when the GDD compensation from the SF11 is at the correct position will the addition of TOD reach a global optimum. This confirms why the experimental step of scanning the amount of SF11 again with varying number of TOD mirrors was necessary. When there is no SF11 the addition of TOD mirrors has a very minor or negligible effect.

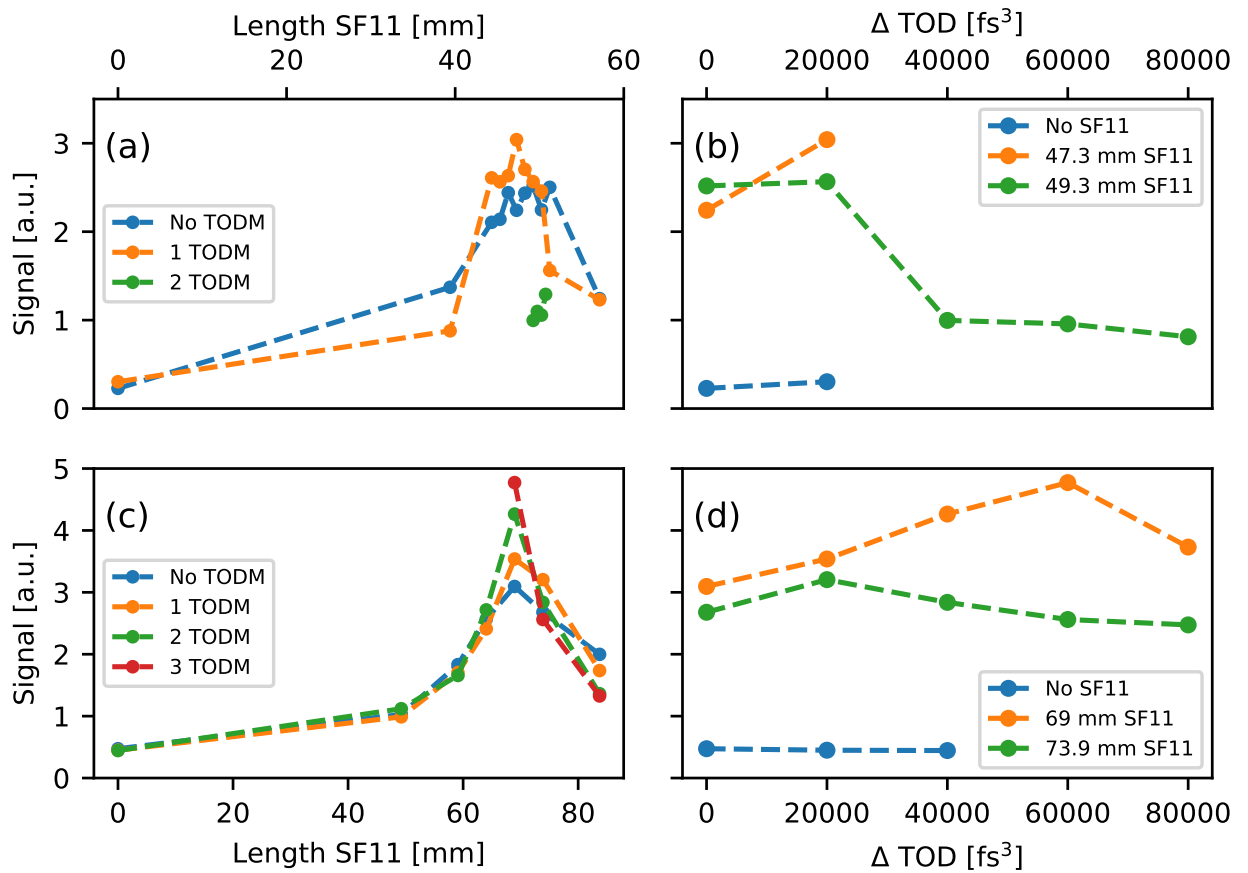


Figure 6.16: The summary of the full compensation with SF11 and TOD mirrors for both crystals. Full scans of SF11 length for the 361 GHz output with zero TOD mirrors and one TOD mirror (a), and the output with varying amounts of TOD added for no SF11 and two set amounts of SF11 (b). The same for the 558 GHz output in (c) and (d). The global optimum at 361 GHz is 47 mm SF11 and one TOD mirror, and the global optimum at 558 GHz is 69 mm SF11 and three TOD mirrors.

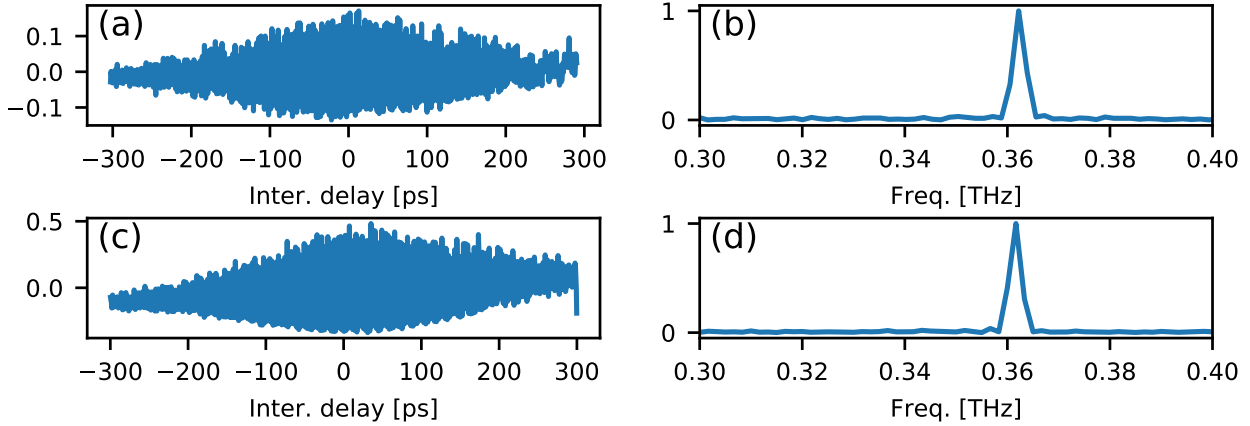


Figure 6.17: Two full-pulse interferometer scans of the 361 GHz output when there is no compensation (**a-b**) and with 49 mm SF11 (**c-d**), which is almost ideal GDD compensation. This shows that both the central frequency and the narrowband nature does not differ with or without compensation (compare **(b)** and **(d)**).

As mentioned before, the frequency was only measured in the compensated case for the 558 GHz output. However, the 361 GHz had a high enough output without compensation to allow for measurement in both cases. Figure 6.17 shows the frequency measurement without compensation (a) and with compensation (b). These results both show the same result of 361 GHz central frequency output with $<1\%$ FWHM bandwidth. This is a confirmation that both the central frequency and narrowband nature do not change with compensation. It must be noted that since the frequency measurement is essentially a correlation of the THz pulse in time, that more detailed temporal qualities cannot be measured. Therefore it may be that there are subtle differences between the uncompensated and compensated cases that cannot be seen.

Returning back to the nature of the delay scans, there are also interesting results in the delay scans at a fixed amount of SF11, while varying only the number of TOD mirrors (these are the results shown in Fig. 6.16(b,d)). What is already known is the increase in the peak THz output at the optimum temporal delay. What occurs additionally in both the 361 GHz case (Fig. 6.18) and the 558 GHz case (Fig. 6.19) is that the optimum delay decreases linearly as more TOD mirrors are added. Because these scans were done in exactly the same experimental conditions and only required exchanging mirrors (with referenced front surfaces

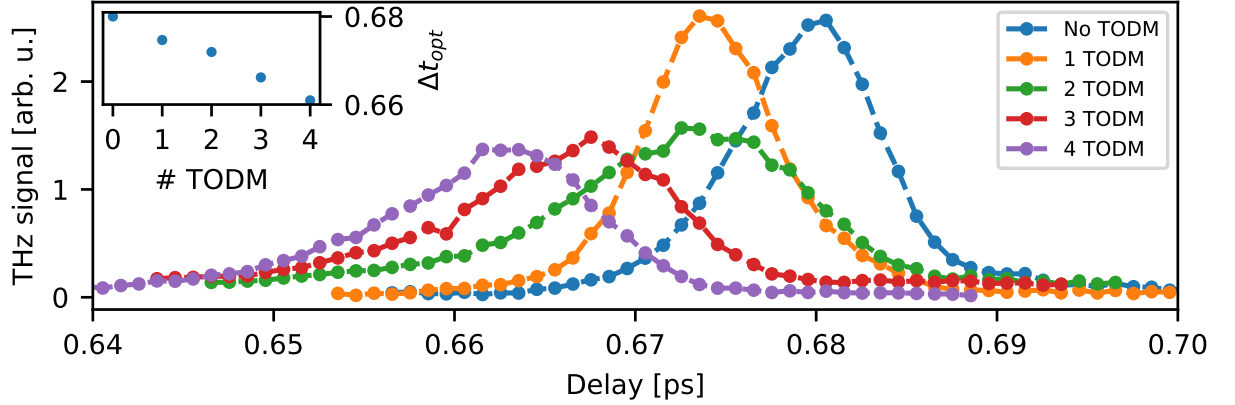


Figure 6.18: Delays scans when generating 361 GHz radiation with 49 mm SF11 in one arm and a varying amount of TOD mirrors (20000 fs³ per mirror) in the other arm. The output changes as TOD mirrors are added, with t_{opt} decreasing almost linearly (shown in the inset). Notice that the skew of the delay curves is approximately minimum with 1 TOD mirror, the scenario with also the most output.

and FF alignment), this result is valid.

At first this was unexpected, but a closer look at equation 6.19 reveals that as TOD is added to a pulse ($\phi_3^{(2)}$) the delay should change linearly. Therefore this is an interesting, and nuanced confirmation that the compensation is indeed the derived and predicted mechanism.

An additional, even more nuanced conclusion from the delay scans at both frequencies is the shape of the delay curves. As TOD mirrors are added and the output approaches the maximum, the skew (essentially the symmetry) of the delay curves decreases. In the case of the 361 GHz crystal, as the TOD mirrors are added beyond the optimum the skew becomes opposite of the initial skew. What can be seen is that at the optimum the delay scans are the most symmetric. This is an indirect confirmation that the difference frequency at this global optimum is flat in time, since there is not more THz generated at delays above or below the optimal delay.

In this section the successful compensation of the TOD present in the ANGUS pump pulses via asymmetric GDD and TOD compensation in a Mach-Zehnder-like setup was shown. All of these results shown were at extremely modest pump fluence, so that there was no risk to any optics, especially the crystals. To finally increase the output energy, pumping at high

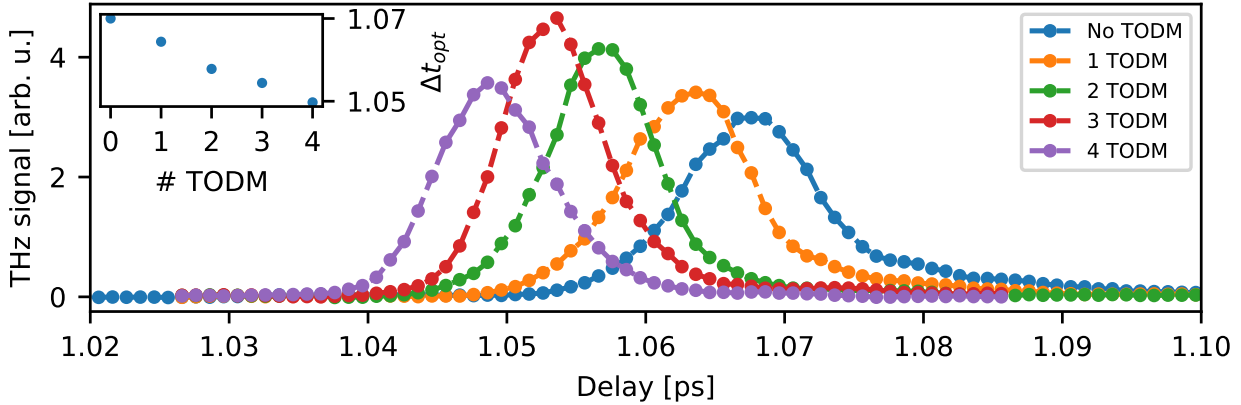


Figure 6.19: Delays scans when generating 558 GHz radiation with 69 mm SF11 in one arm and a varying amount of TOD mirrors (20000 fs³ per mirror) in the other arm. The change is the same as with the other crystal, with t_{opt} decreasing almost linearly (shown in the inset). The skew of the delay curves is approximately minimum with 3 TOD mirrors, the scenario with also the most output.

fluence is necessary.

6.3.2 High energy THz pulses from a single crystal

The pumping of the two crystals at higher fluence requires operating the ANGUS Amp1 with all three pump lasers. The potential, since there are some transport losses and half of the energy is dumped in the Mach-Zehnder, is up to 500-600 mJ on one crystal. The input energy was increased up to 381 mJ input (293 mJ/cm² fluence) on the 330 μ m poling period crystal producing up to a peak energy of 400 μ J THz pulses at 361 GHz (Fig. 6.20(a)). A 100 μ m fused silica output coupler was installed on the rear surface with the front surface AR coated for the pump wavelength, but the output coupler only marginally increased the output by \sim 10%. Unfortunately at this fluence point a TOD mirror damaged, and a black veil due to vacuum chamber cleanliness and laser-induced condensation appeared on the rear face of the PPLN crystal. The veil disappeared after the crystal was warmed up still under vacuum, but the TOD mirror damage was catastrophic. The output THz energy decreased over time as this damage worsened.

These energy levels are a great success, showing the ability of this compensation method

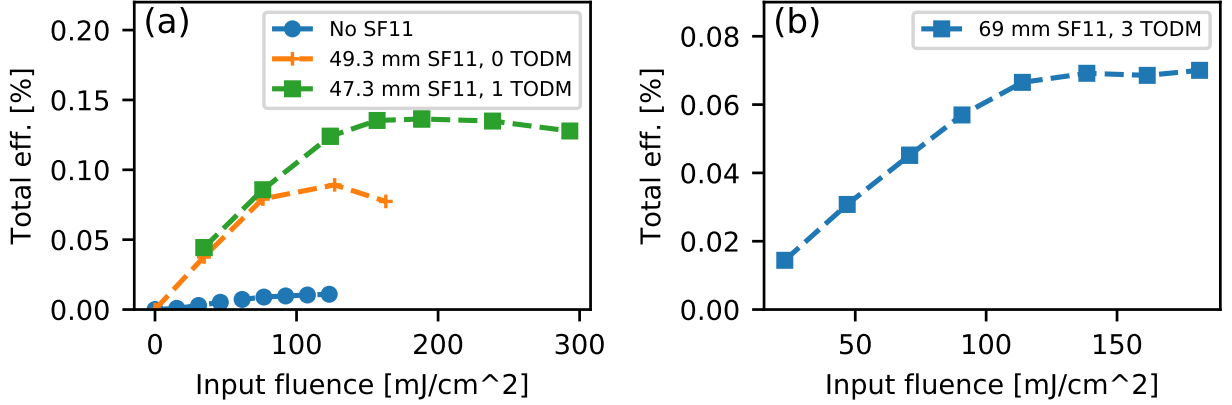


Figure 6.20: High energy output at 361 GHz (a) showing total efficiencies up to 0.13% when pumped at 293 mJ/cm² producing up to 400 μ J THz energy. The highest output at 558 GHz (b) was 128 μ J.

to work at high fluence. Also, it seems preliminarily that the compensation also increases the fluence level at which saturation of the efficiency begins.

The 212 μ m poling period crystal was pumped up to 181 mJ/cm² producing up to a peak energy of 128 μ J THz pulses at 558 GHz (Fig. 6.20(b)). This was without any NIR AR coating or output coupler. The efficiency saturated quite early, and the output was already lower than in the 360 GHz case, so risk was not taken at a higher fluence. This lower output is due to the significantly higher absorption at these higher frequencies, even at cryogenic temperatures [126]. This is a record at this frequency as well.

Still, despite these great results, the total efficiencies are well below the 1% mark. To attempt to assess this discrepancy, the so-called "intrinsic efficiency" is important to consider, which can be analyzed from the output IR spectrum. As the spectrum red-shifts more and more as the pumping fluence is increased, the center-of-mass shift represents how much of the NIR energy is involved in the cascading nonlinear process. This represents what is called the intrinsic efficiency

$$\eta_{\text{intrinsic}} = \frac{\bar{\nu}_{\text{in}}^{\text{IR}} - \bar{\nu}_{\text{out}}^{\text{IR}}}{\bar{\nu}_{\text{in}}^{\text{IR}}}, \quad (6.29)$$

that represents the maximum possible percentage of the input IR energy that could be

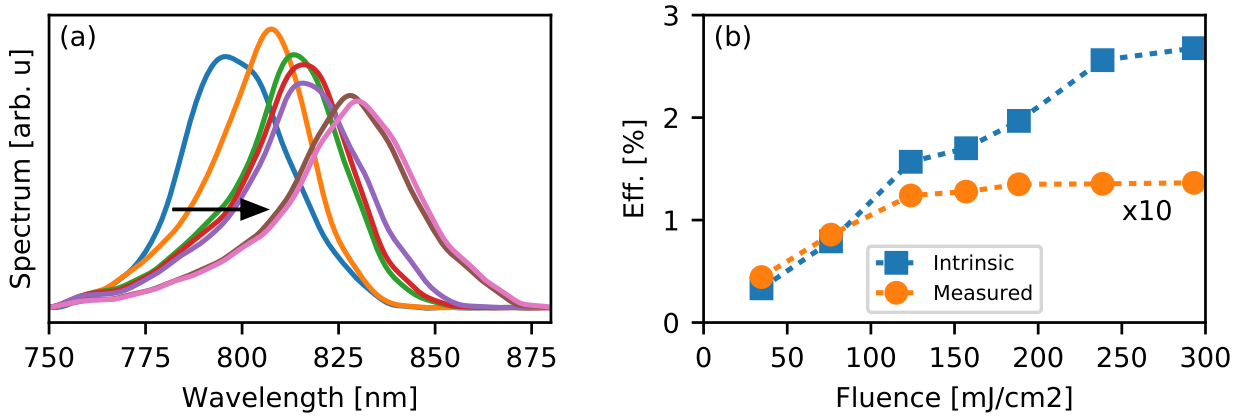


Figure 6.21: Normalized and filtered output spectra (a) at all fluence levels shown in Figure 6.20(a) with full compensation for the 361 GHz output (arrow shows increasing fluence). Note the extreme redshift as fluence increases. When plotting the intrinsic efficiency compared with the measured efficiency (b) it can be shown that the intrinsic efficiency based on the measured spectra does not saturate, while the measured efficiency does.

converted to the produced nonlinear energy, in this case THz. It can be shown that $\eta_{\text{intrinsic}} \propto 1/\bar{\lambda}_{\text{out}}^{\text{IR}}$ so the analysis is quite simple. If there were no absorption, scattering, etc. then the measured experimental efficiency should be close to this intrinsic value calculated from the IR output spectra. However, in the case of the 361 GHz output (Fig. 6.21) and the 558 GHz output (Fig. 6.22) the intrinsic efficiency is approximately 10 and 20 times larger respectively, and in both cases the intrinsic efficiency does not saturate, but the measured efficiency does. Part of the explanation that the 558 GHz discrepancy is larger is the fact that the crystal was not AR-coated for NIR on the front surface, nor was any THz AR wafer attempted on the rear surface at this frequency (since an even thinner wafer would be needed). The intrinsic efficiency can only properly represent the efficiency within the crystal, which is more suitable for the 361 GHz case where there are AR coating installed. In any case, the difference is at minimum a factor of 10.

The conclusion from this is that the absorption even at the cryogenic temperatures is playing a large role. Therefore it is possible that decreasing the crystal length from 36 mm may be advantageous, as long as it is acceptable for applications to have fewer total cycles. An unresolved conclusion is why there is saturation in the measured THz output energy, and if it

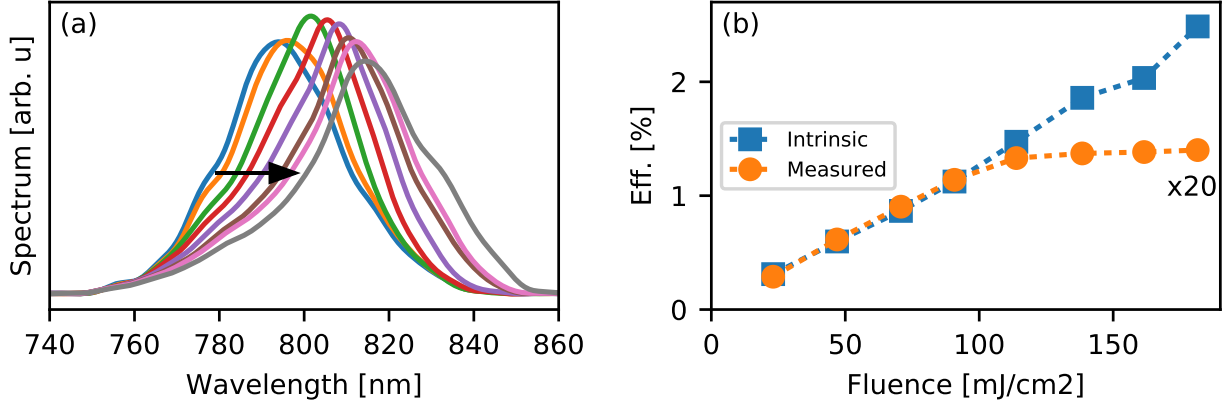


Figure 6.22: Normalized and filtered output spectra (a) at all fluence levels shown in Figure 6.20(b) with full compensation for the 558 GHz output (arrow shows increasing fluence). There is again extreme redshift as fluence increases and the intrinsic efficiency compared with the measured efficiency (b) has the same difference, even more clear in this case.

is possible to mitigate that.

6.3.3 Generation of high-energy THz pulses in two crystals simultaneously

The Mach-Zehnder setup produces two IR outputs with equal energy and identical temporal properties. Therefore, with two identical crystals THz could be produced in two crystals simultaneously. Because the THz energy was clearly higher with the 361 GHz output, the production of THz with two crystals in tandem was pursued with only these crystals: Two crystals with $330\ \mu\text{m}$ poling period and 36 mm length, produced using identical poling masks in the lab of Prof. T. Taira [130].

The experimental setup, seen in Figure 6.23, is the natural extension of the setup in the previous sections, with the addition of a second independent vacuum chamber and cryogenic dewar, half-wave plate, and teflon block to dump the IR. The crystal used in the previous section with an NIR-AR coating on the front and rear surface and an installed $100\ \mu\text{m}$ fused silica plate on the rear surface is left unchanged for these results and is referred to as crystal 1. The second crystal has not coating and no wafer is referred to as crystal 2. The detection setup, consisting of one TPX lens with 150 mm focal length and the THz pyro-electric detector was made to be quickly movable to detect THz from crystal 1 and crystal 2 identically.

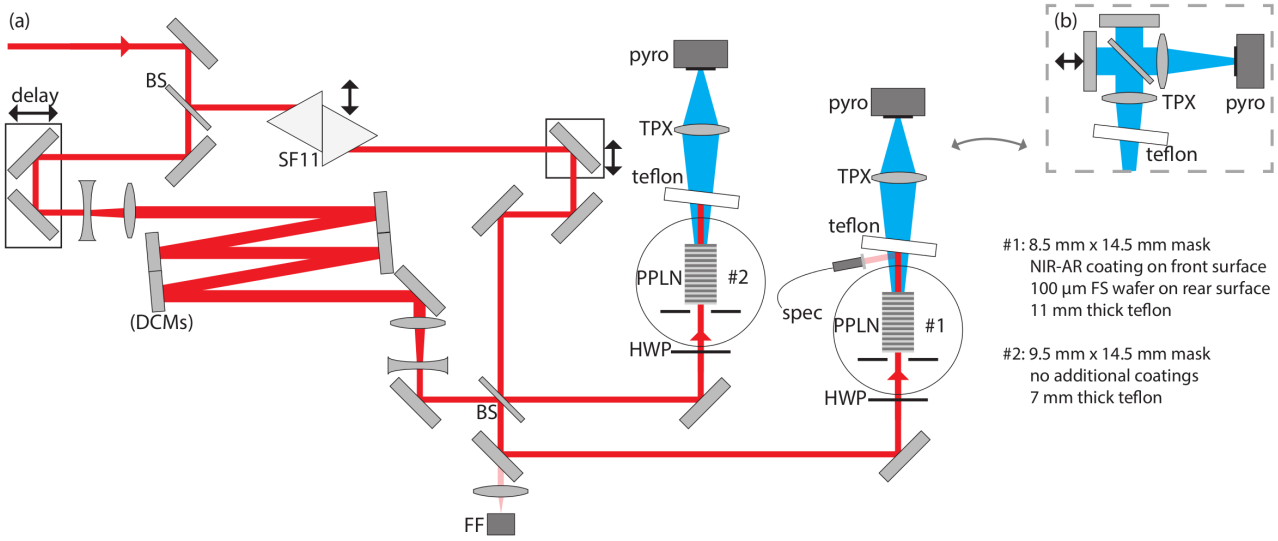


Figure 6.23: A diagram of the experimental setup for asymmetric compensation with two crystals **(a)** with the longitudinal interferometer (correlator) used for frequency measurement **(b)**. Additionally, there were two identical telescopes added in one arm to attempt to avoid the damage experienced on the high-TOD mirrors. **Key:** BS: beamsplitter; DCMs: dispersion compensating mirrors; BB: beam block; FF: farfield camera; spec: optical spectrometer; pyro: pyro-electric detector.

In addition to the second dewar, two identical telescopes were installed in the arm with high-TOD mirrors in order to increase the beamsize on the TOD mirrors to avoid damage in that section. The telescopes are made up of two pairs of identical N-BK7 lenses with -150 mm and $+300$ mm focal lengths, with a total path length of 18.2 mm in both telescopes combined. Because of this additional path length in a material, and the non-negligible GVD of 45 fs²/mm for N-BK7 at 800 nm wavelength [141], there is an added dispersion of roughly 819 fs² in the arm with the high-TOD mirrors. This essentially shifts the maximum output compared to the previous results without the telescopes. Therefore, the new optimum $\Delta\phi_2$ in the prism arm is $8870+819=9689$ fs², which corresponds to 51.7 mm SF11. Therefore, the experiments with two crystals are done only with 51.7 mm SF11.

The first proof of the viability of using two crystals simultaneously is to show that the crystals produce THz at identical temporal delays, since each output of the Mach-Zehnder setup is constrained to have both the same temporal properties in each of the two overlapped pulses, but also the same temporal delay between the pulses. This was shown at a low fluence

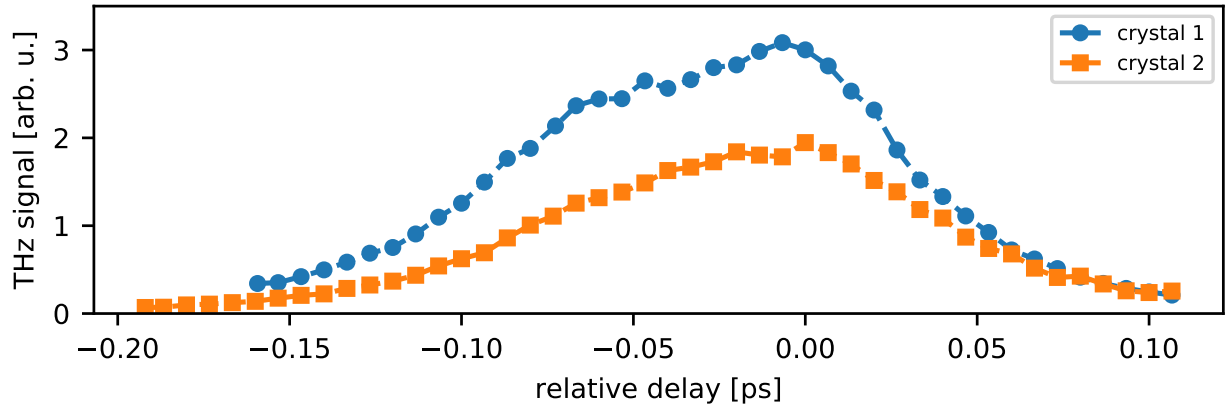


Figure 6.24: Delay scans showing the peak in THz output at the exact same delay for both crystals.

with crystal 1 cooled to 86 K and crystal 2 cooled to 92 K. As shown in Figure 6.24, the peak THz output is at an identical temporal delay in each crystal. This is both a confirmation that the outputs of the setup indeed do have identical properties, and that the two crystals were manufactured with high precision.

Using the positive result that the peak THz was produced at the same temporal delay, the input into the crystals was increased to a high fluence to increase the total output THz energy. Each crystal was pumped with up to a total IR energy of 519 mJ, a total of more than 1 J out of the Mach-Zehnder setup, which corresponds to a fluence of 400 mJ/cm² on each crystal.

The first positive results of these high fluence measurements is that with the inclusion of the two telescopes in the arm containing the high-TOD mirrors there was no optical damage. Previously the crystals were pumped only successfully up to 381 mJ and experienced damage at that step. Therefore this is already a successful improvement to the setup.

When pumping to this fluence the single-crystal output energy was increased to a peak value of 458 μ J, and an average of 392 μ J from crystal 1. This is an increase of about 15% compared to the previous results, due to the fact that the crystals could now be pumped at a higher fluence without damage. Additionally, in crystal 2 a peak energy of 232 μ J and an average output of 212 μ J were reached. Therefore from both crystals simultaneously 1 J of

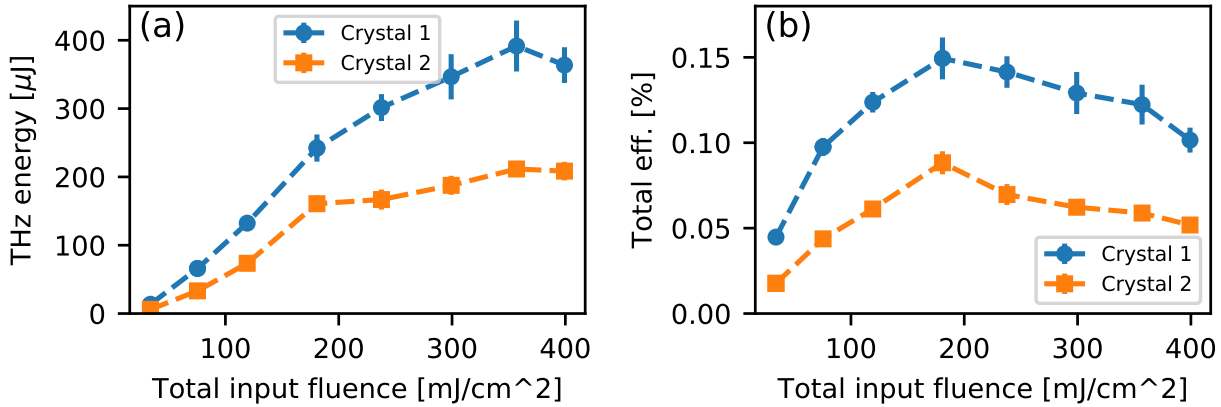


Figure 6.25: THz output simultaneously with increasing pump fluence for both 330 μm poling period crystals of 36 mm length.

pump energy produced an average output of 604 μJ at 361 GHz.

What is important to note, as can be seen in Figure 6.25, is that although the increased fluence improved the total achieved output from crystal 1, this was not true with each step up in fluence. The last increase in pump fluence from 357 mJ/cm^2 to 399 mJ/cm^2 saw a decrease not only in efficiency, but also in the output THz energy. The efficiency had already saturated, with the peak efficiency of 0.149% at a fluence of 181 mJ/cm^2 , but the decrease in output THz energy means that beyond a fluence of 357 mJ/cm^2 the efficiency is quickly decreasing. Therefore, although it was potentially possible to increase the fluence by one more additional step using all of the available laser energy, this would have had only a negative effect on the output energy with an increased risk of optical damage.

The qualitative behavior is quite similar in crystal 2, of both the peak in efficiency at 181 mJ/cm^2 pump fluence and the eventual decrease in output THz energy above 357 mJ/cm^2 pump fluence, with only a lower total output. The lower output is due to the lack of the NIR-AR coating on the front surface, which decreases the actual input IR energy in the crystal to 85% of that in crystal 1. The AR coating on crystal 1 warps significantly when cooled to cryo-temperatures and is therefore at present not a viable solution long-term, if the IR pump were to be re-used after the interaction. Also, the lack of an installed wafer at the rear surface decreased the THz outcoupling at the rear surface slightly. However, the wafer installed on crystal 1 was

still only measured to increase output by $\sim 10\%$ and is therefore not yet performing up to the theoretical level.

6.4 Outlook

This chapter showed an exploration of possible methods to compensate for the TOD present on the NIR pump pulses, a derivation of the validity of using either a de-tuned grating compressor or asymmetrically tuning the phase of the pulses, and an experimental verification of the asymmetric tuning method. This resulted in an increase of 8 times of the output efficiency and in the case of the 361 GHz output THz pulses up to $458\ \mu\text{J}$ in peak energy from a single crystal, and a combined average output of $604\ \mu\text{J}$ produced in two crystals in tandem.

As just explained, the efficiencies are still only on the 0.1% level, and there are possibilities to improve this further. The most important of these is improving the performance of the output coupler to the theoretically predicted level. This is more-so an engineering challenge, to ensure that micron-scale distortions do not occur in the thin wafers when cryo-cooling. The THz pulses produced in tandem in the two crystals could also be combined coherently to have the total energy in one pulse, since this is relatively easy with the 1 mm-scale wavelengths of THz radiation. However, the combination process likely has small losses, and nicely transporting the spatial modes of these long-wavelength beams is challenging.

There are also less obvious steps forward. For example, the discrepancy between the intrinsic efficiency and the measured efficiency means that there is either an unavoidably large effect of absorption, that the crystal should be cooled to even lower temperatures, that the crystal length is not optimum, or that the frequency is not optimum. All of these could be experimentally explored, except for the fact that crystals of these apertures are not available on short-notice and are not available in any frequencies outside the current range at all.

Lastly, the issue of the saturation of the efficiency may be mitigated by approaching perfect compensation. It could be that with more finely spaced TOD mirrors, or a set or perfectly designed general chirped mirrors, or with a DAZZLER in one arm of the setup, a very precise optimum could be found that does not necessarily increase the efficiency at low fluence, but maybe completely eliminates efficiency saturation or at least delays it until a

higher fluence. This would allow for even more THz energy output at the high fluences already explored. However, this is only a potential result that has no strong proof so far. And indeed, in all high-fluence results with both 361 GHz and 558 GHz crystals the efficiency began saturating (i.e. increasing more slowly than linear) above 100 mJ/cm^2 pump fluence.

These near-term methods provide a realistic road-map towards breaking and surpassing 1 mJ of narrowband THz. Besides the clear implications for high energy THz production when quasi-phase-matched in PPLN, the successful compensation for the TOD could also have implications for the production of ultra-narrowband THz pulses at higher frequencies in other materials. Analysis showed that when TOD is present and the pump pulses are optimized for higher frequencies (for example ~ 7 THz in GaP) then the produced THz is broader bandwidth, but has a significant chirp. The compensation method shown experimentally in this chapter would be equally applicable to removing the chirp from THz pulses produced in direct-phase matched DFG in thin crystals — albeit with significantly more propagation needed within SF11 — which with ANGUS pump pulse parameters could produce sub-0.1% bandwidth THz. The same arguments for being able to pump harder due to the fact that the pump pulses are heavily chirped would also apply in this case, potentially pushing the limits of narrowband THz pulse energies at these frequencies as well.

Chapter 7

Conclusion

This work has outlined in general the ANGUS laser system and its integration into controls systems on the DESY campus, increasing vastly the reliability and availability of the high-power system. This progress has allowed the system to be used reliably for its main purpose of laser-plasma acceleration [22], but also for use in the THz generation experiments outlined in the rest of the work.

A very high pulse energy of THz radiation is crucial for acceleration or manipulation of particles in specially designed waveguides [13, 21]. In addition to the high pulse energy, the radiation must be phase-matched to the relativistic electrons being accelerated. Because the phase matching conditions in such waveguides are not broadband the THz must be narrowband to couple efficiently to the desired mode. For that application, among others, this work focused on the generation of THz in periodically-poled lithium niobate (PPLN) using copies of ANGUS pulses.

The first results reported include a verification of this so-called chirp-and-delay method, where it is shown that the optimum temporal delay Δt_{opt} for crystals of four different poling periods (400 μm , 330 μm , 212 μm and 125 μm) — corresponding to four different frequencies 0.275 THz, 0.361 THz, 0.544 THz, and 0.867 THz respectively — was linearly proportional to the generated frequency. This is predicted by the simplest explanation of the mechanism that $t_{\text{opt}} = \Omega\phi_2$ where Ω is the THz angular frequency and ϕ_2 is the GDD of the ANGUS pulses. Both 10 mm and 20 mm long crystals with 212 μm poling period were pumped at higher fluence, at both 294 K and 82 K, showing dramatic increase when cooled to 82 K. With the shorter crystal the highest output energy of 40 μJ was achieved and with the longer crystal the highest internal efficiency was measured up to 0.13 %. The discrepancy is due to the fact that the longer crystal has a smaller input aperture and in the experiments had a lower damage threshold than the shorter crystal. These initial results were reported as well in a publication in Optics Letters [85].

Although in these first results there was evidence of optical cascading, a signature and confirmation of high efficiency, the absolute efficiency values were significantly below those predicted by numerical simulations. Based on a detailed analysis it could be found that the third-order dispersion (TOD) inherent to the ANGUS pulses was directly responsible for this. A detailed analysis of the expected pulses properties of the stretched IR pulses produced a simple relation for the temporal phase (rather than the spectral phase), which could be used to match experimental data in multiple ways. This confirms that the TOD was indeed a significant effect on the initial chirp-and-delay results. The effect relevant for the quasi-phase-matched experiments in PPLN is a reduction in efficiency. Additionally, it was shown that for direct phase matched experiments with thin crystals the TOD on the pump pulses would result in a significant chirp on the THz pulses. Without the TOD in the thin-crystal case the bandwidth may be extremely narrow, motivating additionally a proven method to compensate for the TOD.

Of course the next step was to experimentally compensate for this TOD, but due to the large magnitude it was argued that single-component-level solutions are not possible to remove a significant percentage of the TOD, and that only more complicated solutions are sufficient. One proposed is a de-tuned grating compressor, but due to complexity and the possible further limitation of pump fluence an alternative method of asymmetric compensation was theoretically described and experimentally implemented.

This asymmetric compensation method used a Mach-Zehnder style setup and the combination of SF11 glass (with relatively high dispersion) and high-TOD dispersion compensating mirrors to independently manipulate the phase of each optical pulse copy. This method was shown to work for two different crystals of large aperture, increasing efficiency by a factor of 8 and resulting in pulses with an energy up to a maximum of $400 \mu\text{J}$ at 361 GHz (with $<1\%$ bandwidth) and $128 \mu\text{J}$ at 558 GHz. With some indirect arguments it was reasoned that the length of these crystals, 36 mm, may actually be too large, and that there may be possible further optimization. However, THz pulses of these energies at such narrow bandwidth pushes the boundaries of what is possible in the 0.1–1 THz frequency range, opening up a world of possibilities.

Bibliography

- [1] “Future Circular Collider Study,” <https://fcc.web.cern.ch/>.
- [2] “Linear Collider Collaboration,” <https://www.linearcollider.org/>.
- [3] H. Franz, O. Leupold, R. Röhlsberger, S. Roth, O. Seeck, J. Spengler, J. Stremper, M. Tischer, J. Viefhaus, E. Weckert, and T. Wroblewski, “Technical report: PETRA III: DESY’s new high brilliance third generation synchrotron radiation source,” *Synchrotron Radiation News* **19**, 25–29 (2006).
- [4] P. Emma, R. Akre, J. Arthur, R. Bionta, C. Bostedt, J. Bozek, A. Brachmann, P. Bucksbaum, R. Coffee, F.-J. Decker, Y. Ding, D. Dowell, S. Edstrom, A. Fisher, J. Frisch, S. Gilevich, J. Hastings, G. Hays, P. Hering, Z. Huang, R. Iverson, H. Loos, M. Messerschmidt, A. Miahnahri, S. Moeller, H.-D. Nuhn, G. Pile, D. Ratner, J. Rzepiela, D. Schultz, T. Smith, P. Stefan, H. Tompkins, J. Turner, J. Welch, W. White, J. Wu, G. Yocky, and J. Galayda, “First lasing and operation of an angstrom-wavelength free-electron laser,” *Nature Photonics* **4**, 641–647 (2010).
- [5] H. Chapman, A. Barty, M. Bogan, S. Boutet, M. Frank, S. Hau-Riege, S. Marchesini, B. Woods, S. Bajt, W. Benner, R. London, E. Plönjes, M. Kuhlmann, R. Treusch, S. Düsterer, T. Tschentscher, J. Schneider, E. Spiller, T. Möller, C. Bostedt, M. Hoener, D. Shapiro, K. Hodgson, D. van der Spoel, F. Burmeister, M. Bergh, C. Caleman, G. Huldt, M. Seibert, F. Maia, R. Lee, A. Szöke, N. Timneanu, and J. Hajdu, “Femtosecond diffractive imaging with a soft-X-ray free-electron laser,” *Nature Physics* **2**, 839–843 (2006).
- [6] L. Young, E. Kanter, B. Krässig, Y. Li, A. M. March, S. T. Pratt, R. Santra, S. Southworth, N. Rohringer, L. DiMauro, G. Doumy, C. Roedig, N. Berrah, L. Fang, M. Hoener, P. Bucksbaum, J. Cryan, S. Ghimire, J. Glowia, D. Reis, J. Bozek, C. Bostedt, and

M. Messerschmidt, “Femtosecond electronic response of atoms to ultra-intense X-rays,” *Nature* **466**, 56–62 (2010).

- [7] “FELIX lab,” <http://www.ru.nl/felixelix/>.
- [8] “FEL at jefferson lab,” <http://www.jlab.org/FEL/>.
- [9] S. Mangles, C. Murphy, Z. Najmudin, A. Thomas, J. Collier, A. Dangor, E. Divall, P. Foster, J. Gallacher, C. Hooker, D. Jaroszynski, A. Langley, W. Mori, P. Norreys, F. Tsung, R. Viskup, B. Walton, and K. Krushelnick, “Monoenergetic beams of relativistic electrons from intense laser-plasma interactions,” *Nature* **431**, 535–538 (2004).
- [10] C. Geddes, C. Toth, J. van Tilborg, E. Esarey, C. Schroeder, D. Bruhwiler, C. Nieter, J. Cary, and W. Leemans, “High-quality electron beams from a laser wakefield accelerator using plasma-channel guiding,” *Nature* **431**, 538–541 (2004).
- [11] J. Faure, Y. Glinec, A. Pukhov, S. Kiselev, S. Gordienko, E. Lefebvre, J.-P. Rousseau, F. Burgy, and V. Malka, “A laser-plasma accelerator producing monoenergetic electron beams,” *Nature* **431**, 541–544 (2004).
- [12] E. Esarey, C. Schroeder, and W. Leemans, “Physics of laser-driven plasma-based electron accelerators,” *Reviews of Modern Physics* **81**, 1229–1285 (2009).
- [13] L. Wong, A. Fallahi, and F. Kärtner, “Compact electron acceleration and bunch compression in THz waveguides,” *Optics Express* **21**, 9792–9806 (2013).
- [14] E. A. Nanni, W. R. Huang, K.-H. Hong, K. Ravi, A. Fallahi, G. MoriENA, R. J. D. Miller, and F. X. Kärtner, “Terahertz-driven linear electron acceleration,” *Nature communications* **6** (2015).
- [15] F. Kärtner, F. Ahr, A.-L. Calendron, H. Çankaya, S. Carbajo, G. Chang, G. Cirimi, K. Dörner, U. Dorda, A. Fallahi, A. Hartin, M. Hemmer, R. Hobbs, Y. Hua, W. Huang, R. Letrun, N. Matlis, V. Mazalova, O. Mücke, E. Nanni, W. Putnam, K. Ravi, F. Reichert, I. Sarrou, X. Wu, A. Yahaghi, H. Ye, L. Zapata, D. Zhang, C. Zhou, R. Miller,

- K. Berggren, H. Graafsma, A. Meents, R. Assmann, H. Chapman, and P. Fromme, “AX-SIS: Exploring the frontiers in attosecond X-ray science, imaging and spectroscopy,” *Nuclear Instruments and methods in Physics Research A* **829**, 24–29 (2016).
- [16] M. Fakhari, A. Fallahi, and F. Kärtner, “THz cavities and injectors for compact electron acceleration using laser-driven thz sources,” *Physical review Accelerators and Beams* **20**, 041302 (2017).
- [17] V. Vagin and V. Kotov, “Investigation of hybrid waves in a circular waveguide partially filled with dielectric,” *Soviet Physics - Technical Physics* **10**, 987–991 (1966).
- [18] R. Kustom, C. Chang, and J. Dawson, “Dielectric loaded waveguides as particle separators,” *Nuclear Instruments and Methods* **87**, 19–27 (1970).
- [19] P. Emma, J. Frisch, and P. Krejcik, “A transverse rf deflecting structure for bunch length and phase space diagnostics,” *SLAC Linear Collider Collaboration Tech Notes* (2000).
- [20] M. Röhrs, C. Gerth, H. Schlarb, B. Schmidt, and P. Schmüser, “Time-resolved electron beam phase space tomography at a soft X-ray free-electron laser,” *Physical Review Special Topics - Accelerators and Beams* **12**, 050704 (2009).
- [21] F. Lemery, K. Flöttmann, T. Vinatier, and R. Assman, “A transverse deflection structure with dielectric-lined waveguides in the sub-THz regime,” in “proceedings of IPAC,” (2017).
- [22] N. Delbos, “High repetition rate laser-plasma accelerator: 5 hz electron beam generation and advanced target design,” Ph.D. thesis, Universität Hamburg (2017).
- [23] D. Strickland and G. Mourou, “Compression of amplified chirped optical pulses,” *Optics Communications* **56**, 219–221 (1985).
- [24] E. B. Treacy, “Compression of picosecond light pulses,” *Physics Letters* **28A**, 34–35 (1968).
- [25] R. Fork, C. B. Cruz, P. Becker, and C. Shank, “Compression of optical pulses to six femtoseconds by using cubic phase compensation,” *Optics Letters* **12**, 483–485 (1987).

- [26] S. Kane and J. Squier, “Fourth-order-dispersion limitations of aberration-free chirped-pulse amplification systems,” *Journal of the Optical Society of America B* **14**, 1237–1244 (1997).
- [27] S. Backus, C. Durfee, M. Murnane, and H. Kapteyn, “High power ultrafast lasers,” *Review of Scientific Instruments* **69**, 1207–1223 (1998).
- [28] O. Martinez, “3000 times grating compressor with positive group velocity dispersion: Application to fiber compensation in 1.3-1.6 μm region,” *IEEE Journal of Quantum Electronics* **23** (1987).
- [29] J. McMullen, “Chirped-pulse compression in strongly dispersive media,” *Journal of the Optical Society of America* **67**, 1575–1578 (1977).
- [30] H. Kim, V. Pathak, K. Pae, A. Lifschitz, F. Sylla, J. Shin, C. Hojbota, S. Lee, J. Sung, H. Lee, E. Guillaume, C. Thauray, K. Nakajima, J. Vieira, L. Silva, V. Malka, and C. Nam, “Stable multi-GeV electron accelerator driven by waveform controlled PW laser pulses,” *Scientific Reports* **7**, 10203 (2017).
- [31] A. E. Siegman, *Lasers* (University Science Books, 1986).
- [32] P. W. Milonni and J. H. Eberly, *Lasers* (John Wiley and Sons, 1988).
- [33] R. W. Boyd, *Nonlinear Optics* (Elsevier, 2008), 3rd ed.
- [34] K. Ravi, D. Schimpf, and F. Kärtner, “Pulse sequences for efficient multi-cycle terahertz generation in periodically poled lithium niobate,” *Optics Express* **24**, 5253–5276 (2016).
- [35] L. Canova, S. Kourtev, N. Minkovski, A. Jullien, R. Lopez-Martens, O. Albert, and S. Saltiel, “Efficient generation of cross-polarized femtosecond pulses in cubic crystals with holographic cut orientation,” *Applied Physics Letters* **92**, 231102 (2008).
- [36] T. Grow, A. Ishaaya, L. Vuong, A. Gaeta, N. Gavish, and G. Fibich, “Collapse dynamics of super-Gaussian beams,” *Optics Express* **14**, 5468–5475 (2006).

- [37] U. Frühling, M. Wieland, M. Gensch, T. Gebert, B. Schütte, M. Krikunova, R. Kalms, F. Budzyn, O. Grimm, J. Rossbach, E. Plönjes, and M. Drescher, “Single-shot terahertz-field-driven X-ray streak camera,” *Nature Photonics* **3**, 523–528 (2009).
- [38] P. Juranić, A. Stepanov, R. Ischebeck, V. Schlott, C. Pradervand, L. Patthey, M. Radović, I. Gorgisyan, L. Rivkin, C. Hauri, B. Monoszalai, R. Ivanov, P. Peier, J. Liu, T. Togashi, S. Owada, K. Ogawa, T. Katayama, M. Yabashi, and R. Abela, “High-precision x-ray FEL pulse arrival time measurements at SACLA by a THz streak camera with Xe clusters,” *Optics Express* **22**, 30004–30012 (2014).
- [39] I. Gorgisyan, R. Ischebeck, C. Erny, A. Dax, L. Patthey, C. Pradervand, L. Sala, C. Milne, H. Lemke, C. Hauri, T. Katayama, S. Owada, M. Yabashi, T. Togashi, R. Abela, L. Rivkin, and P. Juranić, “THz streak camera method for synchronous arrival time measurement of two-color hard X-ray FEL pulses,” *Optics Express* **25**, 2080–2091 (2017).
- [40] I. Grguraš, A. Maier, C. Behrens, T. Mazza, T. Kelly, P. Radcliffe, S. Düsterer, A. Kazan-sky, N. Kabachnik, T. Tschentscher, J. Costello, M. Meyer, M. Hoffmann, H. Schlarb, and A. Cavalieri, “Ultrafast X-ray pulse characterization at free-electron lasers,” *Nature Photonics* **6**, 852–857 (2012).
- [41] W. Helml, A. Maier, W. Schweinberger, I. Grguraš, P. Radcliffe, G. Doumy, C. Roedig, J. Gagnon, M. Messerschmidt, S. Schorb, C. Bostedt, F. Grüner, L. DiMauro, D. Cubaynes, J. Bozek, T. Tschentscher, J. Costello, M. Meyer, R. Coffee, S. Düsterer, A. Cavalieri, and R. Kienberger, “Measuring the temporal structure of few-femtosecond free-electron laser X-ray pulses directly in the time domain,” *Nature Photonics* **8**, 950–957 (2014).
- [42] A. Stepanov, J. Hebling, and J. Kuhl, “Efficient generation of subpicosecond terahertz radiation by phase-matched optical rectification using ultrashort laser pulses with tilted pulse fronts,” *Applied Physics Letters* **83**, 3000 (2003).
- [43] K.-L. Yeh, J. H. M.C. Hoffmann, and K. Nelson, “Generation of 10 μ j ultrashort terahertz pulses by optical rectification,” *Applied Physics Letters* **90**, 171121 (2007).

- [44] J. Fülöp, L. Pálfalvi, G. Almási, and J. Hebling, “Design of high-energy terahertz sources based on optical rectification,” *Optics Express* **18**, 12311–12327 (2010).
- [45] J. Fülöp, L. Pálfalvi, M. Hoffmann, and J. Hebling, “Towards generation of mJ-level ultrashort THz pulses by optical rectification,” *Optics Express* **19**, 15090–15097 (2011).
- [46] J. Fülöp, L. Pálfalvi, S. Klingebiel, G. Almasi, F. Krausz, S. Karsch, and J. Hebling, “Generation of sub-mJ terahertz pulses by optical rectification,” *Optics Letters* **37**, 557–559 (2012).
- [47] J. Fülöp, Z. Ollmann, C. Lombosi, C. Skrobol, S. Klingebiel, L. Pálfalvi, F. Krausz, S. Karsch, and J. Hebling, “Efficient generation of THz pulses with 0.4 mJ energy,” *Optics Express* **22**, 20155–20163 (2014).
- [48] X. Wu, S. Carbajo, K. Ravi, F. Ahr, G. Cirimi, Y. Zhou, O. Mücke, and F. Kärtner, “Terahertz generation in lithium niobate driven by Ti:sapphire laser pulses and its limitations,” *Optics Letters* **39**, 5403–5406 (2014).
- [49] K. Ravi, W. Huang, S. Carbajo, X. Wu, and F. Kärtner, “Limitations to THz generation by optical rectification using tilted pulse fronts,” *Optics Express* **22**, 20239–20251 (2014).
- [50] K. Ravi, W. Huang, S. Carbajo, E. Nanni, D. Schimpf, E. Ippen, and F. Kärtner, “Theory of terahertz generation by optical rectification using tilted-pulse-fronts,” *Optics Express* **23**, 5253–5276 (2015).
- [51] L. Xu, X. Zhang, and D. Auston, “Terahertz beam generation by femtosecond optical pulses in electro-optic materials,” *Applied Physics Letters* **61**, 1784–1786 (1992).
- [52] T. Carrig, G. Rodriguez, T. Clement, A. Taylor, and K. Stewart, “Generation of terahertz radiation using electro-optic crystal mosaics,” *Applied Physics Letters* **66**, 10–12 (1995).
- [53] T. Carrig, G. Rodriguez, T. Clement, A. Taylor, and K. Stewart, “Scaling of terahertz radiation via optical rectification in electro-optic crystals,” *Applied Physics Letters* **66**, 121–123 (1995).

- [54] B. Monozslai, C. Vicario, M. Jazbinsek, and C. Hauri, “High-energy terahertz pulses from organic crystals: DAST and DSTMS pumped at Ti:sapphire wavelength,” *Optics Letters* **38**, 5106–5109 (2013).
- [55] C. Vicario, B. Monozslai, and C. Hauri, “GV/m single-cycle terahertz fields from a laser-driven large-size partitioned organic crystal,” *Physical Review Letters* **112**, 213901 (2014).
- [56] C. Vicario, A. Ovchinnikov, S. Ashitkov, M. Agranat, V. Fortov, and C. Hauri, “Generation of 0.9-mJ THz pulses in DSTMS pumped by a Cr:Mg₂SiO₄ laser,” *Optics Letters* **39**, 6632–6635 (2014).
- [57] C. Vicario, M. Jazbinsek, A. Ovchinnikov, O. Chefonov, S. Ashitkov, M. Agranat, and C. Hauri, “High efficiency THz generation in DSTMS, DAST and OH1 pumped by Cr:forsterite laser,” *Optics Express* **23**, 4573–4580 (2015).
- [58] M. Shalaby, C. Vicario, K. Thirupugalmani, S. Brahadeeswaran, and C. Hauri, “Intense THz source based on BNA organic crystal pumped at Ti:sapphire wavelength,” *Optics Letters* **41**, 1777–1780 (2016).
- [59] M. Shalaby and C. Hauri, “Spectrally intense terahertz source based on triangular selenium,” *Scientific Reports* **5**, 8059 (2015).
- [60] H. Hamster, A. Sullivan, S. Gordon, W. White, and R. Falcone, “Subpicosecond, electromagnetic pulses from intense laser-plasma interaction,” *Physical Review Letters* **71**, 2725 (1993).
- [61] H. Hamster, A. Sullivan, S. Gordon, and R. Falcone, “Short-pulse terahertz radiation from high-intensity-laser-produced plasmas,” *Physical Review E* **49**, 671 (1994).
- [62] D. Cook and R. Hochstrasser, “Intense terahertz pulses by four-wave rectification in air,” *Optics Letters* **25**, 1210–1212 (2000).
- [63] J. Dai, J. Liu, and X.-C. Zhang, “Terahertz wave air photonics: Terahertz wave generation and detection with laser-induced gas plasma,” *IEEE Journal of Selected Topics in Quantum Electronics* **17**, 183–190 (2011).

- [64] F. Buccheri and X.-C. Zhang, “Terahertz emission from laser-induced microplasma in ambient air,” *Optica* **2**, 366–369 (2015).
- [65] Y. Shibata, T. Takahashi, T. Kanai, K. Ishi, M. Ikezawa, J. Ohkuma, S. Okuda, and T. Okada, “Diagnostics of an electron beam of a linear accelerator using coherent transition radiation,” *Physical Review E* **50**, 1479 (1994).
- [66] M. Hoffmann, S. Schulz, S. Wesch, S. Wunderlich, A. Cavalleri, and B. Schmidt, “Coherent single-cycle pulses with MV/cm field strengths from a relativistic transition radiation light source,” *Optics Letters* **36**, 4473–4475 (2011).
- [67] W. Leemans, C. Geddes, J. Faure, C. Tóth, J. van Tilborg, C. Schroeder, E. Esarey, G. Fubiani, D. Auerbach, B. Marcelis, M. Carnahan, R. Kaindl, J. Byrd, and M. Martin, “Observation of terahertz emission from a laser-plasma accelerated electron bunch crossing a plasma-vacuum boundary,” *Physical Review Letters* **91**, 074802 (2003).
- [68] C. Schroeder, E. Esarey, J. van Tilborg, and W. Leemans, “Theory of coherent transition radiation generated at a plasma-vacuum interface,” *Physical Review E* **69**, 016501 (2004).
- [69] J. van Tilborg, C. Schroeder, C. Filip, C. Tóth, C. Geddes, G. Fubiani, R. Huber, R. Kaindl, E. Esarey, and W. Leemans, “Temporal characterization of femtosecond laser-plasma-accelerated electron bunches using terahertz radiation,” *Physical Review Letters* **96**, 014801 (2006).
- [70] A. Debus, M. Bussmann, U. Schramm, R. Sauerbrey, C. Murphy, Z. Major, R. Hörlein, L. Veisz, K. Schmid, J. Schreiber, K. Witte, S. Jamison, J. Gallacher, D. Jaroszynski, M. Kaluza, B. Hidding, S. Kiselev, R. Heathcote, P. Foster, D. Neely, E. Divall, C. Hooker, J. Smith, K. Ertel, A. Langley, P. Norreys, J. Collier, and S. Karsch, “Electron bunch length measurements from laser-accelerated electrons using single-shot THz time-domain interferometry,” *Physical Review Letters* **104**, 084802 (2010).
- [71] Y.-S. Lee, T. Meade, V. Perlin, H. Winful, T. B. Norris, and A. Galvanauskas, “Generation of narrow-band terahertz radiation via optical rectification of femtosecond pulses in periodically poled lithium niobate,” *Applied Physics Letters* **76**, 2505–2507 (2000).

- [72] Y.-S. Lee, T. Meade, M. DeCamp, T. B. Norris, and A. Galvanauskas, “Temperature dependence of narrow-band terahertz generation from periodically poled lithium niobate,” *Applied Physics Letters* **77**, 1244–1246 (2000).
- [73] Y. S. Lee, T. Meade, T. B. Norris, and A. Galvanauskas, “Tunable narrow-band terahertz generation from periodically poled lithium niobate,” *Applied Physics Letters* **78**, 3583–3585 (2001).
- [74] N. Yu, K. Lee, D.-K. Ko, C. Kang, S. Takekawa, and K. Kitamura, “Temperature dependent narrow-band terahertz pulse generation in periodically poled crystals via difference frequency generation,” *Optics Communications* **284**, 1395 (2011).
- [75] C. Weiss, G. Torosyan, Y. Avetisyan, and R. Beigang, “Generation of tunable narrow-band surface-emitted terahertz radiation in periodically poled lithium niobate,” *Optics Letters* **26**, 563 (2001).
- [76] S. Carbajo, J. Schulte, X. Wu, K. Ravi, D. Schimpf, and F. Kärtner, “Efficient narrowband terahertz generation in cryogenically cooled periodically poled lithium niobate,” *Optics Letters* **40**, 5762–5765 (2015).
- [77] F. Ahr and coauthors, “Compressed pulse-train pumping for efficient narrowband terahertz generation in periodically poled lithium niobate,” (2018). In preparation.
- [78] A. Weling, B. Hu, N. Froberg, and D. Auston, “Generation of tunable narrowband THz radiation from large aperture photoconducting antennas,” *Applied Physics Letters* **64**, 137–139 (1994).
- [79] J. Danielson, A. Jameson, J. Tomaino, H. Hui, J. Wetzel, Y.-S. Lee, and K. Vodopyanov, “Intense narrow band terahertz generation via type-ii difference-frequency generation in ZnTe using chirped optical pulses,” *Journal of Applied Physics* **104**, 033111 (2008).
- [80] Z. Chen, X. Zhou, C. A. Werley, and K. A. Nelson, “Generation of high power tunable multicycle terahertz pulses,” *Applied Physics Letters* **99**, 071102 (2011).

- [81] B. Liu, H. Bromberger, A. Cartella, T. Gebert, M. Först, and A. Cavalleri, “Generation of narrowband, high-intensity, carrier-envelope phase-stable pulses tunable between 4 and 18 THz,” *Optics Letters* **42**, 129–131 (2017).
- [82] A. Cartella, T. Nova, A. Oriana, G. Cerullo, M. Först, C. Manzoni, and A. Cavalleri, “Narrowband carrier-envelope phase stable mid-infrared pulses at wavelengths beyond 10 μm by chirped-pulse difference frequency generation,” *Optics Letters* **42**, 663–666 (2017).
- [83] K. Ravi, M. Hemmer, G. Cirimi, F. Reichert, D. Schimpf, O. Mücke, and F. Kärtner, “Cascaded parametric amplification for highly efficient terahertz generation,” *Optics Letters* **41**, 3806–3809 (2016).
- [84] G. Cirimi, M. Hemmer, K. Ravi, F. Reichert, L. Zapata, A.-L. Calendron, H. Cankaya, F. Ahr, O. Mücke, N. Matlis, and F. Kärtner, “Cascaded second-order processes for the efficient generation of narrowband terahertz radiation,” *Journal of Physics B: Atomic Molecular and Optical Physics* **50**, 044002 (2017).
- [85] F. Ahr, S. Jolly, N. Matlis, S. Carbajo, T. Kroh, K. Ravi, D. Schimpf, J. Schulte, H. Ishizuki, T. Taira, and F. Kärtner, “Narrowband terahertz generation with chirped-and-delayed laser pulses in periodically poled lithium niobate,” *Optics Letters* **42**, 2118–2121 (2017).
- [86] K. Vodopyanov, “Optical generation of narrow-band terahertz packets in periodically-inverted electro-optic crystals: conversion efficiency and optimal laser pulse format,” *Optics Express* **14**, 2263–2276 (2006).
- [87] P. Bartkiewicz and P. Duval, “TINE as an accelerator control system at DESY,” *Measurement Science and Technology* **18**, 2379–2386 (2007).
- [88] S. Goloborodko, G. Grygiel, O. Hensler, V. Kocharyan, K. Rehlich, and P. Shevtsov, “DOOCS: an object oriented control system as the integrating part for the TTF linac,” in “proceedings of ICALEPCS,” (1997).

- [89] P. Tournois, “Acousto-optic programmable dispersive filter for adaptive compensation of group delay time dispersion in laser systems,” *Optics Communications* **140**, 245–249 (1997).
- [90] B. Platt and R. Shack, “History and principles of Shack-Hartmann wavefront sensing,” *Journal of Refractive Surgery* **17**, S573–S577 (2001).
- [91] H. Baumhacker, G. Pretzler, K. Witte, M. Hegelich, M. Kaluza, S. Karsch, A. Kudryashov, V. Samarkin, and A. Roukossouev, “Correction of strong phase and amplitude modulations by two deformable mirrors in a multistaged Ti:sapphire laser,” *Optics Letters* **27**, 1570–1572 (2002).
- [92] G. Genoud, M. S. Bloom, J. Vieira, M. Burza, Z. Najmudin, A. Persson, L. Silva, K. Svensson, C.-G. Wahlström, and S. Mangles, “Increasing energy coupling into plasma waves by tailoring the laser radial focal spot distribution in a laser wakefield accelerator,” *Physics of Plasmas* **20**, 064501 (2013).
- [93] T. Oksenhendler, S. Coudreau, N. Forget, V. Crozatier, S. Grabielle, R. Herzog, O. Gobert, and D. Kaplan, “Self-referenced spectral interferometry,” *Applied Physics B* **99**, 7–12 (2010).
- [94] A. Moulet, S. Grabielle, C. Cornaggia, N. Forget, and T. Oksenhendler, “Single-shot, high-dynamic-range measurement of sub-15 fs pulses by self-referenced spectral interferometry,” *Optics Letters* **35**, 3856–3858 (2010).
- [95] S. Grabielle, A. Moulet, N. Forget, V. Crozatier, S. Coudreau, R. Herzog, T. Oksenhendler, C. Cornaggia, and O. Gobert, “Self-referenced spectral interferometry cross-checked with SPIDER on sub-15 fs pulses,” *Nuclear Instruments and Methods in Physics Research A* **653**, 121–125 (2011).
- [96] J. Janszky, G. Corradi, and R. Gyuzalian, “On a possibility of analysing the temporal characteristics of short light pulses,” *Optics Communications* **23**, 293–298 (1977).

- [97] Y. Ishida, T. Yajima, and A. Watanabe, “A simple monitoring system for single sub-picosecond laser pulses using an SH spatial autocorrelation method and a CCD image sensor,” *Optics Communications* **56**, 57–60 (1985).
- [98] A. Brun, G. L. S. P. Georges, and F. Salin, “Single-shot characterization of ultrashort light pulses,” *Journal of Physics D: Applied Physics* **24**, 1225 (1991).
- [99] R. Trebino, K. DeLong, D. Flittinghoff, J. Sweetser, M. Krumbügel, B. Richman, and D. Kane, “Measuring ultrashort laser pulses in the time-frequency domain using frequency-resolved optical gating,” *Review of Scientific Instruments* **68**, 3277–3295 (1997).
- [100] S. Luan, M. Hutchinson, R. Smith, and F. Zhou, “High dynamic range third-order correlation measurement of picosecond laser pulse shapes,” *Measurement Science and Technology* **4**, 1426 (1993).
- [101] G. Grygiel and V. Rybnikov, “DOOCS camera system,” in “proceedings of ICALEPCS,” (2007).
- [102] G. Genoud, F. Wojda, M. Burza, A. Persson, , and C.-G. Wahlström, “Active control of the pointing of a multi-terawatt laser,” *Review of Scientific Instruments* **82**, 033102 (2011).
- [103] E. Sombrowski, R. Kammering, and K. Rehlich, “A HTML5 web interface for Java DOOCS data display,” in “proceedings of ICALEPCS,” (2015).
- [104] C. Siders, S. L. Blanc, D. Fisher, T. Tajima, M. Downer, A. Babine, A. Stepanov, and A. Sergeev, “Laser wakefield excitation and measurement by femtosecond longitudinal interferometry,” *Physical Review Letters* **76**, 3570 (1996).
- [105] N. Matlis, S. Reed, S. Bulanov, V. Chvykov, G. Kalintchenko, T. Matsuoka, P. Rousseau, V. Yanovsky, A. Maksimchuk, S. Kalmykov, G. Shvets, and M. Downer, “Snapshots of laser wakefields,” *Nature Physics* **2**, 749–753 (2006).
- [106] J. Faure, C. Rechatin, A. Norlin, A. Lifschitz, Y. Glinec, and V. Malka, “Controlled injection and acceleration of electrons in plasma wakefields by colliding laser pulses,” *Nature* **444**, 737–739 (2006).

- [107] V. Malka, J. Faure, C. Rechatin, A. Ben-Ismaïl, J. Lim, X. Davoine, and E. Lefebvre, “Laser-driven accelerators by colliding pulses injection: A review of simulation and experimental results,” *Physics of Plasmas* **16**, 056703 (2009).
- [108] E. Esarey, S. Ride, and P. Sprangle, “Nonlinear Thomson scattering of intense laser pulses from beams and plasmas,” *Physical Review E* **48**, 3003–3021 (1993).
- [109] K. T. Phuoc, S. Corde, C. Thauray, V. Malka, A. Tafzi, J. Goddet, R. Shah, S. Sebban, and A. Rousse, “All-optical Compton gamma-ray source,” *Nature Photonics* **6**, 308–311 (2012).
- [110] S. Chen, N. Powers, I. Ghebregziabher, C. Maharjan, C. Liu, G. Golovin, S. Banerjee, J. Zhang, N. Cunningham, A. Moorti, S. Clarke, S. Pozzi, and D. Umstadter, “MeV-energy X rays from inverse Compton scattering with laser-wakefield accelerated electrons,” *Physical Review Letters* **110**, 155003 (2013).
- [111] N. Powers, I. Ghebregziabher, G. Golovin, C. Liu, S. Chen, S. Banerjee, J. Zhang, and D. Umstadter, “Quasi-monoenergetic and tunable X-rays from a laser-driven Compton light source,” *Nature Photonics* **8**, 28–31 (2014).
- [112] H.-E. Tsai, X. Wang, J. Shaw, Z. Li, A. Arefiev, X. Zhang, R. Zgadzaj, W. Henderson, V. Khudik, G. Shvets, and M. Downer, “Compact tunable Compton x-ray source from laser-plasma accelerator and plasma mirror,” *Physics of Plasmas* **22**, 023106 (2015).
- [113] M. Hoffmann and J. Turner, “Ultrafast X-ray experiments using terahertz excitation,” *Synchrotron Radiation News* **25**, 17–24 (2012).
- [114] R. Mainz. Private communication.
- [115] T. Schibli, J. Kim, O. Kuzucu, J. Gopinath, S. Tandon, G. Petrich, L. Kolodziejcki, J. Fujimoto, E. Ippen, and F. Kärtner, “Attosecond active synchronization of passively mode-locked lasers by balanced cross correlation,” *Optics Letters* **28**, 947–949 (2003).
- [116] F. Batysta, R. Antipenkov, J. Green, J. Naylor, J. Novák, T. Mazanec, P. Hříbek, C. Zervos, P. Bakule, and B. Rus, “Pulse synchronization system for picosecond pulse-pumped

- OPCPA with femtosecond-level relative timing jitter,” *Optics Express* **22**, 30281–30286 (2014).
- [117] J. Kim, J. Chen, Z. Zhang, F. Wong, F. Kärtner, F. Loehl, and H. Schlarb, “Long-term femtosecond timing link stabilization using a single-crystal balanced cross correlator,” *Optics Letters* **32**, 1044–1046 (2007).
- [118] C. Manzoni, S.-W. Huang, G. Cirimi, P. Farinello, J. Moses, F. Kärtner, and G. Cerullo, “Coherent synthesis of ultra-broadband optical parametric amplifiers,” *Optics Letters* **37**, 1880–1882 (2012).
- [119] R. Mainz, G. M. Rossi, G. Cirimi, Y. Yang, O. Mücke, and F. Kärtner, “High-dynamic-range arrival time control for flexible, accurate and precise parametric sub-cycle waveform synthesis,” *Optics Express* **25**, 3052–3058 (2017).
- [120] F. Ahr, “High energy multi-cycle terahertz generation,” Ph.D. thesis, Universität Hamburg (2017).
- [121] J. Hebling, K. L. Yeh, M. C. Hoffmann, and K. A. Nelson, “High-power THz generation, THz nonlinear optics, and THz nonlinear spectroscopy,” *IEEE Journal of Selected Topics in Quantum Electronics* **14**, 345 (2008).
- [122] M. Fejer, G. Magel, D. Jundt, and R. Byer, “Quasi-phase-matched second harmonic generation: Tuning and tolerances,” *IEEE Journal of Quantum Electronics* **28**, 2631–2654 (1992).
- [123] M. Yamada, N. Nada, M. Saitoh, and K. Watanabe, “First-order quasi-phase matched LiNbO₃ waveguide periodically poled by applying an external field for efficient blue second-harmonic generation,” *Applied Physics Letters* **62**, 435–436 (1993).
- [124] Z. Cao, X. Gao, W. Chen, H. Wang, W. Zhang, and Z. Gong, “Study of quasi-phase matching wavelength acceptance bandwidth for periodically poled LiNbO₃ crystal-based difference-frequency generation,” *Optics and Lasers in Engineering* **47**, 589–593 (2009).

- [125] D. Jundt, “Temperature-dependent Sellmeier equation for the index of refraction, n_e , in congruent lithium niobate,” *Optics Letters* **22**, 1553–1555 (1997).
- [126] X. Wu, C. Zhou, W. Huang, F. Ahr, and F. Kärtner, “Temperature dependent refractive index and absorption coefficient of congruent lithium niobate crystals in the terahertz range,” *Optics Express* **23**, 29729–29737 (2015).
- [127] L. Pálfalvi, J. Hebling, J. Kuhl, A. Peter, and K. Polgar, “Temperature dependence of the absorption and refraction of Mg-doped congruent and stoichiometric LiNbO₃ in the THz range,” *Journal of Applied Physics* **07**, 123505 (2005).
- [128] M. Unferdorben, Z. Szaller, I. Hajdara, J. Hebling, and L. Pálfalvi, “Measurement of refractive index and absorption coefficient of congruent and stoichiometric lithium niobate in the terahertz range,” *Journal of Infrared, Millimeter, and Terahertz Waves* **36**, 1203–1209 (2015).
- [129] M. Cronin-Golomb, “Cascaded nonlinear difference-frequency generation of enhanced terahertz wave production,” *Optics Letters* **29**, 2046 (2004).
- [130] H. Ishizuki and T. Taira, “Half-joule output optical-parametric oscillation using 10-mm-thick periodically poled Mg-doped congruent LiNbO₃,” *Optics Express* **20**, 20002–20010 (2012).
- [131] D. Dietze, K. Unterrainer, and J. Darmo, “Dynamically phase-matched terahertz generation,” *Optics Letters* **37**, 183–190 (2012).
- [132] E. Petersen, W. Shi, A. Chavez-Pirson, N. Peyghambarian, and A. Cooney, “Efficient parametric terahertz generation in quasi-phase-matched GaP through cavity enhanced difference-frequency generation,” *Applied Physics letters* **98**, 121119 (2011).
- [133] P. Han and X.-C. Zhang, “Coherent, broadband midinfrared terahertz beam sensors,” *Applied Physics Letters* **73**, 3049–3051 (1998).
- [134] G. Gallot and D. Grischkowsky, “Electro-optic detection of terahertz radiation,” *Journal of the Optical Society of America B* **16**, 1204–1212 (1999).

- [135] T. Hattori, Y. Homma, A. Mitsuishi, and M. Tacke, “Indices of refraction of ZnS, ZnSe, ZnTe, CdS, and CdTe in the far infrared,” *Optics Communications* **7**, 229–232 (1973).
- [136] G. Gallot, J. Zhang, R. McGowan, T.-I. Jeon, and D. Grischkowsky, “Measurements of the THz absorption and dispersion of ZnTe and their relevance to the electro-optic detection of THz radiation,” *Applied Physics Letters* **74**, 3450–3452 (1999).
- [137] F. Madarasz, J. Dimmock, N. Dietz, and K. Bachmann, “Sellmeier parameters for ZnGaP₂ and GaP,” *Journal of Applied Physics* **87**, 1564–1565 (2000).
- [138] M. Miyagi and S. Nishida, “Pulse spreading in a single-mode fiber due to third-order dispersion,” *Applied Optics* **18**, 678–682 (1979).
- [139] T. Yoshida, S. Kamada, and T. Aoki, “Elimination of the chirp of narrowband terahertz pulses generated by chirped pulse beating using a tandem grating pair laser pulse stretcher,” *Optics Express* **22**, 23679–23685 (2014).
- [140] S. Sartania, Z. Cheng, M. Lenzner, G. Tempea, C. Spielmann, F. Krausz, and K. Ferencz, “Generation of 0.1-TW 5-fs optical pulses at a 1-kHz repetition rate,” *Optics Letters* **22**, 1562–1564 (1997).
- [141] M. Polyanskiy, “Refractive index database,” <https://refractiveindex.info/>.
- [142] V. Pervak, C. Teisset, A. Sugita, S. Naumov, F. Krausz, and A. Apolonski, “High-dispersive mirrors for femtosecond lasers,” *Optics Express* **16**, 10220–10233 (2008).
- [143] S.-H. Chia, G. Cirimi, G. R. S. Fang, O. Mücke, and F. Kärtner, “Two-octave-spanning dispersion-controlled precision optics for sub-optical-cycle waveform synthesizers,” *Optica* **1**, 315–322 (2014).
- [144] W. Knox, N. Pearson, K. Li, and C. Hirlimann, “Interferometric measurements of femtosecond group delay in optical components,” *Optics Letters* **13**, 574–576 (1988).
- [145] “Transfer-matrix method (optics),” [https://en.wikipedia.org/wiki/Transfer-matrix_method_\(optics\)](https://en.wikipedia.org/wiki/Transfer-matrix_method_(optics)).

- [146] M. Naftaly and R. Miles, “Terahertz time-domain spectroscopy of silicate glasses and the relationship to material properties,” *Journal of Applied Physics* **102**, 043517 (2007).
- [147] D. Slocum, E. Slingerland, R. Giles, and T. Goyette, “Atmospheric absorption of terahertz radiation and water vapor continuum effects,” *Journal of Quantitative Spectroscopy and Radiative Transfer* **127**, 49–63 (2013).

Vita

Spencer Jolly was born in Evansville, IN in 1989 and soon afterwards followed his parents to the northern suburbs of Philadelphia where he spent the rest of his youth. After attending Pennsbury High School and graduating near the top of his class in 2007, he enrolled in the University of Michigan in Ann Arbor. Originally a gear-head interested in working on internal combustion engines, he widened his reach and became a physics major in his junior year at Michigan. There he took up his first work with high-intensity lasers with Alec Thomas. After working on two-color high-intensity interactions with Mike Downer in Austin, TX for a master's degree, Spencer moved to Europe to work on a collaboration between ELI-Beamlines and Universität Hamburg in order to earn his PhD under Andi Maier. There he contributed significantly to the operation of the ANGUS laser system and the LUX plasma acceleration and undulator radiation experiment, in addition to broad work on mJ-level narrowband terahertz generation.

Permanent address: 6 Oak Ave
Yardley, PA 19067

This dissertation was typeset with \LaTeX^\dagger by the author.

[†] \LaTeX is a document preparation system developed by Leslie Lamport as a special version of Donald Knuth's \TeX Program.